

**THERMOFLUIDIC TRANSPORT IN EVAPORATING DROPLETS:  
MEASUREMENT AND APPLICATION**

by

**Aditya Chandramohan**

**A Dissertation**

*Submitted to the Faculty of Purdue University*

*In Partial Fulfillment of the Requirements for the degree of*

**Doctor of Philosophy**



School of Mechanical Engineering

West Lafayette, Indiana

May 2019

**THE PURDUE UNIVERSITY GRADUATE SCHOOL  
STATEMENT OF COMMITTEE APPROVAL**

Dr. Suresh V. Garimella, Co-Chair

School of Mechanical Engineering

Dr. Justin A. Weibel, Co-Chair

School of Mechanical Engineering

Dr. Jun Chen

School of Mechanical Engineering

Dr. Muhammad A. Alam

School of Electrical and Computer Engineering

**Approved by:**

Dr. Jay P. Gore

Head of the Graduate Program

*This work is dedicated to my parents and my sister*

## ACKNOWLEDGMENTS

I would like to thank my advisors, Dr. Suresh V. Garimella and Dr. Justin A. Weibel, for their continued guidance through the course of my Ph.D. Their patience and dedication in helping me develop my research, presentation, and professional skills tremendously.

Additionally, I would like to thank the members of my advisory committee, Dr. Muhammad A. Alam and Dr. Jun Chen, for their timely and helpful comments on my preliminary proposals. Their input helped me apply the early part of my research into a meaningful application.

I am forever grateful to all of my lab members, for their advice and ideas whenever I hit a snag in my research. I will always treasure our lunch discussions and our friendship for making my Ph.D. a much more pleasant experience. I would like to thank Dr. Susmita Dash for guiding me as a novice researcher during the early parts of my Ph.D. and helping me develop my own ideas for research. I would also like to thank Sara Lyons, Dr. Xuemei Chen, Dr. Monojit Chakraborty, and Rishav Roy for their lending their assistance and research expertise in my research.

Lastly, I would like to thank my parents and my sister for their persistent support of my endeavors, especially through the tough times. Thank you for guiding me and making me the person and professional that I am today.

## TABLE OF CONTENTS

LIST OF TABLES .....	8
LIST OF FIGURES .....	9
ABSTRACT .....	13
CHAPTER 1. INTRODUCTION .....	16
1.1 Background .....	16
1.2 Objectives and Major Contributions .....	16
1.3 Organization of Thesis .....	17
CHAPTER 2. LITERATURE REVIEW .....	18
2.1 Multiframe Super-Resolution and Infrared Thermography .....	18
2.2 Characterization of Interface Temperature during Water Droplet Evaporation .....	19
2.3 Evaporation Dynamics in Organic Liquid Droplets .....	21
2.4 Miniaturized Colorimetric Analysis of Protein Concentration .....	22
CHAPTER 3. QUANTITATIVE ANALYSIS OF ERROR REDUCTION IN EMISSIVITY MAPPING AND INFRARED THERMOGRAPHY BY MULTIFRAME SUPER- RESOLUTION .....	25
3.1 Materials and Methods .....	25
3.1.1 Infrared Measurement Setup .....	25
3.1.2 Emissivity Mapping .....	27
3.2 Simulated Images .....	28
3.3 Results and Discussion .....	29
3.3.1 Experimental Results .....	29
3.3.2 Simulation Results .....	33
3.4 Conclusion .....	38
CHAPTER 4. SPATIOTEMPORAL INFRARED MEASUREMENT OF INTERFACE TEMPERATURES DURING WATER DROPLET EVAPORATION ON A NONWETTING SUBSTRATE .....	40
4.1 Materials and Methods .....	40
4.2 Results and Discussion .....	42
4.2.1 Raw Data Analysis .....	42

4.2.2 Reflection Correction .....	44
4.2.3 Evaporation Rate .....	46
4.3 Conclusion .....	47
CHAPTER 5. MARANGONI CONVECTION IN EVAPORATING ORGANIC LIQUID DROPLETS ON A NONWETTING SUBSTRATE.....	48
5.1 Materials and Methods.....	48
5.2 Results and Discussion .....	51
5.2.1 Velocity Profiles and Temperature Measurements .....	51
5.2.2 Velocity Scaling Analysis .....	53
5.2.3 Reduced-Order Evaporation Model Incorporating Advective Transport in the Droplet .....	56
5.3 Conclusion .....	58
CHAPTER 6. EVAPORATION-DRIVEN MICROMIXING IN SESSILE DROPLETS FOR MINIATURIZED ABSORBANCE-BASED COLORIMETRY .....	59
6.1 Materials and Methods.....	59
6.2 Results and Discussion .....	62
6.3 Conclusion .....	71
CHAPTER 7. CONCLUSIONS AND FUTURE WORK .....	72
7.1 Conclusions.....	72
7.2 Future Works .....	74
REFERENCES .....	76
APPENDIX A. QUANTITATIVE ANALYSIS OF MULTI-FRAME SUPER-RESOLUTION FOR EMISSIVITY-MAPPED INFRARED THERMOGRAPHY OF ELECTRONIC DEVICES.....	88
APPENDIX B. SPATIOTEMPORAL INFRARED MEASUREMENT OF INTERFACE TEMPERATURES DURING WATER DROPLET EVAPORATION ON A NONWETTING SUBSTRATE.....	94
APPENDIX C. MARANGONI CONVECTION IN EVAPORATING ORGANIC LIQUID DROPLETS ON A NONWETTING SUBSTRATE.....	113
APPENDIX D. THE ROLE OF CONDENSATION FROM HUMID AIR ON MELTING OF ICE .....	124

APPENDIX E. ABSORBANCE-BASED COLORIMETRIC QUANTITATION IN EVAPORATING, SESSILE DROPLETS ON A NONWETTING SUBSTRATE .....	140
APPENDIX F. LIST OF EXPERIMENTAL EQUIPMENT .....	143
VITA .....	146
PUBLICATIONS.....	147

## LIST OF TABLES

Table 5.1. Liquid Properties at 300 K.....	54
Table F.1. Experimental Equipment and Materials. ....	143

## LIST OF FIGURES

Figure 3.1. Schematic diagram of the experimental setup used for the multi-frame super-resolution infrared measurements. ....	26
Figure 3.2. (a) Photograph of the computer memory card used to demonstrate multi-frame super-resolution reconstruction. (b) An inset photograph of a serpentine wire trace feature with (c) the corresponding low-resolution and (d) multi-frame super-resolution infrared intensity maps. ....	30
Figure 3.3. (a) Uncorrected and (b) emissivity-corrected low-resolution temperature maps, as well as (c) uncorrected and (d) corrected multi-frame super-resolution maps of a portion of the component shown in Figure 3.2. ....	31
Figure 3.4. Emissivity maps generated using the (a) low-resolution and (b) super-resolution images. ....	32
Figure 3.5. Maximum deviation based on a sensitivity analysis of input sensitivity values are plotted. ....	33
Figure 3.6. The (a) smooth wave and (b) sharp band scenes of nondimensionalized temperature are shown above horizontal line plots of the scene, multiframe super-resolution image, and low-resolution image. ....	35
Figure 3.7. The absolute errors for the low-resolution and super-resolution images of the nondimensionalized temperature are shown for the (a) sharp bands and (b) smooth wave scenes. ....	37
Figure 3.8. The difference between the error of the low-resolution and multiframe super-resolution images of the nondimensionalized temperature plotted as a function of the pixel-to-feature size ratio for the (a) sharp bands and (b) smooth wave scenes. The results with 10% maximum image noise are plotted for the (c) sharp bands and (d) smooth waves. The insets in (a) illustrate example pixel size relative to the band feature. ....	38
Figure 4.1. Schematic diagram of the experimental facility. ....	41
Figure 4.2. The uncorrected infrared temperature data are shown for droplet evaporation trials at substrate temperatures of (a) 30 °C, (b) 40 °C, (c) 50 °C, and (d) 60 °C; from left to right, the panels show droplet volumes of 3 $\mu$ L, 2 $\mu$ L, and 1 $\mu$ L. The contact radius, $R$ , and the droplet height, $h$ , are marked for the top right case. ....	43
Figure 4.3. (a) The volume, and (b) contact angle (solid symbols) and contact radius (hollow symbols) of the droplet are shown as a function of time for selected droplet evaporation trials at each substrate temperature. The time axis in (b) is normalized by the total evaporation time in each case. ....	44

Figure 4.4. Temperature data after correcting for background reflections for a 2 $\mu\text{L}$ droplet evaporating on a substrate at a temperature of 50°C. ....	45
Figure 4.5. The temperature drop across the height of the droplet is plotted as function of droplet volume (at intervals of 0.25 $\mu\text{L}$ ) for all substrate temperatures. The error bars represent the standard deviations across all trials at that substrate temperature. ....	46
Figure 4.6. The experimental evaporation rate plotted as a function of droplet volume (at intervals of 0.5 $\mu\text{L}$ ) for all for all substrate temperatures. The error bars represent the standard deviation across all trials at a given substrate temperature.....	47
Figure 5.1. (a) A scanning electron microscopy (SEM) image of the substrate, and (b) a schematic diagram of the experimental setup.....	49
Figure 5.2. (a) Velocity vector field (from PIV analysis with ray-tracing corrections) within a 1.34 $\mu\text{L}$ droplet on a substrate fixed at 10 °C, and (b) the centerline vertical velocity taken along the y-axis at $x = 0$ . (c) A streakline image is obtained from superimposing images of the tracer particles.....	51
Figure 5.3. The velocity vector fields for 1.7 $\mu\text{L}$ methanol droplets at substrate temperatures of: (a) 5 °C, (b) 10 °C, and (c) 15 °C. (d) Centerline velocity profiles for each of the substrate temperatures.....	52
Figure 5.4. Temperature drop from the bottom to the top of the droplet, and maximum velocity magnitude versus substrate temperature. The uncertainty bars indicate the standard deviation for all the tests at each substrate temperature.....	53
Figure 5.5. Projected interface velocity as a function of Marangoni velocity. The error bars show the standard deviation of the four data points at each substrate temperature for both the projected velocities and the Marangoni velocity.....	56
Figure 5.6. Comparison between the experimental values of the average temperature drop inside the droplet, the predictions from the thermal diffusion and the thermal advection models. The inlay shows the transport mechanisms included in the two models.....	58
Figure 6.1. Schematic diagram of the experimental facility used for the absorbance measurement.....	60
Figure 6.2. Time-resolved absorbance measurements for premixed sample droplets at concentrations of: (a) 1.51 $\mu\text{M}$ , (b) 2.26 $\mu\text{M}$ , and (c) 4.51 $\mu\text{M}$ .....	64
Figure 6.3. The sample absorbance metric values at 400 s (extracted from Figure 6.2) are plotted as a function of concentration, along with a linear fit (dashed line) and an 80% prediction interval (dash-dotted line).....	65
Figure 6.4. Time-resolved absorbance measurements for <i>in situ</i> mixed sample at concentrations of: (a) 1.51 $\mu\text{M}$ , (b) 2.26 $\mu\text{M}$ , and (c) 4.51 $\mu\text{M}$ .....	67

- Figure 6.5. Cropped image frames, captured at 100 s increments from the droplet video for the *in situ* mixing case at a concentration of 0.3 mg/mL (4.51  $\mu$ M). ..... 68
- Figure 6.6. A plot of the temporal absorbance for a selected trial at a sample concentration of 0.3 mg/mL (4.51  $\mu$ M) with inset schematic drawings showing the various phases of *in situ* mixing of the reactant and sample, including: (1) the initial droplet, (2) the mixing phase, (3) the dilution phase, (4) the reaction phase, and (5) the adsorption phase..... 69
- Figure 6.7. The absorbance metric at (a) the first peak, (b) the first valley, and (c) the second peak along with their respective linear fits and 80% prediction intervals are shown. Their corresponding locations on the temporal data are illustrated in (d)..... 70
- Figure B.1. Calibration curve for a single pixel in the infrared camera frame with the corresponding calibration points..... 94
- Figure B.2. Comparison of thermocouple and infrared temperature measurements plotted with a one-to-one correlation line. The horizontal and vertical error bars represent the calibrated thermocouple measurement error and the calibrated infrared measurement error, respectively. . 98
- Figure B.3. The reflectivity plotted (a) as a function of the angle from the surface normal, and (b) as a function of position on the surface of an example droplet (at a volume of 2.5  $\mu$ L). ..... 100
- Figure B.4. Temperature data after correcting for background reflections for a substrate temperature of 30°C for droplet volumes of (a) 3.0  $\mu$ L, (b) 2.5  $\mu$ L, (c) 2.0  $\mu$ L, (d) 1.5  $\mu$ L, and (e) 1.0  $\mu$ L..... 101
- Figure B.5. Temperature data after correcting for background reflections for a substrate temperature of 40°C for droplet volumes of (a) 3.0  $\mu$ L, (b) 2.5  $\mu$ L, (c) 2.0  $\mu$ L, (d) 1.5  $\mu$ L, and (e) 1.0  $\mu$ L..... 102
- Figure B.6. Temperature data after correcting for background reflections for a substrate temperature of 50°C for droplet volumes of (a) 3.0  $\mu$ L, (b) 2.5  $\mu$ L, (c) 2.0  $\mu$ L, (d) 1.5  $\mu$ L, and (e) 1.0  $\mu$ L..... 103
- Figure B.7. Temperature data after correcting for background reflections for a substrate temperature of 60°C for droplet volumes of (a) 3.0  $\mu$ L, (b) 2.5  $\mu$ L, (c) 2.0  $\mu$ L, (d) 1.5  $\mu$ L, and (e) 1.0  $\mu$ L..... 104
- Figure B.8. Vertical infrared temperature profiles along droplet centerline during the evaporation process at 1  $\mu$ L, 2  $\mu$ L, and 3  $\mu$ L for a substrate temperature of 50°C (not corrected for reflection from the background as shown)..... 106
- Figure B.9. The evaporation rates from the experiments, vapor-diffusion-based predictions, and natural-convection-based predictions for a droplet volume of 2.5  $\mu$ L. The error bars represent the standard deviation for all trials at that substrate temperature. .... 108
- Figure C.1. The centerline vertical velocity profile is shown at multiple volumes for substrate temperatures of: (a) 5 °C, (b) 10 °C, (c) 15 °C, and (d) room temperature. .... 113

Figure C.2. Relationship between the Marangoni number and maximum velocity. The error bars represent standard deviations over all four tests at each substrate temperature (5 °C, 10 °C, 15 °C, and room temperature). ..... 114

Figure C.3. (a) An example experimental velocity field (at a substrate temperature of 10 °C and droplet volume of 1.34  $\mu\text{L}$ ) is shown to illustrate the estimation of the near-interface upward velocity in the droplet. (b) The vertical velocity vectors are plotted at a horizontal plane of the droplet passing through the vortex center; the upward velocities in the outer region (depicted in red) are estimated based on conserving the mass flow rate from the available experimental data (depicted in blue). ..... 115

Figure C.4. (a) Schematic diagram of the evaporating droplet on a substrate with recirculating flow. The conduction-dominated and advection-dominated regions of the droplet are shown in lighter and darker shades, respectively. Representative discretized control volumes for the (b) conduction-dominated and (c) advection-dominated regions of the droplet are also shown. .... 118

Figure D.1. Schematic diagram of the melting system is shown, including the boundary conditions ( $T_{mp}$ ,  $T_{\infty}$ ,  $m_{g\infty}$ ) and selected calculated physical parameters ( $v_w$ ,  $\delta(x)$ ,  $T_i$ , and  $m_{gi}$ ). ..... 128

Figure D.2. Three-dimensional drawing of the experimental setup. .... 133

Figure D.3. (a) Derivative of the nondimensional vapor-gas stream function,  $f'(\eta)$ , and the gas mass fraction in the vapor-gas domain. (b) Derivative of the nondimensional liquid stream function,  $f_l'(\eta_l)$ , and the nondimensional temperature profile in the liquid domain..... 135

Figure D.4. (a) Predicted and measured liquid film thickness results and (b) melting and condensation mass fluxes along the vertical direction at ambient conditions ( $T_{\infty} = 26$  °C, RH = 40%); the error bars represent the standard deviation of the measurements. .... 136

Figure D.5. (a) Liquid film thickness, (b) melting mass flux, and (c) condensate mass flux are shown with vertical position for four different levels of ambient relative humidity. .... 138

Figure E.1. The droplet volume evolution is shown (in blue) alongside the droplet height (in red) for two droplets with sample concentrations of 0 mg/mL (0  $\mu\text{M}$ ) and 0.15 mg/mL (2.26  $\mu\text{M}$ ). 140

Figure E.2. Time-resolved raw voltage measurements of premixed sample droplets are shown for (a) 1.51  $\mu\text{M}$ , (b) 2.26  $\mu\text{M}$ , and (c) 4.51  $\mu\text{M}$ ..... 141

Figure E.3. Time-resolved raw voltage measurements of *in situ* sample droplets are shown for (a) 1.51  $\mu\text{M}$ , (b) 2.26  $\mu\text{M}$ , and (c) 4.51  $\mu\text{M}$ . ..... 142

## ABSTRACT

Author: Chandramohan, Aditya, PhD

Institution: Purdue University

Degree Received: May 2019

Title: Thermofluidic Transport in Evaporating Droplets: Measurement and Application

Major Professor: Suresh V. Garimella, Justin A. Weibel

Microscale environments provide significant resolution and distortion challenges with respect to measurement techniques; however, with improvements to existing techniques, it is possible to gather relevant data to better understand the thermal and fluidic mechanisms at such small scales in evaporating droplets.

Infrared thermography provides several unique challenges at small scales. A primary issue is that the low native resolution of traditional infrared cameras significantly hamper the collection of details of microscale features. Furthermore, surfaces exhibiting vastly different emissivities, results in inaccurate temperature measurements that can only be corrected with irradiance-based emissivity maps of the surface; however, due to the resolution limitations of infrared thermography, these emissivity maps can also display significant errors. These issues are overcome through the use of multi-frame super-resolution. The enhanced resolution allows for better capture of microscale features, therefore, enhancing the emissivity map. A quantitative error analysis of the system is conducted to quantify the feature size resolution improvement as well as the smoothing effect of super-resolution reconstruction. Furthermore, a sensitivity analysis is conducted to quantify the impact of registration uncertainty on the accuracy of the reconstruction. Finally, the improved emissivity map from super-resolution is demonstrated to show the increased accuracy over low-resolution mapping.

When applied to water droplets, particularly on nonwetting surfaces, infrared thermography is confounded by the presence of nonuniform reflectivities due to the spherical curvature of the liquid-air interface. Thus, when measuring the temperature along the vertical axis of a water droplet, it is necessary to correct the reflection. Using a controlled background environment, in conjunction with the Fresnel equations, it is possible to correct the reflective effects on the interface

and calculate the actual temperature profile. This allows for a better understanding of the governing mechanisms that determine the thermal transport within the droplet. While thermal conduction is the primary transport mechanism along the vertical axis of the droplet, it is determined that the temperature drop is partially dampened by the convective transport from the ambient air to the liquid interface. From this understanding revealed by the measurements, the vapor-diffusion-based model for evaporation was enhanced to better predict evaporation rates.

Further exploration into the mechanisms behind droplet evaporation on nonwetting surfaces requires accurate knowledge of the internal flow behavior. In addition, the influence of the working fluid can have a significant impact on the governing mechanisms driving the flow and the magnitude of the flowrate. While water droplet evaporation has been shown to be governed by buoyancy-driven convection on nonwetting substrates, similar studies on organic liquid droplets are lacking. Particle image velocimetry is effective at generating a velocity flow field, but droplets introduce distortion due to the refraction from the spherical interface of the droplet. As such, velocity correction using a ray-tracing approach was conducted to correct the velocity magnitudes and direction. With the velocity measurements, the flow was determined to be surface-tension-driven and showed speeds that are an order of magnitude higher than those seen in buoyancy-driven flow in water droplets. This resulted in the discovery that advection plays a significant role in the transport within the droplet. As such, the vapor-diffusion-governed evaporation model was adjusted to show a dramatic improvement at predicting the temperature gradient along the vertical axis of the droplet.

Armed with the knowledge of flow behavior inside droplets, it is expected that droplets with aqueous solutions should exhibit buoyancy-driven convection. The final part of this work, therefore, leverages this phenomenon to enhance mixing during reactions. Colorimetry is a technique that is widely utilized to measure the concentration of a desired sample within some liquid; the sample reacts with a reagent dye the color change is measured, usually through absorbance measurements. In particular, the Bradford assay is used to measure protein concentration by reacting the protein to a Coomassie<sup>TM</sup> Brilliant Blue G-250. The absorbance of the dye increases, most significantly at the 590 nm wavelength, allowing for precise quantitation of the amount of protein in the solution. A droplet-based reaction chamber with buoyancy-

enhanced mixing has the potential to speed up the measurement process by removing the need for a separate pre-mixing step. Furthermore, the reduced volume makes the process more efficient in terms of reactant usage. Experimental results of premixed solutions of protein sample and reagent dye show that the absorbance measurement through a droplet tracks strongly with the protein concentration. When the protein sample and dye reagent are mixed *in situ*, the complex interaction between the reactants, the mixing, and the adsorption of protein onto the substrate creates a unique temporal evolution in the measured absorbance of the droplet. The characteristic peaks and valleys of this evolution track strongly with concentration and provide the framework for measurement of concentration in a droplet-based system.

This thesis extends knowledge about droplet thermal and fluidic behavior through enhanced measurement techniques. This knowledge is then leveraged in a novel application to create a simple, buoyancy-driven colorimetric reaction setup. Overall, this study contributes to the field of miniaturized, efficient reaction and measurement devices.

## CHAPTER 1. INTRODUCTION

### 1.1 Background

Aqueous droplet evaporation plays a defining role in DNA microarray manufacturing [1], droplet-based biosensors [2–4], droplet mixing [5], inkjet printing [6], and droplet-based particle deposition [7]. In these applications, an understanding of the thermal and species transport characteristics is critical for controlling the droplet evaporation behavior and deposition of suspended particulates. The inspection of interface temperatures is crucial to understanding and controlling the thermal and evaporative behavior of droplets for various droplet-based manufacturing and testing applications. Infrared thermography with reflection corrections can make accurate maps of surface temperatures. Organic droplet evaporation has received attention in recent studies, particularly for applications such as inkjet printing of metal patterns [8], organic transistor manufacturing [9], and micro-reactors for drug synthesis [10]. In each of these applications, which rely on deposition of solutes or suspected particulates via evaporation of droplets, knowledge of the flow behavior within the droplets is crucial to the system design. Particle image velocimetry, with ray-tracing corrections for the spherical distortion of the droplet interface, can make accurate velocity measurements, which, through scaling analysis, can reveal the governing mechanisms behind the flow behavior.

### 1.2 Objectives and Major Contributions

The primary objective of this thesis is to utilize improved measurement techniques to advance the characterization of microscale systems with the goal of eventually leveraging the findings to the application of droplet-based colorimetric measurements. The first step is evaluating the use of multi-frame super-resolution for infrared thermographic applications through error analysis of various parameters, such as smoothing, feature size recapture, and registration uncertainty. The next objective is to apply infrared thermography to measure the temperature map of an evaporating sessile water droplet to demonstrate that the dominant thermal transport phenomena governing the interface temperature and evaporation rates are thermal conduction and air-side natural convection. Further work using particle image velocimetry shows that organic liquid droplets on nonwetting

substrates. The final project utilizes the knowledge developed on droplet evaporation mechanisms on nonwetting substrates to demonstrate a simplified colorimetric quantitation approach.

### **1.3 Organization of Thesis**

The work presented in this thesis is organized into six chapters. Chapter 1 provides the relevant background information pertaining to non-invasive experimental techniques and details the major contributions and objectives of the current work. Chapter 2 discusses the literature review relevant to each of the fields explored, including multi-frame super-resolution, droplet infrared thermography, and droplet evaporation. Chapter 3 investigates the use of multi-frame super-resolution for quantitative infrared thermography of small-scale measurements. Chapter 4 investigates the temperature profile of water droplets on superhydrophobic substrates and the importance of spatiotemporally resolved measurements, through infrared thermography, to investigate the magnitude of thermal phenomena, such as thermal conduction and air-side natural convection, in the evaporation of the droplet. Chapter 5 focuses on the evaporation of organic liquid droplets on nonwetting substrates, as well as the techniques used to measure various important parameters. Chapter 6 leverages knowledge of flow behavior inside droplets to perform colorimetric quantitation of protein concentration in a sessile droplet.

## CHAPTER 2. LITERATURE REVIEW

### 2.1 Multiframe Super-Resolution and Infrared Thermography

Several standard methods are used to measure temperature in electronics packages, including thermocouples [4], probes [5], thermochromic liquid crystals [6], infrared thermography [7], microcantilevers [8], fluorescent microthermography [9], thermorefectance thermography [10], and infrared microscopes [11]. Of these techniques, infrared thermography has the advantage of noninvasively resolving spatial temperature distributions, unlike thermocouples, microcantilevers, probes, and thermochromic liquid crystals, which require sensors to be embedded into the surface of the electronics package. Traditionally, a high-emissivity surface coating is applied when using infrared thermography to overcome challenges presented by surfaces with nonuniform emissivity [12–14]. However, surface coatings may not be allowable in sensitive electronics and other applications in which the inherent irregularity of the coating, potential interference with the components, or permanent damage to the device can pose serious concerns. Noninvasive surface-emissivity mapping techniques have been used for such electronic device applications [7, 14]. When coupled with emissivity mapping, infrared thermography is simpler to implement than thermochromic liquid crystals or fluorescent microthermography.

A common practical limitation of infrared thermographic measurements is the native resolution of the camera used, rather than theoretical optical limits. Infrared microscopes that provide better spatial resolution are available, but significantly reduce the field of view. Multiframe super-resolution is an optical technique that can be used to enhance the pixel-limited resolution of infrared cameras [11]. In multiframe super-resolution, multiple low-resolution images are acquired, displaced with respect to each other by sub-pixel shifts. The unique information recorded by each of these shifted images can be leveraged to generate a single higher resolution image. Several approaches for reconstruction of the high-resolution image from the low-resolution images are described in the literature, including nonuniform interpolation [12], frequency-domain reconstruction [13], regularized reconstruction [14,15], adaptive weighted averaging [16], and others. While thermorefectance thermography [17] and infrared microscopy [18] provide high resolutions (with the former technique exceeding the diffraction limit [19]), application of super-

resolution using an apparatus for spatial displacement of an infrared camera offers a comparatively simpler measurement setup and does not require an external illumination source.

Despite the nominal resolution benefits of multiframe super-resolution, characterization of the uncertainty and the bounds of resolution improvement is a challenge. Although there are several well-developed multiframe super-resolution techniques, standardized benchmarking between the techniques is rare [20]. It is generally accepted that multiframe super-resolution has the potential to lose high-spatial-frequency data at large resolution enhancements [21]. There has been no extensive quantitative investigation into the degree of resolution improvement that can be achieved, relative to feature size. Robinson and Milanfar conducted a statistical analysis of error resulting from the signal-to-noise ratio, number of low-resolution images, relative displacement of images, and point spread function of the optical setup [22]; these factors significantly impact the ability to estimate unknown subpixel displacement shifts and thereby introduce significant uncertainties in multiframe super-resolution reconstruction when compared to image registration methods that generate *a priori* knowledge of the subpixel shifts. Approaches for multiframe super-resolution error analysis have generally focused on the registration uncertainty (*i.e.*, positional uncertainty associated with image registration during sub-pixel shifting) [23,24]. Pickup *et al.* described the deleterious impact of registration uncertainty on the reconstruction process and addressed this problem by minimizing registration errors [25]. Nevertheless, the practical capabilities of multiframe super-resolution for quantitative measurement applications, such as infrared thermography, have not been fully mapped, particularly in regards to the feature sizes that can be captured relative to the native pixel resolution of the camera.

## **2.2 Characterization of Interface Temperature during Water Droplet Evaporation**

Several measurement techniques have been applied for characterization of droplet temperatures, including microencapsulated thermochromic liquid crystals (TLC) [26], thermocouples [27,28], digital holographic interferometry [29], and infrared thermography [30,31]. Digital holographic interferometry can be used to calculate the water vapor concentration around a droplet and infer the interface temperature and local evaporation rate. Microencapsulated TLCs exhibit a temperature-dependent change in hue which can be captured using a color camera. Both microencapsulated TLCs and thermocouples are intrusive and provide temperature measurements

at discrete locations; the measurements provide temperatures close to the interface, but not at the interface itself. Infrared thermography yields a high-spatial-resolution temperature field; furthermore, it is entirely nonintrusive and does not require the complex system of lasers and mirrors needed for digital holographic interferometry. For organic liquids that are semi-transparent in the infrared spectrum, such as ethanol, methanol, and acetone, infrared thermography captures a temperature signature integrated over the penetration depth, and has been used to observe convective patterns within evaporating droplets [31–33]. Water is virtually opaque in the mid-wavelength infrared spectrum [34], allowing for temperature measurements at the interface. Girard *et al.* [35] applied this technique to measure the temperature of water droplets on a wetting substrate; Saha *et al.* [36] measured the effect of laser heating on the evaporation of acoustically levitated droplets. While some instantaneous infrared temperature measurements have been conducted for droplets evaporating on nonwetting substrates [37], none have accounted for reflections from background radiation incident on the curved surface of the droplet. Whereas coatings can be applied to solid surface to remove such reflection effects [38], this is not possible with liquid-air interfaces. Moreover, no studies have utilized infrared thermography visualizations to capture the temporal droplet (volume) evolution during evaporation alongside temperature measurements.

Accurate measurement of droplet interface temperatures during evaporation is required for improving and validating modeling efforts that have historically neglected important thermal transport mechanisms. Picknett and Bexon [39] developed one of the earliest models for sessile droplet evaporation by applying Maxwell’s diffusion-electrostatic potential analogy [40], while assuming uniform evaporative mass flux. Several later studies experimentally and numerically explored vapor diffusion around low-contact-angle (*i.e.*, wetting) evaporating droplets and concluded that evaporative mass flux is nonuniform over the droplet surface [41–43]. Popov [44] developed a closed-form, analytical solution of vapor species diffusion through air in the surrounding domain to predict the evaporation of droplets exhibiting any contact angle; however, a key assumption in the boundary conditions is that the droplet surface is at a uniform temperature, which inherently neglects the influence of thermal transport within the droplet itself. Several subsequent studies have demonstrated that convective heat and mass transfer to the surroundings can be significant [45–48].

An experimental study by Dash and Garimella [49] revealed a significant discrepancy between vapor-diffusion-based model predictions and the measured rate of droplet evaporation on nonwetting surfaces, which was attributed to a large temperature drop along the droplet height induced by evaporative cooling. High-fidelity numerical modeling by Pan and coworkers [45,50] mapped the competing effects of external natural convection and evaporative cooling as a function of the surface wettability; the relatively tall droplets supported on nonwetting surfaces have a large effective thermal resistance between the substrate and droplet interface, such that evaporative cooling governs the droplet temperature profile and evaporation rate. Gleason and Putnam [51] showed that imposing a nonuniform interface temperature profile as a correction to the vapor-diffusion model more accurately predicted the experimental evaporation data. It is clear that spatially resolved temperature measurements are needed to capture the evaporation characteristics throughout the droplet.

### **2.3 Evaporation Dynamics in Organic Liquid Droplets**

The evaporation dynamics of organic liquid droplets is known to differ significantly from that of water droplets. Volatile organic liquids generally have a higher evaporation rate than water [52] and can be used at lower temperatures in biologically sensitive applications, for example, where denaturing becomes a significant concern [53]. On wetting substrates, while internal flow in evaporating water droplets is generally driven by capillary flow [42], interfacial surface tension gradients (Marangoni flow) are the primary driver for flow in organic liquid droplets [54]. Hu and Larsen [55] speculated that the flow pattern associated with surface-tension-driven convection in organic droplets inhibits the so-called “coffee-ring” deposition [41] that is observed following complete evaporation of water droplets. While substrate temperature manipulation [6] and the introduction of surfactants [56] have been used to localize deposition of suspended particulates during water droplet evaporation, the inherently localized deposition offered by organic fluids is an attractive alternative for inkjet patterning applications [8].

Evaporative transport in organic droplets on wetting substrates has been studied extensively, including the mechanisms that drive the observed flow patterns [54] and the influence of the substrate conductivity on the direction of flow recirculation and temperature distribution within the droplet [57,58]; predictive modeling approaches [59–61] have also been developed that include

pertinent flow convection mechanisms. The flow field has been quantitatively visualized using out-of-focus particle tracking [55] and particle displacement tracking [62] methods. Qualitative flow visualizations have also been conducted for various organic fluids using infrared thermography [32,63] by taking advantage of the semi-transparency of organic liquids in the infrared spectrum to view thermal convection within the droplet. We note that evaporation rates can be accurately predicted under the assumption that thermal transport occurs purely by conduction [64,65] inside volatile droplets on a wetting substrate.

To enable low-surface-tension organic liquid droplets to rest on a solid surface in a nonwetting state, the substrate must have specialized reentrant roughness, such as inverse trapezoidal [66], serif-T [67], mushroom [68], micro-hoodoo [69], and micro-nail [70] structures. On such reentrant structured surfaces, the meniscus of the liquid droplet pins at the sharp edge of the microstructure and exerts a net upward force that opposes impalement of the droplet by the microstructures, even for low-surface-tension liquids. While many studies have investigated water-droplet evaporation on nonwetting substrates [44,71], organic liquid droplet transition from a non-wetting to a wetting state *en route* to complete evaporation has only been considered by Chen *et al.* [72]. There have been no quantitative visualizations of the convection patterns within evaporating organic liquid droplets on nonwetting substrates. While only conduction needs to be considered in organic liquid droplets on a wetting substrate (convection can be neglected in wetting droplets due to their low height-to-contact-diameter ratio [64,65]), this simplification may not hold for droplets on nonwetting surfaces. In view of the sparse literature related to organic liquid droplets evaporating on nonwetting substrates, which take on a significantly different droplet shape, it is necessary to quantitatively visualize the flow field and assess the predominant transport mechanisms.

#### **2.4 Miniaturized Colorimetric Analysis of Protein Concentration**

The Bradford assay is one of the most commonly used protein quantitation techniques. The technique involves mixing a protein-containing sample with the reagent dye Coomassie<sup>TM</sup> Brilliant Blue G-250. This reagent dye is known to exist in three ionic states: anionic, cationic, and neutral [73]. The neutral and anionic states both react to the amino acids in the protein, the former by hydrophobic and electrostatic interactions, and the latter by electrostatic interactions [74]. These reactions form protein–dye complexes that shift the absorbance spectrum of the mixture.

The measured absorbance change is correlated with a set of standard concentrations to determine the protein concentration in the sample by correlation [75]. The non-instantaneous nature of this reaction means that there is likely a combined effect of the reaction and the mixing in the apparatus on the measurement timescale. In conventional Bradford assays that are conducted in macroscale cuvettes, the measurement requires on the order of 5 min to for the reaction to complete [76], likely due to the time limitations of mixing in macroscale devices. Macroscale mixing also raises concerns of protein denaturation and foaming with excessive vortexing [77]. A quicker method of mixing that avoids denaturation, as is possible at the smaller length scales of micromixing techniques, can allow the reaction to be completed more rapidly.

Several techniques are presented in the literature for miniaturized colorimetry, with microfluidic electrowetting-on-dielectric (EWOD) devices [78] and paper-based devices [79] representing a majority of the efforts. Some devices rely on EWOD as an actuation method for transporting droplets to a sensor [78,80]. This approach typically involves use of a hydrophobic substrate to ease the actuation of the droplet. A process of shuttling the droplet is utilized to ensure mixing of the sample and reagent. A significant issue facing the use of hydrophobic substrates is the irreversible adsorption of hydrophobic proteins onto the substrate, causing contamination of the sample and device [81]. This is often mitigated using oil as a separation layer [82]. Paper-based microfluidic devices rely on capillary action to drive the fluids [79]. This approach provides the benefit of low-cost, passively-driven flow. Some of the limitations of this approach includes low sample flow efficiency, potential for leakage, and inability to measure extremely low concentrations [83]. Finally, a sessile droplet-based technique was recently demonstrated for a *hue-based* colorimetry system that relies measuring the color of the sample near completion of evaporation [84]. *Absorbance-based* colorimetry (which is crucial for many commonly used techniques like the Bradford assay, the Lowry assay, etc.) has not been previously explored using sessile droplets.

Recent efforts have attempted high-throughput screening using absorbance-based colorimetry by fabricating miniaturized wells with higher density of wells per unit area [85]; however, these techniques require complex machining to create precise wells and maintain low footprints. Furthermore, a key issue that has to be addressed in these low-volume microwells is mixing the samples thoroughly [86]. Several active micromixing approaches have been proposed in literature,

including ultrasonication [87], vibrations from T-junction microchannels [88], magnetohydrodynamic stirrers [89], and electro-osmotic flow in microchannels [90]. Most of these approaches require complex control schemes and additional manufacturing requirements. Multilaminar mixing is another approach that uses intricate patterns of channels to induce chaotic flows [91]. These techniques often require longer flow lengths [88] and still require complex fabrication to create the complex flow patterns necessary for mixing. As such, a simpler micromixing system would benefit high-throughput microplate-based colorimetric analysis.

Several characteristics of droplets on nonwetting surfaces make them an attractive platform for miniaturized colorimetry. Droplets on nonwetting surfaces demonstrate significantly lower evaporation rates than droplets on wetting substrates [92]. This is due to the suppression of evaporation at the contact line of the droplet due to vapor confinement [92] combined with evaporative cooling [93,94]. This suppression is an important feature for colorimetric applications, where the reaction needs to be completed and the absorbance measurement taken before the droplet significantly evaporates. Furthermore, aqueous droplets demonstrate buoyancy-driven convection on nonwetting substrates [95], which offers an order of magnitude higher internal flow velocities [95] compared to wetting surfaces [41]. This leads to buoyancy-induced mixing rates that are two orders of magnitude higher than simple diffusion-based mixing [95], without requiring long flow lengths as in other passive micromixers. This aspect of the droplet-based system reduces the time to complete the reaction between the dye and the reagent. Finally, sessile droplets of known volumes and contact angles can be simply placed on a hydrophobic substrate, taking on a shape having a small footprint without the need for complex fabrication of microplates.

## **CHAPTER 3. QUANTITATIVE ANALYSIS OF ERROR REDUCTION IN EMISSIVITY MAPPING AND INFRARED THERMOGRAPHY BY MULTIFRAME SUPER-RESOLUTION**

In this study, we explore the application and performance of multi-frame super-resolution for quantitative thermographic measurement applications. Furthermore, the impact of multi-frame super-resolution on improved feature resolution and accuracy of emissivity maps is demonstrated using an electronic component as a sample. Sources of error in multi-frame super-resolution measurements, including registration uncertainty and smoothing effects on emissivity boundaries, are quantified. Finally, the limits of feature size recapture using multi-frame super-resolution are explored as a function of the native resolution of the camera. This study aims to determine the benefits and limits of multi-frame super-resolution in thermographic applications. The material presented in this chapter was published in the *Journal of Electronic Packaging* [96]. The experimental measurements described in Chapter 3.1.1 were performed in collaboration with Sara Lyons.

### **3.1 Materials and Methods**

#### **3.1.1 Infrared Measurement Setup**

The experimental facility, shown in Figure 3.1, is designed to allow acquisition of sub-pixel shifted infrared images of a sample for multi-frame super-resolution reconstruction. A computer memory card is used as the sample to demonstrate this technique. The sample is placed on a thin film heater (Omegalux KHLV-105/10-P) that is thermally insulated on the back side. A thermocouple is used to measure the surface temperature of the sample surface; a set temperature is maintained using a feedback temperature controller (Temp-o-Trol TOT-1200). The heater assembly is mounted on two differential micrometer stages that allow displacement of the sample in the  $x$  and  $y$  directions with a positional resolution of  $0.5 \mu\text{m}$ . A mid-wavelength infrared camera (FLIR SC7650;  $1.5\text{--}5.1 \mu\text{m}$ ) is mounted orthogonal to the sample. The  $25 \text{ mm}$  focal length lens (Janos Asio F/2.3 MWIR) is fitted with a  $6.35 \text{ mm}$  extension tube to achieve a pixel resolution of  $144.3 \mu\text{m}$ . The camera records at  $100 \text{ Hz}$  with an integration time of  $750 \mu\text{s}$ . The ambient temperature during image capture was  $21.2 \text{ }^\circ\text{C}$  and the relative humidity was  $24 \pm 3\%$ .

The camera calibration was conducted using a differential blackbody calibrator (SBIR DB-04) with an effective surface emissivity  $\geq 0.97$ . The calibration was performed to span the expected range of surface temperatures and fit using a fourth order polynomial curve. The nonuniformity of the camera is also corrected using these blackbody measurements and the calibration curve generated for each pixel. The capture settings for the camera match those used in the experiments. For uncertainty analysis, the error covariance method is utilized, as described by Bevington and Robinson [97]. The infrared sensor measurement uncertainty was found to be  $0.41\text{ }^{\circ}\text{C}$  for a black surface. Detailed procedures of both the camera calibration processes and uncertainty analysis can be found in APPENDIX B.1.

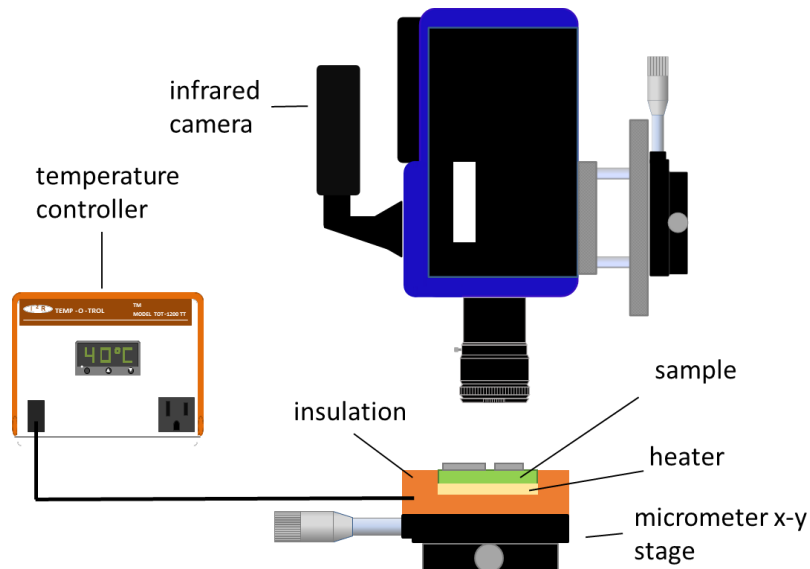


Figure 3.1. Schematic diagram of the experimental setup used for the multi-frame super-resolution infrared measurements.

Experiments are conducted by setting a desired sample surface temperature using the heater and temperature controller. Once the temperature of the sample stabilizes at the set temperature, the infrared data are captured at the camera pixel resolution (referred to as the ‘low-resolution’ images). To capture data for the multiframe reconstruction, the sample is displaced by  $25\text{ }\mu\text{m}$  increments in a five-by-five grid to generate 24 additional low-resolution images in sub-pixel shifts with respect to the center image.

Nonuniform interpolation [12] is a simple approach for reconstruction of the high-resolution image that has the benefit of low processing time [11]. This method is simplified further because the subpixel displacement of images are known *a priori* from the micrometer stage position. In order to conduct the super-resolution reconstruction, all of the low resolution data from each image is mapped onto a single two-dimensional plot. Every pixel position in each image is mapped onto the  $x$ - $y$  plot, accounting for the relative subpixel displacement of each image with respect to the center image. A high-resolution grid with five times the resolution of the low-resolution image is chosen for the super-resolution image reconstruction. The data is then interpolated into this high-resolution grid using a triangulation-based natural neighbor scheme, thus generating the super-resolution image. This image is then conditioned with a Gaussian noise filter. This super-resolution reconstruction algorithm was implemented in MATLAB [98].

### 3.1.2 Emissivity Mapping

A two-temperature approach [99] is used for emissivity mapping. In this two-temperature technique, infrared calibration images are recorded of the sample after it is uniformly heated at two different temperatures, in this case room temperature and 50 °C; a blackbody is also characterized at the same two temperatures. The directional radiance of the sample is calculated for each heating condition using the Planck equation integrated over the wavelength range of the camera sensor:

$$J_{1.5-5.1\mu m}(T_{read}) = \int_{1.5\mu m}^{5.1\mu m} \frac{2hc^2}{\lambda^5} \frac{1}{\frac{hc}{\lambda k_b T_{read}} - 1} d\lambda \quad (D.1)$$

where  $J$  denotes the sample radiance,  $h$  is the Planck constant,  $c$  is the speed of light,  $\lambda$  is the wavelength,  $k_b$  is the Boltzmann constant, and  $T_{read}$  is the uncorrected temperature (from the infrared camera before emissivity correction). The emissivity is then calculated using:

$$\varepsilon_s = \frac{J_2 - J_1}{J_{b2} - J_{b1}} \quad (D.2)$$

where the subscripts 1 and 2 respectively refer to the sample conditions at the first and second temperature, and subscripts b1 and b2 respectively refer to a blackbody at the first and second

temperature. Due to the relatively small temperature range explored in this study, the spectral emissivity characteristics are not expected to change dramatically. Therefore, the sample is assumed to behave as a grey body over the temperature and wavelength range explored in this study. Another important quantity to calculate is the reflection of ambient radiation sources, particularly on the low-emissivity materials. This quantity is estimated using:

$$J_{app} = \varepsilon_s J_{surf} + (1 - \varepsilon_s) J_{amb} \quad (D.3)$$

where  $\varepsilon_s$  is the surface emissivity,  $J_{app}$  is the apparent radiance of the surface,  $J_{surf}$  is the actual radiance from the surface, and  $J_{amb}$  is the radiance from the ambient. Because the true temperature of the two calibration images is known and uniform, the ambient radiance is iteratively calculated through Equation (D.3) until the standard deviation of the temperature map for each calibration case is minimized. The background is assumed to behave as a diffuse, uniform source.

In order to demonstrate the improvement in mapping with the multiframe super-resolution data, this emissivity mapping is conducted with both the low-resolution data as well as the super-resolution data. The temperature correction is conducted using the Newton-Raphson method to solve Equations (D.1) and (D.3) and find the true temperature of the sample surface. These emissivity mapping and temperature correction algorithms were implemented in MATLAB[98].

### 3.2 Simulated Images

When simulating multiframe super-resolution using artificial images, for purposes of investigating boundary smoothing effects and feature recapture, a ‘scene image’ of extremely high resolution is first generated. The low-resolution simulated ‘camera image’ is captured from this scene using a pixel size chosen to be significantly larger than the scene pixel size. A camera position with respect to the scene center is chosen. The scene image is subsequently downsampled to the camera resolution, centered on the camera position. This represents a single low-resolution image captured by the simulated camera. When generating multiple low-resolution images that are shifted by a sub-pixel resolution, the camera position is displaced by a fraction of the camera pixel size and a low-resolution image is similarly captured. In order to simulate the experimental approach, the low-

resolution images are captured in a five-by-five grid and used to reconstruct a simulated super-resolution image with five times the resolution of the low-resolution image.

### **3.3 Results and Discussion**

Experimental results are first presented followed by results of the simulation. The experimental results are based on infrared imaging of electronic components as well as patterned surfaces in order to demonstrate the practical value of multiframe super-resolution in capturing complex features and accurate emissivity mapping. A sensitivity analysis is conducted to demonstrate the effect of registration uncertainty on the accuracy of the super-resolution reconstruction, based on the experimental images. The simulation uses artificial images in order to investigate the effects of multiframe super-resolution on smoothing at boundaries and feature size recapture, compared to low-resolution images.

#### **3.3.1 Experimental Results**

##### **3.3.1.1 Experimental Image**

The benefits of multiframe super-resolution are qualitatively demonstrated with experimental images shown in Figure 3.2. Due to the different emissivities of the wire traces, printed circuit board material, and various components on the surface, the uncorrected infrared intensity map shown in Figure 3.2 is highly nonuniform, despite the sample being maintained at a uniform temperature of 40 °C. By interrogating the infrared images in a region of the device with serpentine wire trace patterns, there are significant aliasing effects in these thin line features in the low-resolution image (Figure 3.2(c)); however, the super-resolution reconstruction in Figure 3.2(d) recaptures lost curvature and portions of the wire trace pattern. The apparent pixelation in the low-resolution images is also smoothed by the super-resolution algorithm.

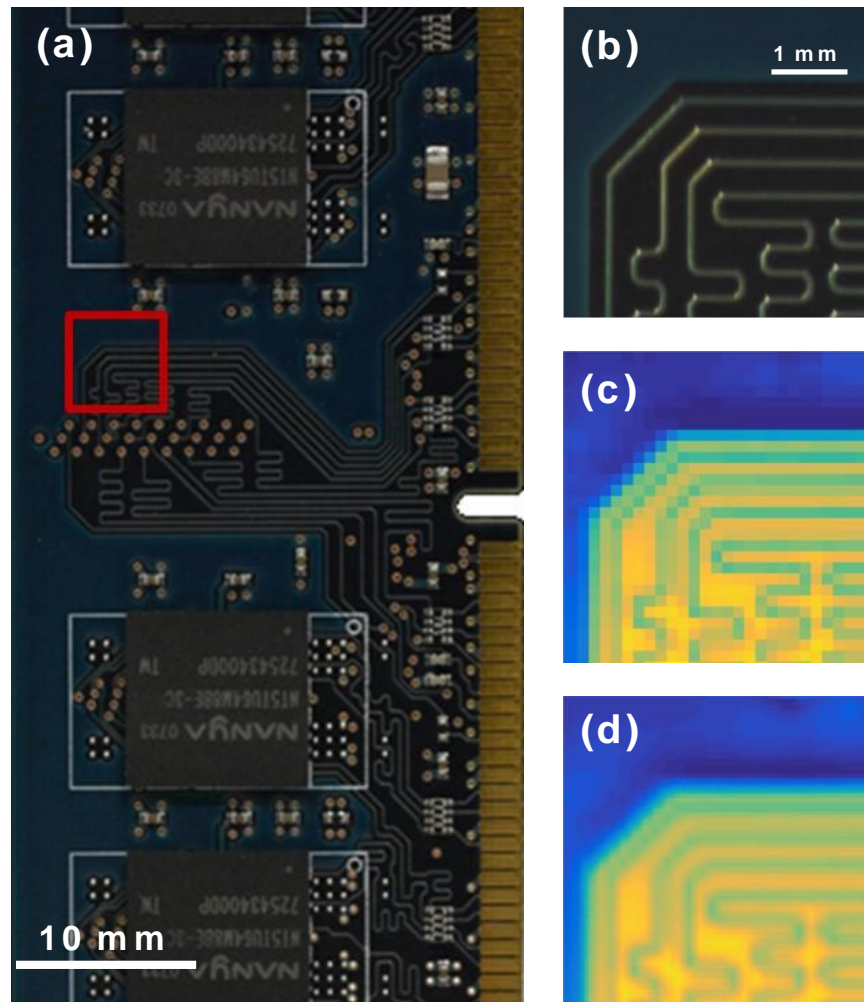


Figure 3.2. (a) Photograph of the computer memory card used to demonstrate multi-frame super-resolution reconstruction. (b) An inset photograph of a serpentine wire trace feature with (c) the corresponding low-resolution and (d) multi-frame super-resolution infrared intensity maps.

### 3.3.1.2 Emissivity Mapping

When considering the benefits of multi-frame super-resolution for quantitative temperature measurements with infrared thermography, a key step is emissivity mapping to correct for the nonuniform emissivity of the sample.

Figure 3.3 shows the uncorrected and emissivity-corrected temperature maps for both the low-resolution and super-resolution data. The sample is maintained at a uniform temperature, but due to the emissivity variation on the sample surface, the uncorrected infrared intensity measurement (Figure 3.3 (a/c)) is nonuniform. Figure 3.4 shows the emissivity maps generated for this sample

using the two-temperature approach. After generating an emissivity map of the sample, a corrected temperature map is obtained (Figure 3.3(b/d)). Because the sample is known to be at a uniform temperature, the standard deviation of the temperature across the sample surface offers a metric for the effectiveness of the emissivity correction. For the cases shown in Figure 3.3, the low-resolution image has a standard deviation of 1.1 °C, while the super-resolution has a significantly reduced standard deviation of 0.7 °C. This demonstrates that super-resolution reconstruction better recovers the emissivity-corrected surface temperature, compared to a low-resolution image captured at the native resolution of the camera.

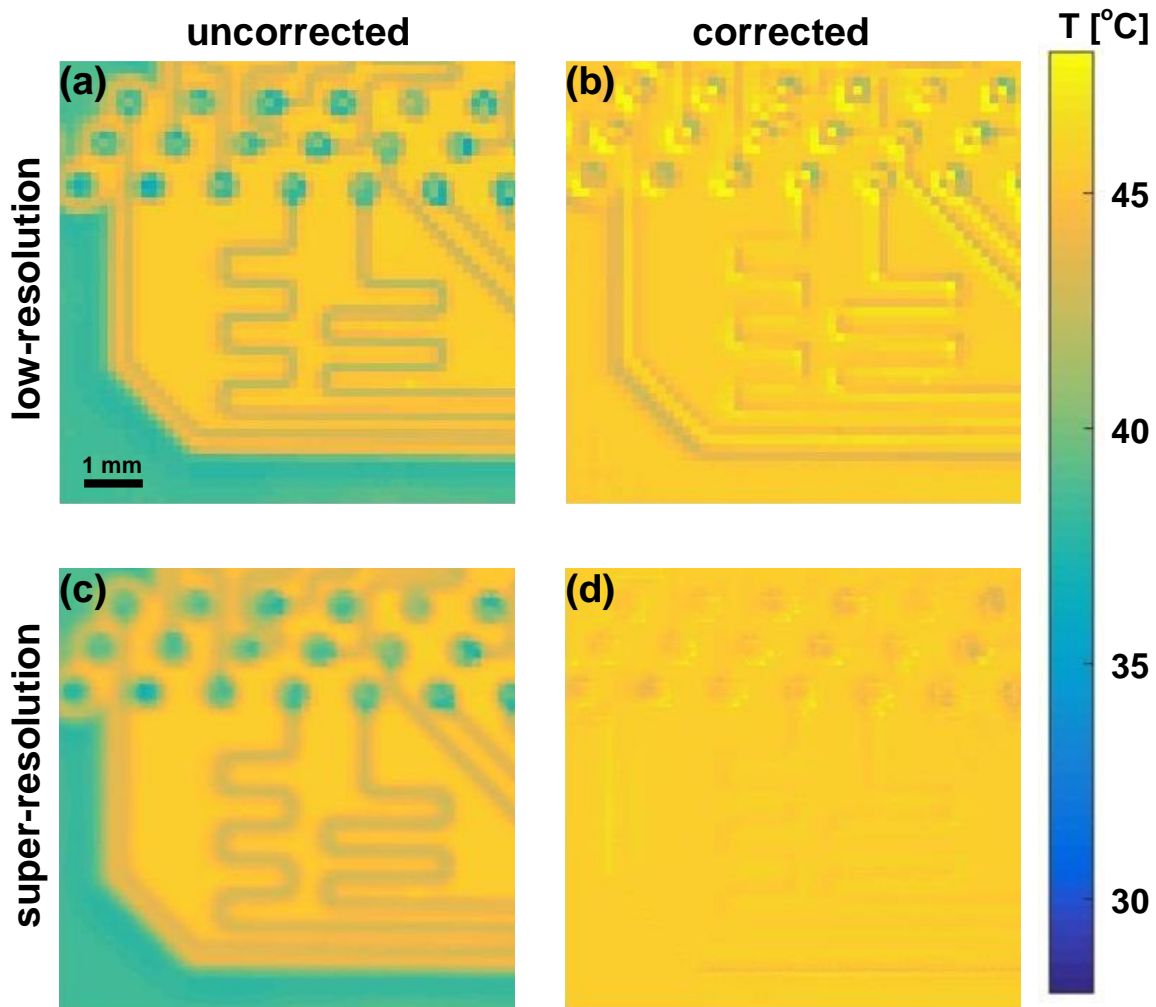


Figure 3.3. (a) Uncorrected and (b) emissivity-corrected low-resolution temperature maps, as well as (c) uncorrected and (d) corrected multi-frame super-resolution maps of a portion of the component shown in Figure 3.2.

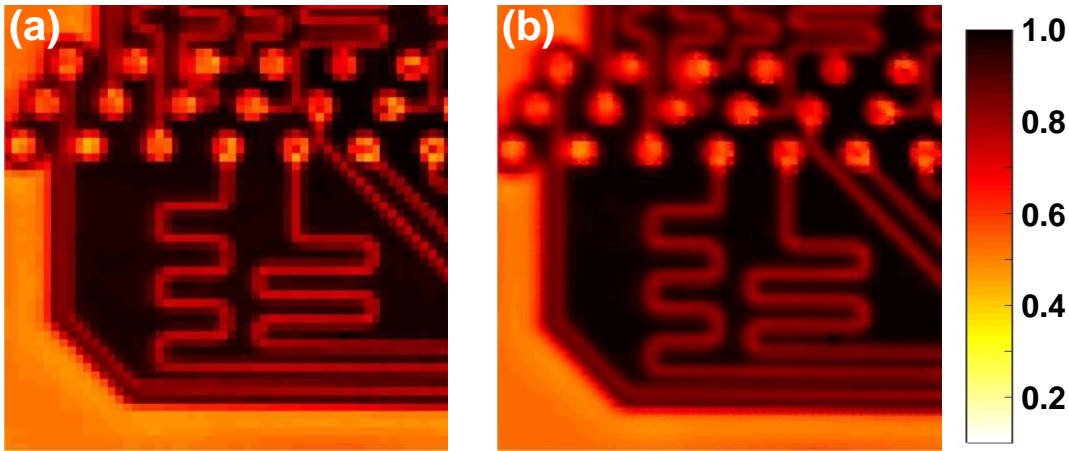


Figure 3.4. Emissivity maps generated using the (a) low-resolution and (b) super-resolution images.

### 3.3.1.3 Registration Uncertainty

One significant source of uncertainty in the pixel values of the reconstructed images is the ‘registration uncertainty’ of the low-resolution images. That is, if the relative shifted positions of the low-resolution images are uncertain, this error will propagate through the reconstruction interpolation. In order to explore the impact of this uncertainty, a sensitivity analysis is conducted based on an infrared measurement of a black surface with painted gold bands. This surface is chosen to provide an example of a binary emissivity distribution with clear emissivity boundaries. Images are acquired using the same experimental procedure as described in Section 3.1.1, except that the lens is fitted with a 19.05 mm tube to yields a pixel resolution of 38.1  $\mu\text{m}$ . The relative positions of the low-resolutions images are randomly perturbed based on a normal distribution spanning the selected registration uncertainty value. The multiframe super-resolution reconstruction, generated using the perturbed images, is then compared to the unperturbed reconstruction; the maximum deviation across the reconstructed image is calculated and recorded. This randomized test is repeated 500 times, after which the error converged. In order to further explore the general impacts of registration uncertainty, several registration uncertainty values, including values exceeding the size of the pixel, are used in the same manner as described above. One of the selected uncertainty values is the actual uncertainty of the differential micrometer stages (0.5  $\mu\text{m}$ ) used in the experiments.

Figure 3.5 plots the maximum deviation as a function of the registration uncertainty. For reference, the calibrated measurement uncertainty of the infrared camera ( $0.41\text{ }^{\circ}\text{C}$ ) is shown as a horizontal line. When the registration uncertainty is below half a pixel size, it has a very small effect on the measurement uncertainty. At values exceeding this threshold, the measurement uncertainty starts to exceed the uncertainty of the infrared measurement. For infrared thermography applications, it is expected that the registration uncertainty can be restricted to within this half-pixel threshold, limiting the concern regarding error induced by registration uncertainty. This is attributed to the *a priori* knowledge of the camera position when acquiring subpixel shifted frames, compared to the more significant registration uncertainty concerns during remote viewing [100] and underwater imaging [101], for which the shifts can be large compared to the pixel size.

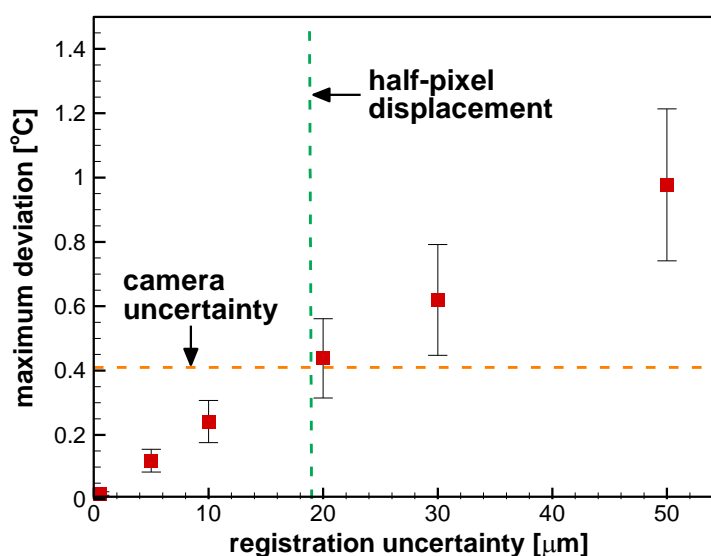


Figure 3.5. Maximum deviation based on a sensitivity analysis of input sensitivity values are plotted.

### 3.3.2 Simulation Results

#### 3.3.2.1 Boundary Smoothing Effect

The smoothing effect at feature boundaries, due to the interpolation of the data, is a potential concern for multiframe super-resolution reconstruction, particularly at sharp emissivity boundaries. In order to quantify this effect, test scenes having either smooth waves (sinusoidal) or sharp bands (square) with varying frequency are simulated. The temperature values are nondimensionalized

(with maximum values of 1 and minimum values of 0) in order to render the results in a generalized form using:

$$\theta = \frac{T - T_{min}}{T_{max} - T_{min}} \quad (\text{D.4})$$

where  $\theta$  is the nondimensionalized temperature,  $T$  is the local temperature,  $T_{min}$  is the minimum temperature, and  $T_{max}$  is the maximum temperature. Simulated low-resolution images are captured assuming a camera pixel size that is 10 times the scene pixel size. A plot of the intensity is taken from a horizontal line along each image (scene, super-resolution, and low-resolution) to assess the super-resolution performance. Figure 3.6 shows the scene images used for the smooth waves and the sharp bands. Line plots from the horizontal centerline of the scene image, the super-resolution image, and the low-resolution image are shown below the respective scene images. As seen in Figure 3.6(a), the super-resolution image noticeably outperforms the low-resolution image at capturing smooth features, particularly the thinner features, where aliasing effects dominate the low-resolution data. The mean error across the image is 0.011 for the super-resolution reconstruction and 0.069 for the low-resolution image. In Figure 3.6(b), the relative improvement offered by the super-resolution image, compared to low-resolution, is moderated due to the smoothing of the sharp boundaries; nevertheless, quantitatively, the super-resolution still significantly outperforms the low-resolution capture (with mean respective errors of 0.065 versus 0.092).

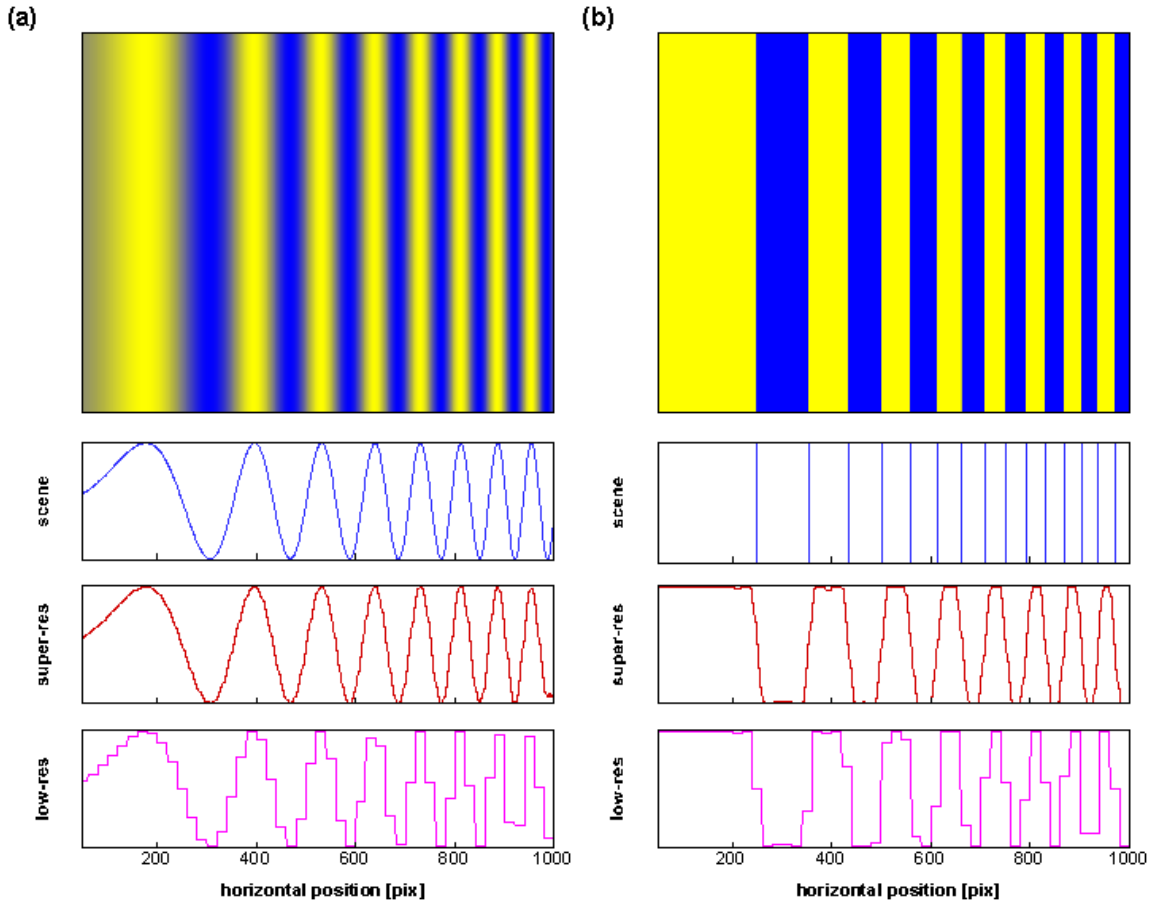


Figure 3.6. The (a) smooth wave and (b) sharp band scenes of nondimensionalized temperature are shown above horizontal line plots of the scene, multiframe super-resolution image, and low-resolution image.

### 3.3.2.2 Feature Size Recapture

The effectiveness of multiframe super-resolution in capturing features of differing sizes, relative to the low-resolution pixel size, is quantitatively explored. In order to investigate the performance of super-resolution across a wide range of feature sizes, simulated images are used to quantify the relative performance with respect to low-resolution images. A two-dimensional test image is generated that features alternating sharp bands of high and low temperatures (*i.e.*, from 0 to 1 to represent nondimensionalized temperature) of widths ranging from much lower to much larger than the low-resolution pixel size. A similar test is also conducted with smooth waves with the same value range to represent smoother images. The test scene images have a resolution that is 10 times the simulated camera resolution.

The simulated low-resolution and super-resolution images are compared to the test scene, to assess the error. The standard deviation of the difference between the image and the scene is used as an error metric. Figure 3.7 displays the absolute errors of the low-resolution and super-resolution reconstruction for the sharp bands and smooth waves. To better illustrate the relative performance of super-resolution, the difference between the low-resolution and super-resolution error (*i.e.*, error difference) for the sharp bands is plotted in Figure 3.8(a) and for the smooth wave in Figure 3.8(b). The error difference, a measure of super-resolution algorithm performance, is plotted as a function of the pixel-to-feature size ratio, defined as the ratio of the pixel size to the band (or wave) width (see Figure 3.8(a) inset). As demonstrated in Figure 3.8, the error difference is at a maximum at a pixel-to-feature size ratio of 0.76. Near this peak, super-resolution reconstruction is able to recapture details and borders of features that are lost due to an offset between the camera pixel and the feature, resulting in significant reduction in the error by up to 0.165 compared to image capture at the native resolution (for the scene that has a maximum value of 1). When the pixel-to-feature-size ratio is above 1, the error difference converges to 0, indicating that super-resolution provides no performance improvement compared to the low-resolution image. This is a result of the fact that the feature data from the low-resolution images are too degraded for the super-resolution to recover any information. On the other end of the test range, at very small pixel-to-feature size ratios, the error difference asymptotes at 0, because the low-resolution image has sufficient resolution to capture the relevant feature data within the scene, such that super-resolution provides no additional information.

The effect of image noise is an important practical consideration for the feature size recapture and quantitative performance improvement of the super-resolution. To investigate this effect, a Gaussian noise profile is applied to the low-resolution simulated images to model camera noise. The standard deviation of the noise profile is selected such that the value of three standard deviations represents the selected maximum noise value. The super-resolution reconstruction is identical to the approach used for the cases without noise. Figure 3.8(c,d) show the results for cases with 10% maximum noise for both sharp bands and smooth waves. The results in Figure 3.8(c) show that a 10% maximum noise slightly reduces the performance improvement of the super-resolution algorithm for square bands (the maximum error difference is 0.14 compared to 0.165 without noise); the trends in the maximum error difference with pixel-to-feature size ratio are not changed. As a point of reference, it should be noted that the camera used in the experiments

showed a maximum noise of  $0.06\text{ }^{\circ}\text{C}$ , which, nondimensionalized, amounts to approximately 6%. Figure 3.8(d) shows that the effect of image noise on the error difference is significantly smaller for the smooth wave scene compared to the square bands. Furthermore, unlike the case without noise, the super-resolution technique shows improvements for lower pixel-to-feature size ratios in the smooth data. This is due to the smoothing effect of super-resolution on the noise in the low-resolution images.

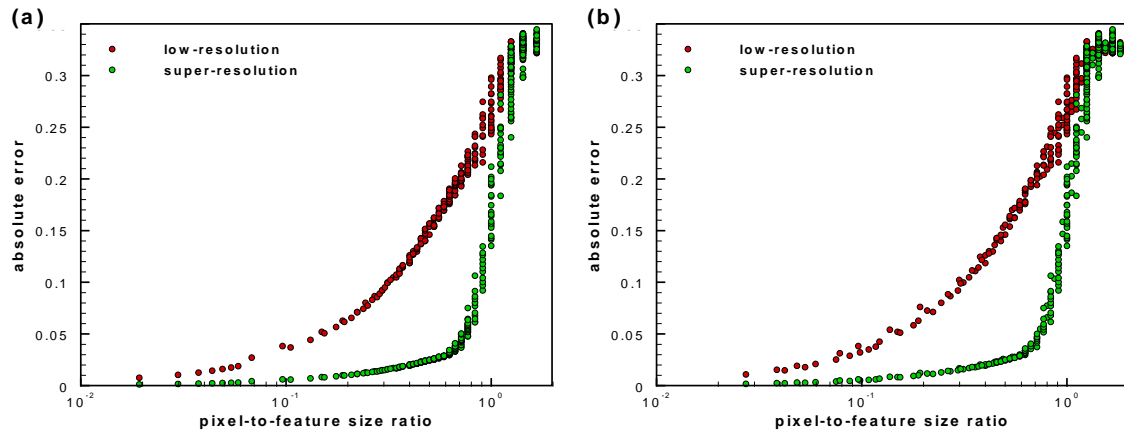


Figure 3.7. The absolute errors for the low-resolution and super-resolution images of the nondimensionalized temperature are shown for the (a) sharp bands and (b) smooth wave scenes.

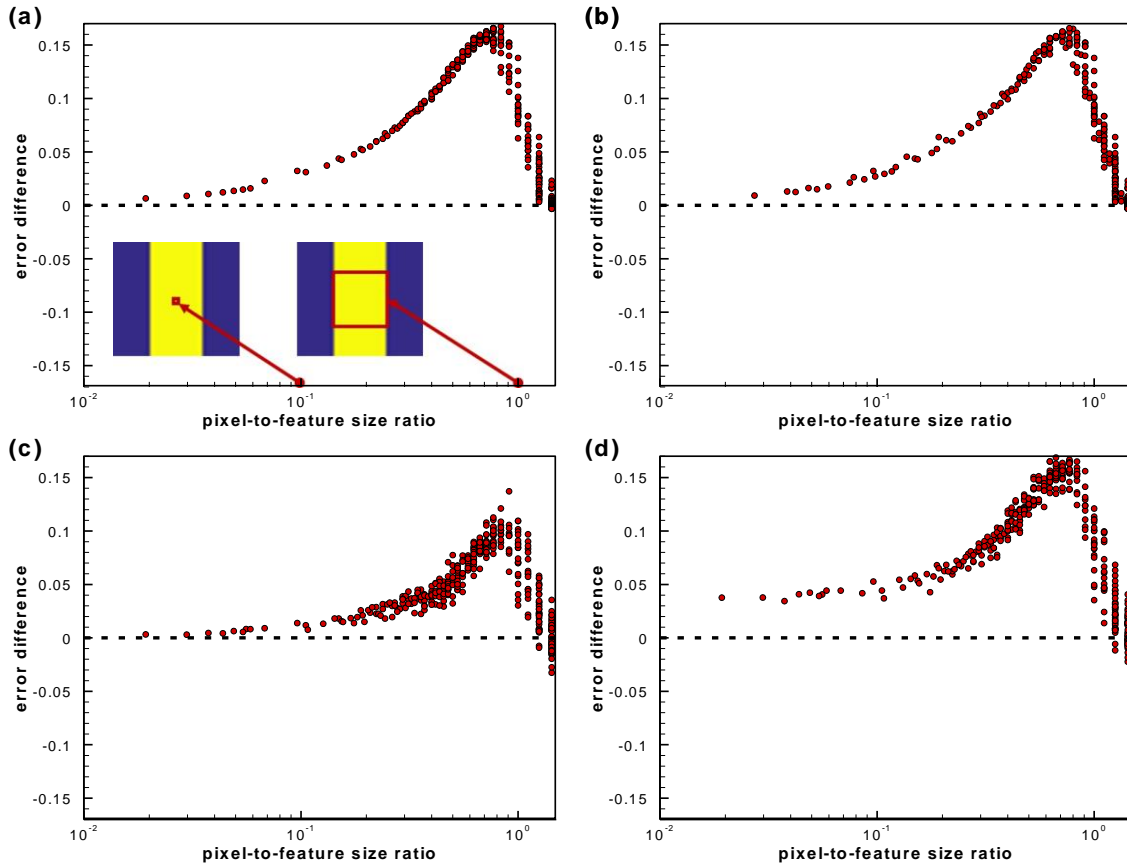


Figure 3.8. The difference between the error of the low-resolution and multiframe super-resolution images of the nondimensionalized temperature plotted as a function of the pixel-to-feature size ratio for the (a) sharp bands and (b) smooth wave scenes. The results with 10% maximum image noise are plotted for the (c) sharp bands and (d) smooth waves. The insets in (a) illustrate example pixel size relative to the band feature.

### 3.4 Conclusion

The performance of multiframe super-resolution for quantitative infrared thermography measurements has been explored. A demonstration case of the emissivity mapping shows that the super-resolution reconstruction corrects for emissivity nonuniformity more effectively than is possible with low-resolution images. It is also shown that the sensitivity of the image reconstruction to uncertainty in the registration of subpixel shifted frames is generally a minor concern when the camera position is known *a priori*. Through analysis of simulated image capture, it is demonstrated that super-resolution reconstruction yields a quantitative reduction in error when capturing a scene compared to the low-resolution capture, despite introducing a smoothing effect at sharp boundaries. Furthermore, we show that super-resolution provides the most benefit for

recapture of features that are near the size of the native pixel resolution of the optical system. Camera noise can lower the peak performance of super-resolution but is mitigated by the smoothing effect of super-resolution at larger feature sizes. Multiframe super-resolution provides a simple means to improve the native measurement resolution of infrared cameras for quantitative thermographic applications.

## CHAPTER 4. SPATIOTEMPORAL INFRARED MEASUREMENT OF INTERFACE TEMPERATURES DURING WATER DROPLET EVAPORATION ON A NONWETTING SUBSTRATE

This chapter demonstrates calibrated infrared measurement of the temperature distribution on the surface of droplets evaporating on nonwetting substrates over a range of temperatures. The temporal evolution of droplet volume, contact angle, temperature profiles along the droplet height, and the evaporation rate are simultaneously tracked. This builds on past work in on droplet evaporation dynamics and the mechanisms for the thermal resistance within a water droplet on a nonwetting substrate [5]. These studies showed that conduction resistance is the primary mechanism of thermal transport along the vertical axis of the droplet; however, there is no direct measurement of the temperature profiles to confirm this trend. This study aims to address this need and investigate the influence of other thermal mechanisms in the vertical temperature profile of a droplet. The material presented in this chapter was published in *Applied Physics Letters* [94].

### 4.1 Materials and Methods

The nonwetting copper substrate used in this study was fabricated in the Birck Nanotechnology Center at Purdue University. The substrate was immersed in an aqueous solution of 2M NaOH and 0.1 (NH<sub>4</sub>)<sub>2</sub>S<sub>2</sub>O<sub>8</sub> for 60 min to etch copper oxide nanostructures. It was then rinsed with deionized water and dried with N<sub>2</sub> gas. To attain superhydrophobicity, the nanostructured surface was immersed in a 0.001 M n-hexane solution of 1H, 1H, 2H, 2H-perfluorooctyltrichlorosilane (PFOS) for 60 min followed by heat treatment on a hotplate at ~150°C for 60 min. A localized surface indentation is introduced to provide a consistent location where the droplet pins to the substrate to allow for repeatable visualization.

The experimental facility used to capture the infrared images of evaporating droplets is shown in Figure 4.1. The substrate is held at a fixed temperature by attaching it to an insulated copper block that is heated from the bottom by a polyimide heater with a feedback temperature controller (TOT-1200, Temp-O-Trol). In order to maintain consistent background radiation, a black-painted (ColorMaster™ Flat Black, Krylon; emissivity of 0.97) aluminum shield surrounds the droplet. The temperature of the metal shield is maintained using a temperature-controlled thermoelectric

cooling stage (CP-031HT, TE Technology, Inc.). All experiments were conducted with the shield held at  $20 \pm 0.1$  °C. The ambient relative humidity was  $28 \pm 3\%$ .

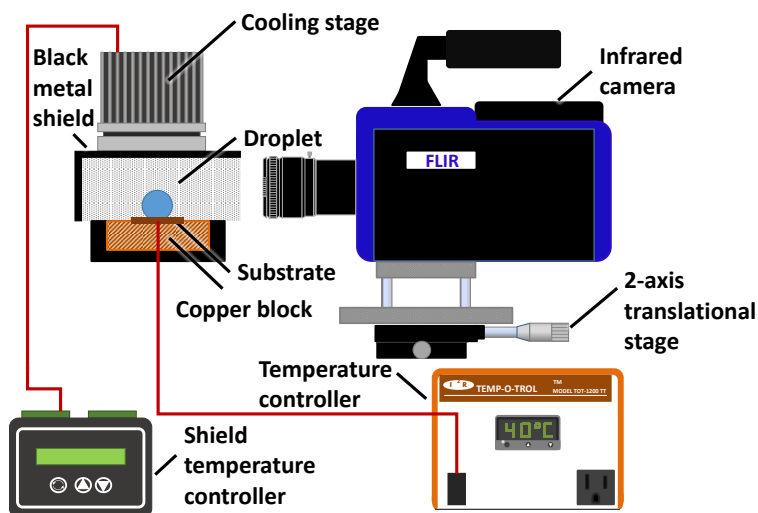


Figure 4.1. Schematic diagram of the experimental facility.

The temperature of the droplet surface is measured with an infrared camera (SC7650, FLIR). A 50 mm lens (Nyctea, Janos) that is fitted with 30 mm of extension tubes yields a magnification of  $\sim 0.76$ . This lens and camera system captures radiation in the mid-wavelength infrared range ( $1.5 \mu\text{m}$  to  $5.1 \mu\text{m}$ ), which coincides with the peak emission wavelength (*viz.*,  $3 \mu\text{m}$ ) of water [34]. Further details on the blackbody calibration, uncertainty assessment, and validation of infrared temperature measurement of water-air interfaces are included in APPENDIX B.1. The uncertainty of the infrared temperature measurement is  $0.41$  °C [94]. The camera records frames at 5 Hz.

To perform an experiment, a water droplet of approximately  $4 \mu\text{L}$  is deposited on the heated substrate using a pipette (AP-10, AccuPet). At the volumes used, the effects of gravity on the interface curvature can be neglected and the droplet assumes a spherical cap geometry. The droplet is allowed time to settle after being placed on the surface; temperature data are only presented from the time the droplet volume has reduced to  $3 \mu\text{L}$  until complete evaporation. Five repeated droplet evaporation trials are performed at each of four different fixed substrate temperatures:  $30 \pm 0.5$  °C,  $40 \pm 0.5$  °C,  $50 \pm 0.5$  °C, and  $60 \pm 0.5$  °C.

## 4.2 Results and Discussion

### 4.2.1 Raw Data Analysis

The infrared visualizations of the droplet are used to simultaneously track the droplet temperature and shape throughout the evaporation process, as shown in Figure 4.2. The droplet contact diameter and height are measured at each frame and used to calculate the droplet volume and contact angle based on geometric relations for a spherical cap shape. The volume and contact angle evolution of the droplets are plotted with respect to time in Figure 3 at intervals of ~30 sec. As shown in Figure 4.3(a), the volume decreases in a similar, exponential trend to those reported in literature [5,49]. The evaporation rate increases significantly with increasing substrate temperature. The contact line remains pinned and the evaporation primarily follows a constant-contact radius mode; as shown in Figure 4.3(b), the contact radius is nearly constant during the course of evaporation. The contact angle continuously decreases *en route* to complete evaporation.

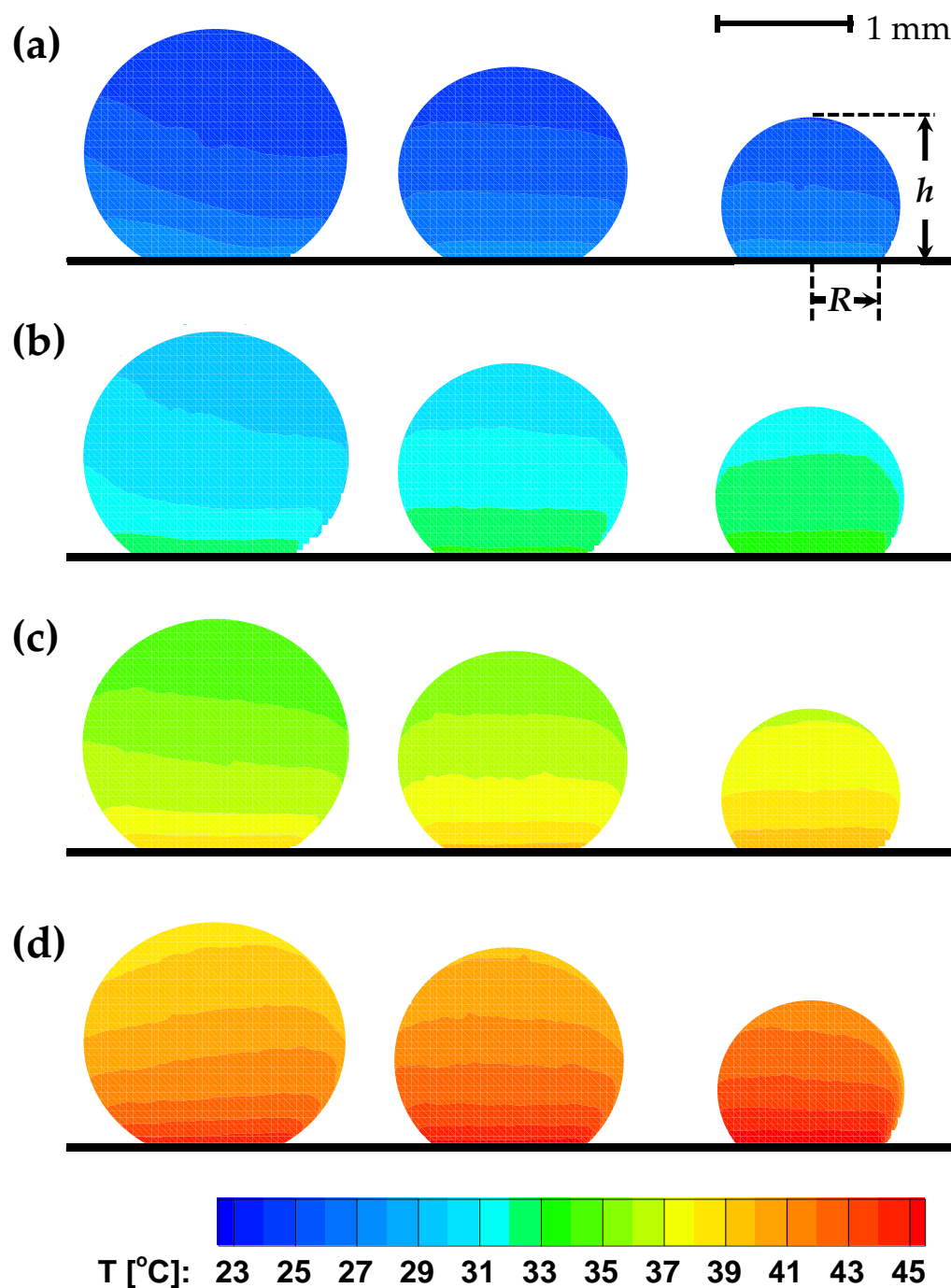


Figure 4.2. The uncorrected infrared temperature data are shown for droplet evaporation trials at substrate temperatures of (a) 30 °C, (b) 40 °C, (c) 50 °C, and (d) 60 °C; from left to right, the panels show droplet volumes of 3 μL, 2 μL, and 1 μL. The contact radius,  $R$ , and the droplet height,  $h$ , are marked for the top right case.

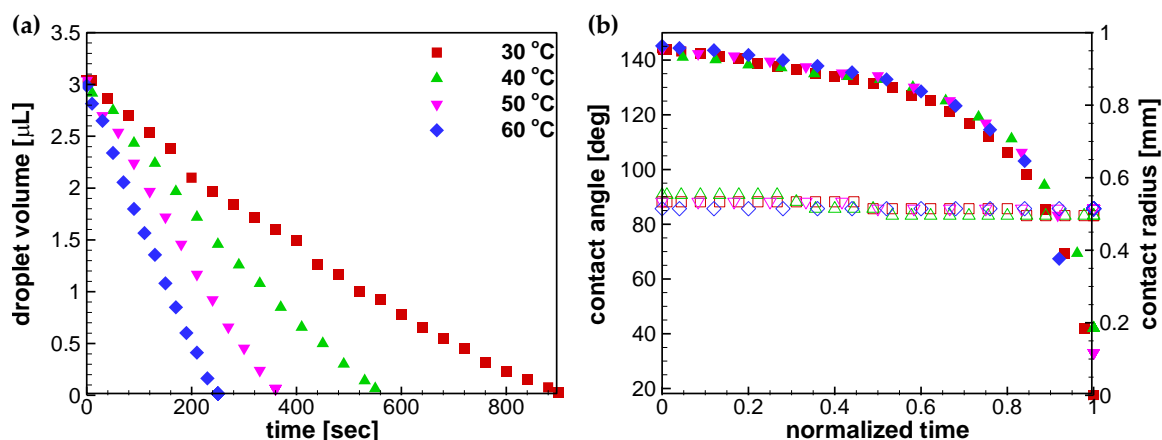


Figure 4.3. (a) The volume, and (b) contact angle (solid symbols) and contact radius (hollow symbols) of the droplet are shown as a function of time for selected droplet evaporation trials at each substrate temperature. The time axis in (b) is normalized by the total evaporation time in each case.

#### 4.2.2 Reflection Correction

The uncorrected interface temperatures shown in Figure 4.2 include the effects of background radiation. To proceed with further quantitative analysis, the raw interface temperature data acquired with infrared thermography must be corrected to account for the reflection of background radiation off the droplet to the camera sensor. Assuming that the incident radiation on the droplet interface is unpolarized, the specular reflectivity can be calculated using the Fresnel equations [102]. Due to the spherical shape of the droplet, the reflectivity of the droplet changes as a function of the angle between the surface normal of the droplet and the image plane. Hence, the droplet shape parameters are used to locally correct for the reflection for the entire droplet surface. Details of the reflection-correction procedure are presented in APPENDIX B.2.

All the infrared temperature data are corrected using this procedure; an example interface temperature contour of a droplet on a 50 °C substrate is shown in Figure 4.4. A complete set of corrected infrared temperature data for each substrate temperature and a range of droplet volumes are included in APPENDIX B.3. As can be seen in Figure 4.4, evaporative cooling has a significant effect on the droplet temperature distribution, resulting in a large temperature gradient along the height of the droplet. The resistance to thermal transport from the substrate to the top of the droplet leads to a significant temperature drop at the top of the droplet due to evaporative cooling. We note that the maximum interface temperature measured near the bottom of the droplet

( $\sim 39^\circ\text{C}$ ) is lower than the nominal bulk substrate temperature ( $50^\circ\text{C}$ ) due to localized evaporative cooling of the substrate directly beneath the droplet. A similar localized cooling effect was reported by Gleason et al. [103] based on infrared measurements of the substrate temperature in the presence of an evaporating droplet. The net evaporation rate from the droplet is determined by this non-uniform droplet interface temperature distribution; this effect is ignored in simplified vapor-diffusion-based models [44] that assume a uniform temperature for the entire interface. As a measure of the evaporative cooling effect, the temperature drop across the height of the droplet is plotted as function of the droplet volume in Figure 4.5. The temperature drop decreases as the droplet volume decreases with progressive evaporation. The reduction in the droplet height and contact angle with evaporation reduces the thermal transport resistance from the substrate to the interface, thus homogenizing the droplet temperature. This is consistent with high-fidelity modeling efforts that have shown a decreasing influence of evaporative cooling with decreasing droplet height-to-contact-diameter aspect ratio [50].

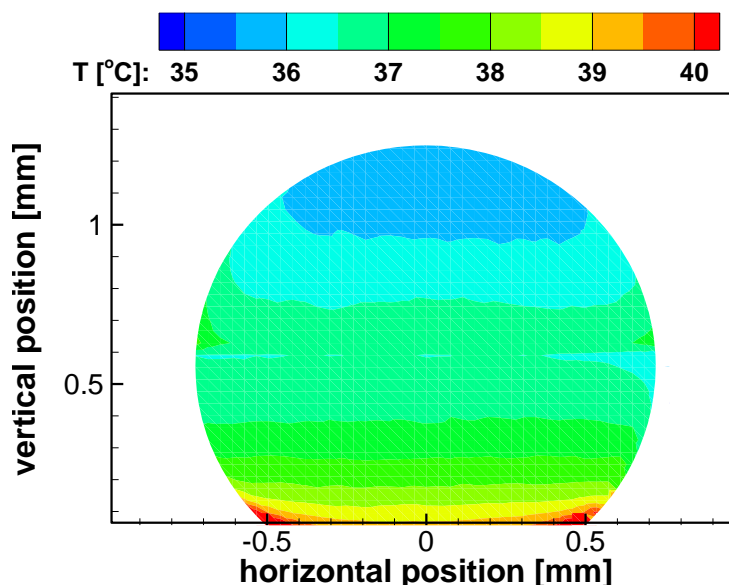


Figure 4.4. Temperature data after correcting for background reflections for a  $2\ \mu\text{L}$  droplet evaporating on a substrate at a temperature of  $50^\circ\text{C}$ .

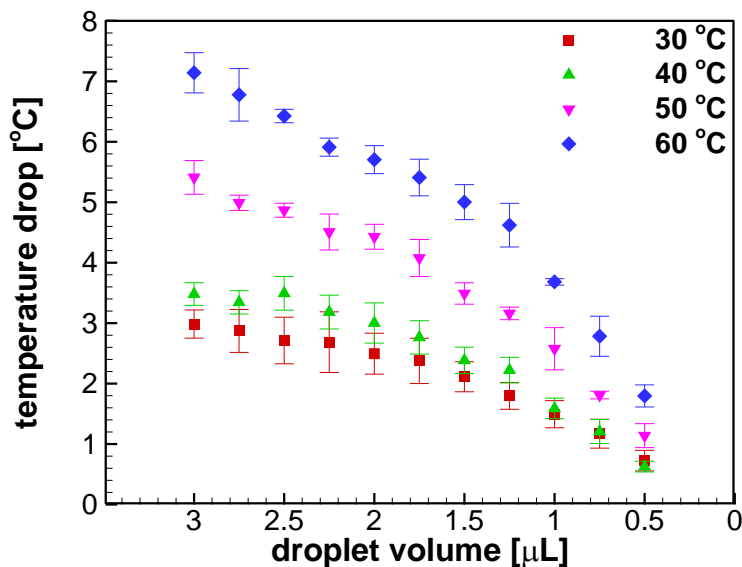


Figure 4.5. The temperature drop across the height of the droplet is plotted as function of droplet volume (at intervals of 0.25  $\mu\text{L}$ ) for all substrate temperatures. The error bars represent the standard deviations across all trials at that substrate temperature.

### 4.2.3 Evaporation Rate

The experimental evaporation rate shown in Figure 4.6 is calculated based on the derivative of droplet volume with time from the data shown in Figure 4.3. The evaporation rate decreases with decreasing volume during the course of evaporation. Even though the evaporation flux on the interface increases with decreasing volume (particularly drastically at the contact line) [49], the surface area of the droplet available for evaporation decreases sufficiently such that the net total rate reduces. Further analysis in APPENDIX B.4 incorporates the interface temperature data into vapor-diffusion-based and natural-convection-based predictions of the evaporation rate, to assess the relative importance of these transport mechanisms for the current data.

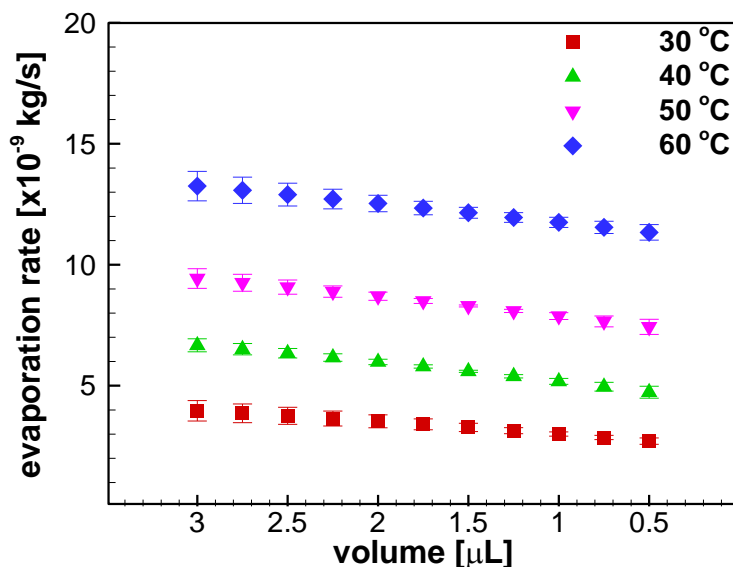


Figure 4.6. The experimental evaporation rate plotted as a function of droplet volume (at intervals of  $0.5 \mu\text{L}$ ) for all for all substrate temperatures. The error bars represent the standard deviation across all trials at a given substrate temperature.

### 4.3 Conclusion

Infrared thermography is exploited to capture the spatiotemporal interface temperature distribution during evaporation of a droplet on a nonwetting substrate; the volume and shape evolution of the droplet are tracked simultaneously with the interface temperature. This approach meets the need for accurate, localized temperature data to characterize salient features of droplet evaporation, as called for in past studies [51,71]. In addition, such data are critical to applications in which the droplet temperatures control physical processes other than evaporation, such as voltage-induced modulation of droplet temperatures for biosensing [104], control of reaction rates in droplet microfluidics [105,106], and temperature modulation to denature DNA for polymerase chain reactions [107,108]. The methodology is also broadly applicable for characterizing the temperature of curved interfaces.

## CHAPTER 5. MARANGONI CONVECTION IN EVAPORATING ORGANIC LIQUID DROPLETS ON A NONWETTING SUBSTRATE

The chapter quantifies the flow behavior inside sessile methanol droplets evaporating on a nonwetting substrate using particle image velocimetry (PIV). By means of an analysis of the flow direction and velocities, the relative significance of various thermal and flow transport mechanisms under these conditions is revealed. A reduced-order model is developed to predict thermal transport inside the organic liquid droplet during evaporation on a nonwetting substrate. The results show that the flow in these droplets are driven by surface tension gradients along the liquid-air interface of the droplet. The material presented in this chapter was published in *Langmuir* [28]. The experiments in Chapter 5.1 were done in collaboration with Dr. Susmita Dash and the substrates used in these experiments were fabricated by Dr. Xuemei Chen.

### 5.1 Materials and Methods

The reentrant mushroom-structured surface used in this study was fabricated on a copper substrate in the Birck Nanotechnology Center at Purdue University. The fabrication procedures include photolithography and electroplating. Briefly, photolithography was used to form a photoresist mold with a square array of circular pores, and over-mold electroplating was used to deposit copper and form hemispherical mounds atop the mold layer at each exposed pore location. This electroplating setup and copper deposition parameters were described previously in Ref. [109]. After electroplating, the copper substrate was soaked in acetone for 2 min to dissolve the photoresist mold, leaving behind mushroom-shaped copper structures. To render the as-fabricated surface repellent to liquids of low surface tension, the sample was silanized through immersion in a hexane solution of 0.5 wt% 1H,1H,2H,2H-perfluorodecyltrichlorosilane for 1 hr, followed by heat treatment at  $\sim 150$  °C on a hotplate for 1 hr. After surface treatment, the static methanol and water contact angles on this substrate were  $124 \pm 4$  deg and  $133 \pm 6$  deg, respectively. Figure 5.1(a) shows a scanning electron microscope (SEM) image of the mushroom-structured copper surface. The mushroom cap diameter and height are  $\sim 40$   $\mu\text{m}$  and  $\sim 15$   $\mu\text{m}$ , respectively; the mushroom stem diameter and height are  $\sim 20$   $\mu\text{m}$  and  $\sim 35$   $\mu\text{m}$ , respectively; and the mushroom center-to-center spacing is  $\sim 50$   $\mu\text{m}$ .

In the droplet evaporation experiments, methanol droplets with volumes from 1.3  $\mu\text{L}$  to 2.75  $\mu\text{L}$  (three or four test cases per substrate temperature) were placed on the substrate. The Bond number, which is the ratio of the gravitational body force to surface tension, is defined as  $\text{Bo} = \Delta\rho g L^2 / \sigma$ , where  $\Delta\rho$  is the density difference between liquid and vapor,  $g$  is the gravitational constant,  $L$  is the characteristic length (droplet height), and  $\sigma$  is the surface tension. For all of the experimental cases, the Bond number was found to be significantly lower than 1, indicating that the droplet interface shape is governed by surface tension. The testing apparatus is shown in Figure 5.1(b). A transparent, acrylic enclosure was placed around the droplet to prevent ambient air currents from affecting the evaporation process and internal flow field. The substrate was held at a fixed temperature using a Peltier stage with temperature feedback (CP-031, TE Technology, Inc.). The experiments were conducted at ambient conditions and with the substrate fixed at three different sub-ambient temperatures:  $15 \pm 0.1$   $^\circ\text{C}$ ,  $10 \pm 0.1$   $^\circ\text{C}$ , and  $5 \pm 1$   $^\circ\text{C}$ . Testing at sub-ambient temperatures limits the evaporation rate and enables capture of time-averaged velocity data without a significant change in the droplet volume during the measurement period. The ambient temperature and humidity were  $23 \pm 1$   $^\circ\text{C}$  and  $20 \pm 3\%$ , respectively.

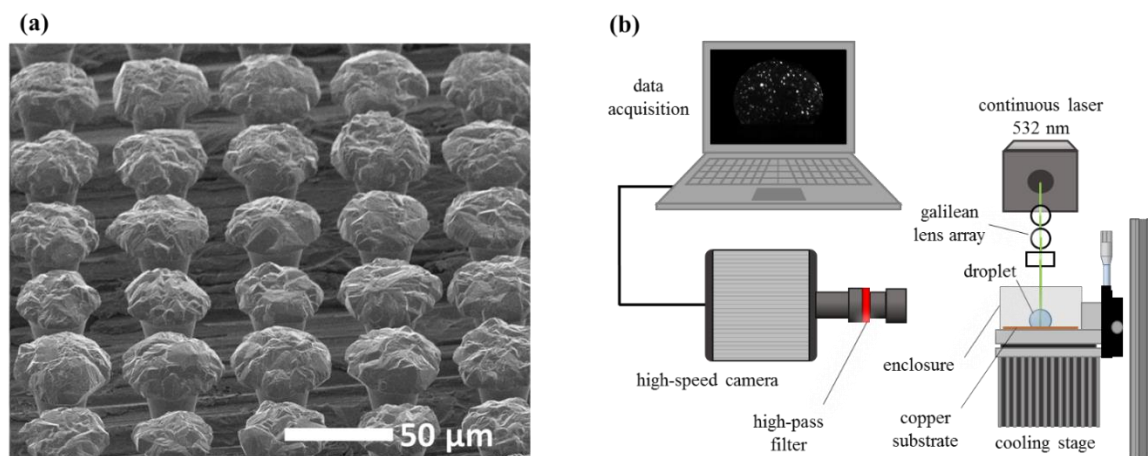


Figure 5.1. (a) A scanning electron microscopy (SEM) image of the substrate, and (b) a schematic diagram of the experimental setup.

For visualization of the flow field inside the droplet, the liquid was seeded with fluorescent polystyrene microspheres (1  $\mu\text{m}$  diameter), which have peak excitation and emission wavelengths of 532 nm and 602 nm, respectively. The PIV setup utilized a continuous diode-pumped solid-

state Nd:YAG laser (Coherent Verdi V5; 532 nm) and a Galilean lens arrangement. The light sheet produced by this arrangement was  $\sim 30 \mu\text{m}$  thick and illuminated the center vertical plane of the droplet. The laser provided sufficient illumination at 0.75 W for these experiments; fluid heating due to laser illumination can be ignored at this power level due to the low absorption coefficient of methanol at 532 nm ( $5.9 \pm 0.5 \times 10^{-4} \text{ cm}^{-1}$  [110]). A high-speed camera (Photron FASTCAM-1024PCI) observed the illuminated plane of the droplet using a lens (Cosmicar TV Lens, 50 mm, 1:1.8), extension tubes (13.5 cm), and a long-pass filter (620 nm center wavelength; 52 nm bandwidth). The images were captured at 1000 frames/sec with a spatial resolution of  $\sim 4.4 \mu\text{m}/\text{pixel}$ . The imaging components are shown in Figure 5.1(b). For each experiment, after the droplet had been allowed to sit on the substrate for approximately 1 min in order to ensure the establishment of a steady internal flow pattern, images were captured for a duration of 1.0 to 1.5 sec. The change in volume within this period of imaging was negligible; the flow field acquired is representative of a quasi-static snapshot at a given droplet volume. The flow field visualizations do not yield an estimate of the evaporation rate based on a change in the droplet volume. The velocity vector fields were calculated by analyzing consecutive images using a multipass, cross-correlation algorithm with a discrete window offset. Successive window sizes of  $64 \times 64$  and  $32 \times 32$  pixels, with a 50% overlap between consecutive frames, were used. The instantaneous velocities were then averaged over the span of the data collection to create an ensemble vector field. Assuming that the droplet has a spherical-cap shape, a ray-tracing method was used to correct the distortion caused by the curved interface of the droplet and obtain an accurate measurement of the flow field [5].

Separate from the flow field visualizations, the same experimental setup was used to directly measure the temperature difference between the top and bottom of the droplet. A  $75 \mu\text{m}$ -diameter thermocouple was positioned vertically along the center axis of the droplet using a micrometer stage. The droplet temperatures were measured very close to the substrate and to the liquid-vapor interface at the top; measurement locations were  $0.21 \pm 0.04 \text{ mm}$  from the substrate ( $T_{bot}$ ) and  $0.11 \pm 0.04 \text{ mm}$  from the top of the droplet ( $T_{top}$ ).

## 5.2 Results and Discussion

### 5.2.1 Velocity Profiles and Temperature Measurements

Figure 5.2(a) shows the velocity field in the vertical center plane for a sample droplet; Figure 5.2(b) shows the vertical velocity component along a vertical centerline in this plane. An axisymmetric toroidal vortex structure is observed, with flow downward at the centerline toward the substrate, then outward toward the contact line, and upward along the peripheral liquid-air interface. This recirculating flow pattern is also clearly apparent in the photographic streaklines shown in Figure 5.2(c).

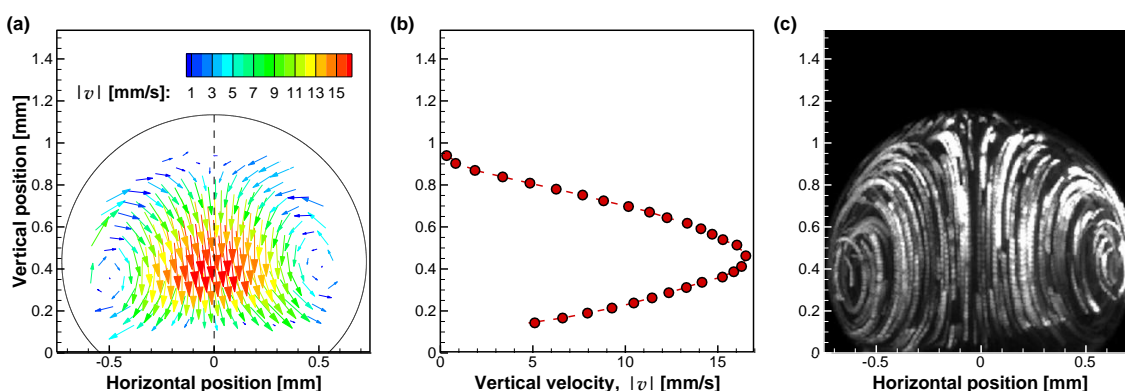


Figure 5.2. (a) Velocity vector field (from PIV analysis with ray-tracing corrections) within a  $1.34 \mu\text{L}$  droplet on a substrate fixed at  $10^\circ\text{C}$ , and (b) the centerline vertical velocity taken along the  $y$ -axis at  $x = 0$ . (c) A streakline image is obtained from superimposing images of the tracer particles.

The flow direction of a recirculating Marangoni convection pattern is determined by the substrate-to-droplet thermal conductivity ratio ( $k_R$ ) and the contact angle (CA) [54,57,111]. For the present cases, where  $k_R > 2000$  and  $\text{CA} \approx 124^\circ$ , the experimentally visualized flow direction matches the direction that would be expected for Marangoni convection. An evaporation-induced temperature gradient along the height of the droplet (with a decreasing temperature from the contact line to droplet apex) would lead to the surface-tension-induced Marangoni convection pattern observed here.

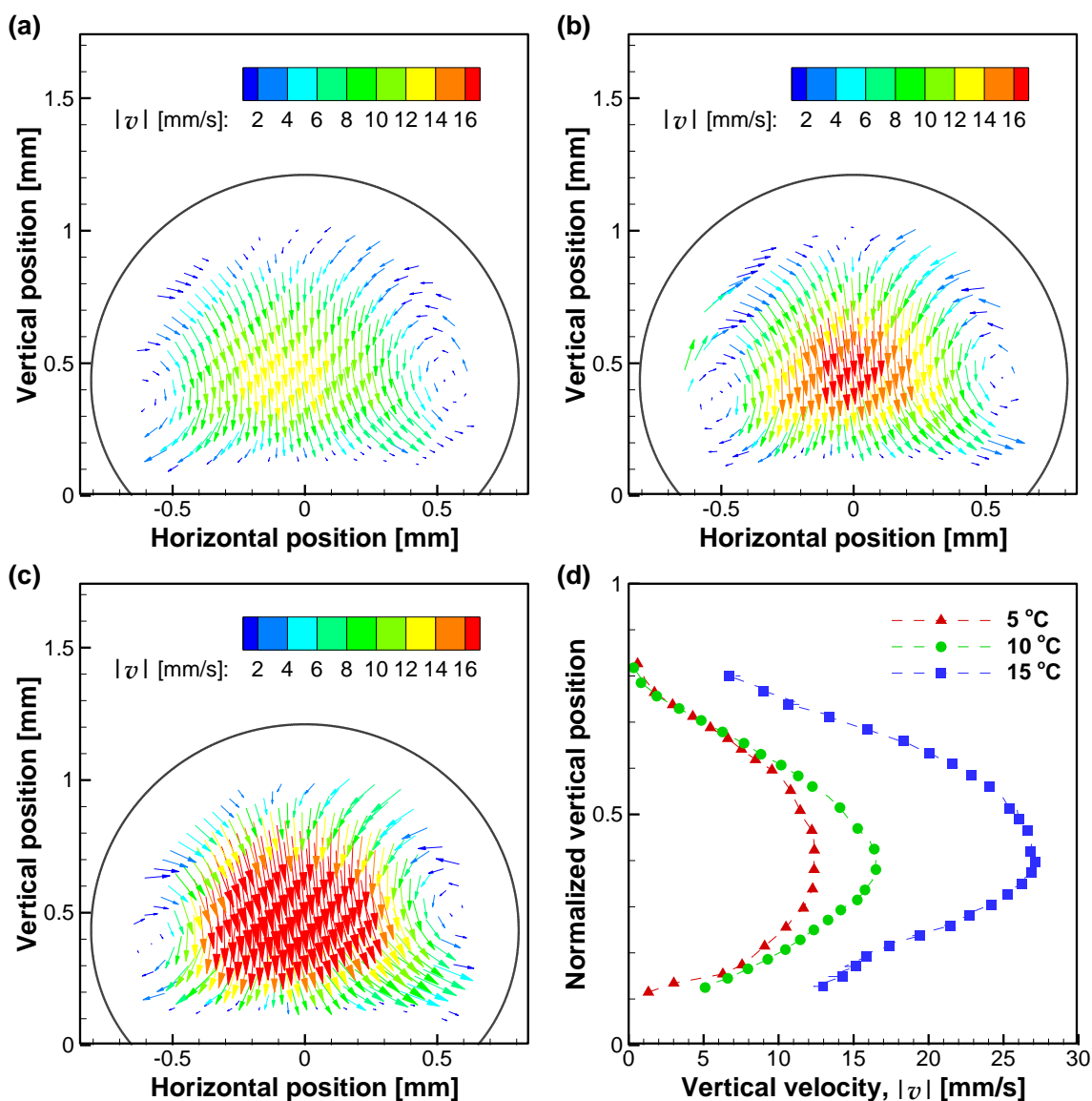


Figure 5.3. The velocity vector fields for 1.7  $\mu\text{L}$  methanol droplets at substrate temperatures of: (a) 5 °C, (b) 10 °C, and (c) 15 °C. (d) Centerline velocity profiles for each of the substrate temperatures.

Figure 5.3 shows that the velocity fields in the droplets are strongly influenced by the substrate temperature: the velocities increase with an increase in substrate temperature. This increase is most apparent at the center of the droplet, where the velocity is a maximum as a result of the funneling into the center of the toroidal flow. The maximum velocities measured in the present study for methanol droplets on nonwetting surfaces are on the order of 10 to 45 mm/s, depending on the substrate temperature. It is also observed from the experiments that there is no discernable

correlation between droplet volume and velocity profile (in both magnitude and shape), as shown in Figure C.1 in APPENDIX C.1, for the range of droplet volumes investigated.

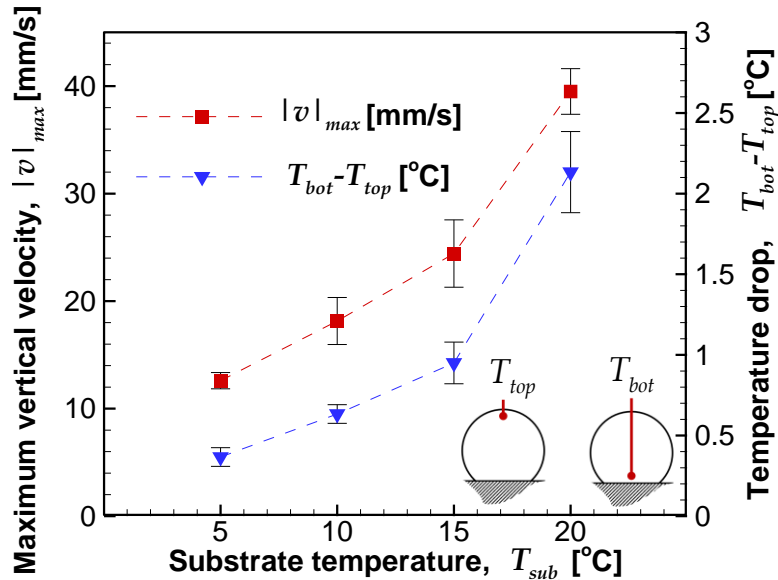


Figure 5.4. Temperature drop from the bottom to the top of the droplet, and maximum velocity magnitude versus substrate temperature. The uncertainty bars indicate the standard deviation for all the tests at each substrate temperature.

Figure 5.4 shows the measured temperature difference between the bottom and top of the droplet for each substrate temperature. The initial volume of the droplet during these temperature measurements ranged from 1.9  $\mu\text{L}$  to 3.2  $\mu\text{L}$ , with four tests performed at each temperature. There is a temperature drop between the bottom and the top of the droplet due to evaporative cooling [45,112]. The temperature difference across the droplet height decreases as the substrate temperature decreases due to a reduction in the rate of evaporation. Figure 5.4 also shows the magnitude of the maximum velocity at each substrate temperature. The trend in maximum velocity tracks the temperature difference across the droplet height, indicating a temperature-gradient-driven flow field.

## 5.2.2 Velocity Scaling Analysis

Buoyancy and surface tension forces may both induce temperature-gradient-driven flows. Marangoni convection inside an evaporating droplet [32] is driven by a surface tension gradient along the droplet interface (induced by a temperature gradient along the interface). Buoyant

convection is driven by a density difference along the height of the droplet (induced by a temperature gradient along the height). A simple scaling analysis shows that surface tension has a stronger influence on the flow patterns than buoyancy. The ratio of surface tension to viscous forces is given by the Marangoni number  $Ma = -(d\sigma / dT)L\Delta T / (\mu\alpha)$ , where  $\sigma$  is the surface tension of the fluid,  $L$  is the characteristic length scale or droplet height,  $\Delta T$  is the temperature difference across the droplet height,  $\mu$  is the dynamic viscosity of the liquid, and  $\alpha$  is the thermal diffusivity of the liquid. In Figure C.2, we show a direct correlation between the maximum velocity and the Marangoni number for each experimental case, indicating that the flow may be surface tension-driven. The ratio of buoyancy and viscous forces is given by the Rayleigh number  $Ra = g\beta\Delta TL^3 / (\nu\alpha)$ , where  $\nu$  is the kinematic viscosity of the fluid and  $\beta$  is the thermal expansion coefficient. Nominal values for the properties at 300 K are shown in Table 5.1, but temperature-dependent properties are used in the calculation. Thus, a ratio of the Marangoni and Rayleigh numbers may be used to assess the relative strength of the surface tension and buoyancy forces. On average over the test cases, this ratio is calculated to be 4.6, indicating that surface tension forces dominate over buoyancy in the present experiments. This confirms that, while buoyancy may play a counteracting role, the flow direction is driven by Marangoni convection. It is noted that for droplet evaporation on a nonwetting surface, capillary-driven flow can be neglected due to a lack of liquid confinement effects, as well as suppression of evaporation, at the contact line [49].

Table 5.1. Liquid Properties at 300 K [113]

$\rho$	$k_l$	$c_p$	$h_{fg}$	$\mu$	$d\sigma/dT$	$p_{sat}$	$D_{AB}$	$\beta$
$[kg/m^3]$	$[W/m \cdot K]$	$[J/kg \cdot K]$	$[kJ/kg]$	$[mPa \cdot s]$	$[mN/K]$	$[kPa]$	$[cm^2/s]$	$[1/K]$
784.5	0.204	3663.8	1166.2	0.543	-0.0812	18.61	0.140	0.00149

An additional scaling analysis is conducted using the representative Marangoni velocity, which is defined as  $v_{Ma} = -(d\sigma / dT)(\Delta T / \mu)$ ; this scaling represents the velocity at the interface for this surface phenomenon. However, the experimental results do not provide velocity data very close to the interface due to the inherent masking of visual data in this region from the camera sensor caused by the spherical droplet shape and difference between the refractive indices of methanol

and air [5,114]. Thus, it becomes necessary to estimate the velocity at the interface from the available experimental data. We assume a flow field profile such that the available velocity data can be projected to the interface, as described in detail in APPENDIX C.3, in the section on estimation of the droplet interface velocity. This interface velocity is plotted against the Marangoni velocity scale in Figure 5.5. The linear correlation between the two velocities is strong, and the absolute velocities are on the same order of magnitude. The deviation of the slope of the dependence from unity is likely due to the approximations involved in the determination of the interface velocity from the available experimental data as well as the counteracting effect of buoyancy. We note that these velocities are significantly higher than the velocities seen in the core of the droplet as a result of a restricted flow area in the periphery, as well as the flow field profile assumed.

We note that the interface velocities reported here ( $\sim 100$  mm/s) are much higher than those reported in literature [54]. Based on the understanding of the transport in evaporating droplets in the literature [5], the large height-to-width aspect ratio of a droplet sitting on a nonwetting substrate allows a larger temperature gradient to be established across the droplet height compared to low-contact-angle droplets on wetting substrates. This larger temperature gradient would increase temperature-driven Marangoni convection velocities.

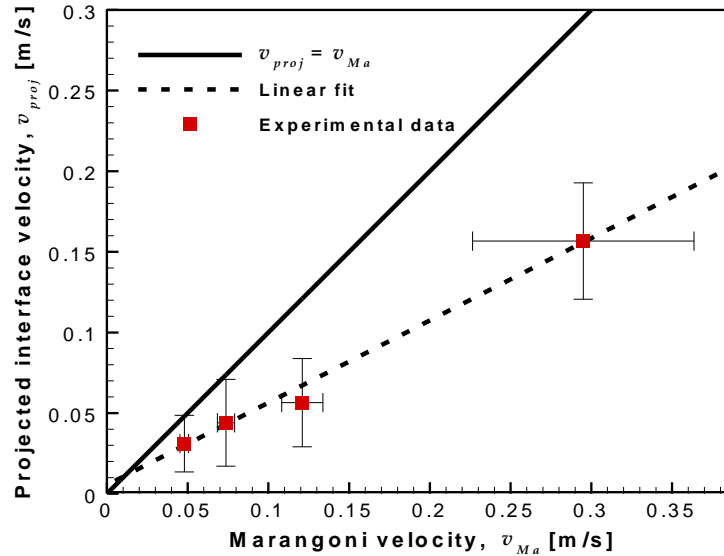


Figure 5.5. Projected interface velocity as a function of Marangoni velocity. The error bars show the standard deviation of the four data points at each substrate temperature for both the projected velocities and the Marangoni velocity.

### 5.2.3 Reduced-Order Evaporation Model Incorporating Advective Transport in the Droplet

The maximum velocities reached for buoyancy-induced flow fields observed inside water droplets evaporating on superhydrophobic surfaces are on the order of only 0.15 mm/s, even for heated substrates [5]. This is in stark contrast with the much higher velocities obtained in the present work for methanol droplets on nonwetting substrates. The relative importance of advective heat transfer can be characterized by the Péclet number, which is the ratio of the rate of advection to thermal diffusion and is defined as  $Pe = UL/\alpha$ , where  $U$  is taken as the mean velocity and  $L$  is the characteristic length scale (droplet height). For substrate temperatures between 5 °C and 15 °C in the current experiments, the calculated Péclet number ranged from 150 to 500, indicating that advection may play an important role during the evaporation of organic liquid droplets on nonwetting surfaces. The temperature drop along the height of the droplets predicted using evaporation models with and without advection must be compared against the experimentally reported temperature drops to further investigate the influence of advective transport.

Simplified vapor-diffusion models characterize the evaporation process by considering species diffusion from the droplet interface (at the saturated vapor pressure) to the ambient [44].

Augmented vapor-diffusion evaporation models account for temperature variation along the height of the droplet by only considering conduction [64,65]; these models overpredict the temperature drop within the droplet for the current experiments, as shown in Figure 5.6. A droplet evaporation model is developed that incorporates advective transport to reconcile the discrepancy between the diffusion-only predictions and the experimental values. The model predicts the recirculating mass flow rate using the representative Marangoni velocity formula, and assumes a simplified convection cell for which coupled advection and diffusion transport is calculated. A detailed description of the modeling approach and implementation is provided in APPENDIX C.4. Briefly, advective transport is considered by identifying two regions – a central core where the flow is downward and an outer peripheral region where the flow is upward (Figure 5.6). These regions are coupled at the top and bottom of the droplet by diffusion-dominated regions. The model also incorporates convective heat transfer between the droplet and the ambient air. To obtain a temperature drop across the droplet height, the substrate temperature is fixed and evaporative cooling at the interface is predicted for vapor-species diffusion to the ambient [44,71]. The model uses a guessed temperature gradient to calculate the Marangoni velocity. This Marangoni velocity is used to calculate the mass flowrate in the system, which is then used in the advective term for the thermal transport to calculate the temperature gradient. This loop is iterated upon until the temperature gradient converges. As can be seen in Figure 5.6, this simplified thermal advection model adequately predicts the measured temperature difference across the droplet. For the diffusion model, the mean relative percent error in temperature drop was found to be 1350%, while the advection model yielded a much lower 41.5% relative percent error. We conclude that accounting for advective transport is crucial for predicting the temperature drop inside an evaporating organic liquid droplet on a nonwetting surface, unlike on wetting substrates where this advective contribution is negligible [64,65]. Furthermore, the simplified modeling approach offered here is representative of the effective advective transport of the toroidal vortex induced by Marangoni convection.

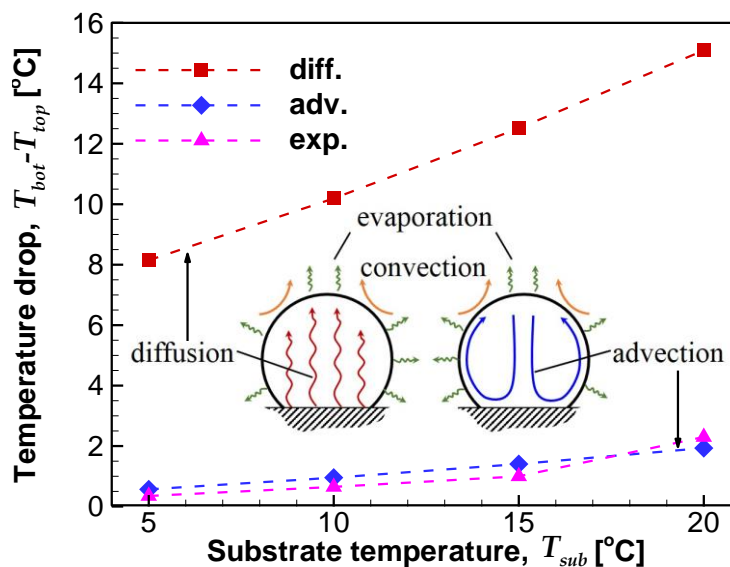


Figure 5.6. Comparison between the experimental values of the average temperature drop inside the droplet, the predictions from the thermal diffusion and the thermal advection models. The inset shows the transport mechanisms included in the two models.

### 5.3 Conclusion

A quantitative study was performed of velocity profiles inside methanol droplets evaporating on a nonwetting substrate. The experimentally observed flow direction, as well as the clear correlation between the maximum velocity and temperature gradient in the droplet, indicated that the flow field was driven by surface tension forces. This was confirmed through a scaling analysis; the interface velocity was found to be proportional to the Marangoni velocity. Due to the large velocities present in the droplet, a semi-empirical, reduced-order droplet evaporation model was formulated that incorporates advective transport in order to accurately predict thermal transport in the droplet. Unlike previous reduced-order models that only consider conduction in the droplet, our model showed a strong agreement with the experimentally measured temperature drops for an organic liquid droplet evaporating on a nonwetting substrate.

## **CHAPTER 6. EVAPORATION-DRIVEN MICROMIXING IN SESSILE DROPLETS FOR MINIATURIZED ABSORBANCE-BASED COLORIMETRY**

This chapter explores a sessile droplet-based, absorbance measurement system for colorimetric quantitation of protein concentration. The complex interactions between mixing, reaction, and protein adsorption are investigated and characterized. With the concepts presented here, we propose a technique that uses a sessile droplet-based device as an alternative for microtiter plates for absorbance-based colorimetry. The material presented in this chapter is in preparation for publication.

### **6.1 Materials and Methods**

We propose a technique that would use a droplet microarray as an alternative for microtiter plates for absorbance-based colorimetry. The concept involves making real-time absorbance measurements through droplets on a nonwetting substrate, where the droplets are formed by placing reagent dye upon a sample solution, and comparing the response to that of known concentrations. The nonwetting substrate exploits the buoyancy-driven convection to ensure rapid mixing and complete reaction of the reagent into the sample, while also ensuring that evaporation of the droplet is suppressed. The absorbance is measured by illuminating the droplet at the wavelength of interest from one side and measuring the incoming light on the other. The current study demonstrates this sessile-droplet-based absorbance measurement for colorimetric analysis of protein concentration. The proof-of-concept implementation approach is described and real-time absorbance measurement signals are analyzed for pre-mixed droplets and *in situ* droplet mixing.

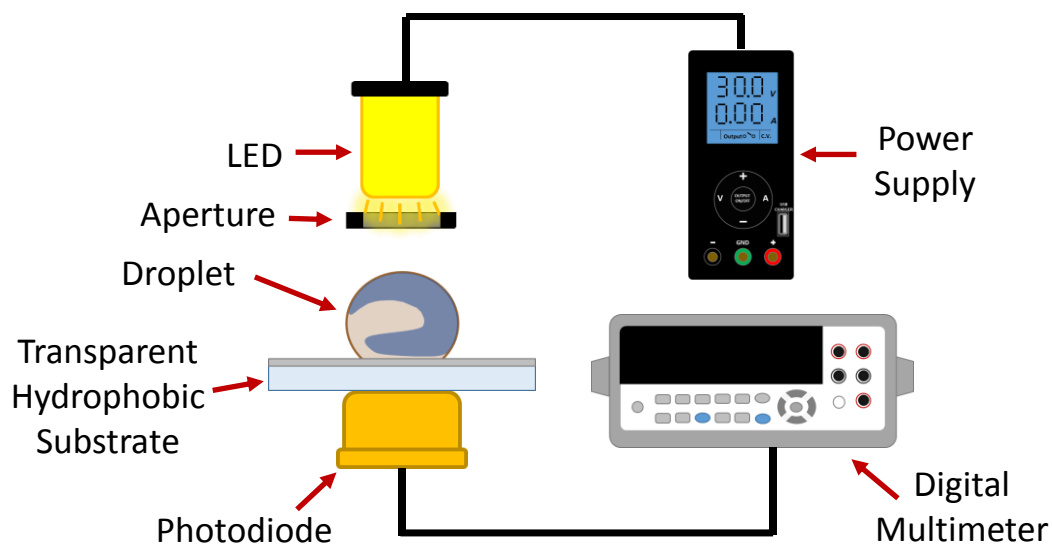


Figure 6.1. Schematic diagram of the experimental facility used for the absorbance measurement.

Figure 6.1 shows a schematic diagram of the experimental setup used for the absorbance measurements. The setup measures the light at a specific wavelength through a sessile droplet placed on a transparent, nonwetting substrate. To this effect, an InGaAlP light-emitting diode (LED) with a peak wavelength of  $590 \pm 10$  nm (LED591E, Thorlabs) is aligned with a photodiode with a wavelength range of 320-1100 nm (FD11A, Thorlabs) through a 0.84 mm-diameter aperture that confines the area of the illumination to within the droplet's base footprint radius. The LED is connected to a DC power supply (1550, BK Precision). The photodiode is connected to a digital multimeter (34410A, Keysight) that records the signal at 10 Hz using a LabVIEW code. The nonwetting substrate is fabricated using a glass slide of 1 mm thickness (3057, Gold Seal®). The slide is cut into a 25 mm×25 mm square substrate and cleaned with acetone, methanol, and deionized (DI) water, respectively. Teflon granules (Teflon® AF2400, Dupont) are dissolved into FC-72 (Fluorinert Electronic Liquid FC-72, 3M) to create a 1% weight/volume solution. This solution is then spin coated onto the clean glass at 1500 RPM. The coated slides are then baked on a hot plate at 150 °C for 2 hr. The resulting low-surface-energy surface has contact angle of 125 deg for the sample–reagent mixture used in the experiments. The droplet exhibits a constant contact radius mode of evaporation due to contact line pinning on the substrate.

The droplet is composed of two solutions: the sample and the reagent. The sample is prepared by dissolving Bovine Serum Albumin (98% lyophilized powder, Sigma-Aldrich) into DI water to achieve the desired concentration of protein; the sample concentration is henceforth defined by the amount of protein in DI water. The reagent is the Bradford reagent mixture (Sigma-Aldrich), which contains Coomassie<sup>TM</sup> Brilliant Blue G-250 dye in phosphoric acid and methanol. The reagent is initially of a reddish-brown color. The reaction between the protein (in the sample) and dye (in the reagent) results in the liquid changing to a blue color, with the degree of change corresponding to the concentration of protein in the sample. The change in absorbance of the liquid is most sensitive at a wavelength near 590 nm.

Experiments are conducted in two different configurations: (1) a pre-mixed case to confirm that the absorbance signals measured through the droplet medium have a detectable change over the target range of sample concentrations, and (2) an *in situ* mixing case to demonstrate the proposed concept of using the droplet as a self-contained passive mixing apparatus to make colorimetric measurements. For the pre-mixed case, the sample and reagent are thoroughly mixed in 1-to-5 ratio of sample to reagent in a test tube. After the sample is thoroughly mixed and the reaction is complete, a 10  $\mu\text{L}$  droplet of this mixture is deposited on the substrate, quickly aligned between the LED and photodiode, and the signal is recorded in volts. This approach effectively measures the signal of the completely reacted mixture, without introducing the complexities of real-time mixing and reaction within the droplet. For the *in situ* mixing case, a 1.7  $\mu\text{L}$  droplet of sample is first placed on the nonwetting substrate. An 8.3  $\mu\text{L}$  reagent is then added to the sample droplet, thereby creating an approximately 1-to-5 sample-to-reagent ratio. The droplet is then aligned with the photodiode and the signal measured in real time for 1000 s. The experiments for both configurations are conducted at three sample concentrations: 0.1 mg/mL (1.51  $\mu\text{M}$ ), 0.15 mg/mL (2.26  $\mu\text{M}$ ), and 0.3 mg/mL (4.51  $\mu\text{M}$ ). Three tests are conducted at each test case to demonstrate repeatability.

In order to calculate an absorbance metric from the raw signal, a 'blank' sample is used for reference, as is the case in conventional colorimetry. A droplet with a sample of 0 mg/mL concentration of protein is used as the blank, which allows a reference signal to be measured that takes into account the curvature of the droplet and the resulting lensing effects. This is possible because the evaporation characteristics of the droplets with blank samples is nearly identical to

that of droplets with protein samples, as confirmed by the goniometric measurements shown in Figure E.1 in E.1; the volume and height evolution of the droplets with and without protein in the sample are identical. A key assumption in the absorbance metric is that the intensity of the light incident on the photodiode is linearly proportional to the voltage signal output read by the multimeter. Based on this assumption, a formulation analogous to Beer's Law is used to calculate the absorbance metric:

$$A = \log_{10} \left( \frac{V_o}{V} \right) \quad (\text{D.1})$$

where  $A$  is the absorbance metric,  $V_o$  is the voltage reading from the blank sample, and  $V$  is the voltage reading from the sample that is being measured. Signal measurement of the blank sample, measured separately, is relatively constant throughout evaporation at mean value of 0.1303 V. The overall lack of change in signal with evaporation indicates that the change in lensing with droplet volume is negligible with respect to measured absorbance signal. As the concentration increases, it is expected that the absorbance signal increases as well.

## 6.2 Results and Discussion

Figure 6.2. shows the absorbance metric measurements for premixed sample concentrations of 0.1 mg/mL (1.51  $\mu\text{M}$ ), 0.15 mg/mL (2.26  $\mu\text{M}$ ), and 0.3 mg/mL (4.51  $\mu\text{M}$ ). The raw voltage measurements that were used to calculate these values are provided for reference in Figure E.2, in APPENDIX E.2. As can be clearly seen in Figure 6.2, the absorbance generally increases with concentration. There is an initial valley in the absorbance signal that becomes more pronounced at higher concentrations. This valley is likely due to buoyant convection in the droplet initially mixing the components, diluting the protein temporarily faster than it can react. There is also a monotonic decrease in the absorbance with time towards the end of the experiment. This is due to adsorption of the protein onto the Teflon-coated substrate reducing the concentration in the droplet, and thus, reducing the absorbance. This trend is more apparent with increasing concentration due to the higher contrast in the signal between the blank and the test sample. Figure 6.3 shows the absorbance metric value at 400 s as a function of the sample concentration, with a linear fit and an 80% prediction interval, with a slope of 0.616  $\mu\text{M}^{-1}$ . There is a strong monotonic increase in

absorbance with increasing concentration. With this experimental confirmation of a measurable trend in the absorbance for a sessile droplet configuration, the proposed method of mixing *in situ* and removing the necessity of an external mixing apparatus is explored.

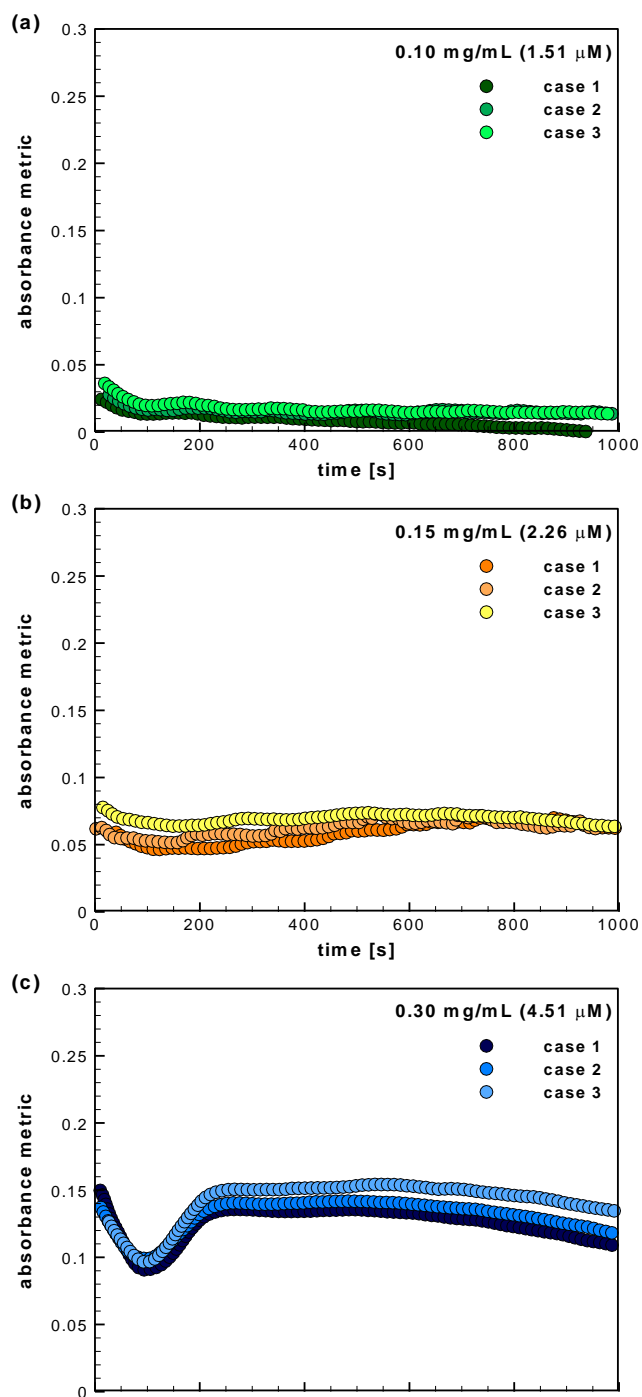


Figure 6.2. Time-resolved absorbance measurements for premixed sample droplets at concentrations of: (a) 1.51  $\mu$ M, (b) 2.26  $\mu$ M, and (c) 4.51  $\mu$ M.

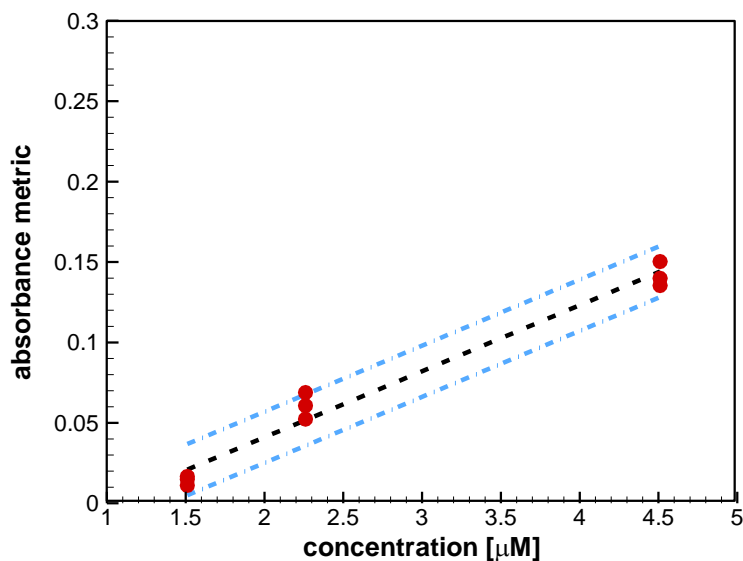


Figure 6.3. The sample absorbance metric values at 400 s (extracted from Figure 6.2) are plotted as a function of concentration, along with a linear fit (dashed line) and an 80% prediction interval (dash-dotted line).

The results for *in situ* mixing absorbance metric measurements for sample concentrations of 0.1 mg/mL (1.51  $\mu\text{M}$ ), 0.15 mg/mL (2.26  $\mu\text{M}$ ), and 0.3 mg/mL (4.51  $\mu\text{M}$ ) are shown in Figure 6.4(a), (b), and (c), respectively. Raw signal measurements for these test cases are shown in Figure E.3 in APPENDIX E.2. A complex temporal absorbance signal is recorded for all samples, consistently featuring a slight increase followed by a slight decrease and then a large increase (approximately within the first  $\sim 400$  s). Lastly, there is a monotonic decrease in the absorbance metric that continues to the end of the experiment. This signal evolution results in two initial absorbance metric peaks (local maxima) with a valley (local minimum) in between. Overall, the absorbance increases with increasing protein concentration, as in the pre-mixed cases; this concentration-dependence is especially prominent for the peak and valley values.

To understand the complexities of this evolution, videos were collected during the mixture and reaction process for the droplet with a sample of concentration 0.3 mg/mL (4.51  $\mu\text{M}$ ). At this concentration, color changes due to the reaction are clearly observable in the visible spectrum to a camera. The camera is placed horizontally facing the droplet and records through the same time period as the absorbance measurement. Images extracted from this video at 100 s increments are shown in **Error! Reference source not found.** The images illustrate the interplay of buoyancy-induced mixing, chemical reaction, and protein adsorption, which play a significant role in

affecting the signal measured through the droplet, as the droplet progresses through multiple stages of being darker blue (higher absorbance at the 590 nm wavelength) and lighter blue or brown (lower absorbance at the 590 nm wavelength).

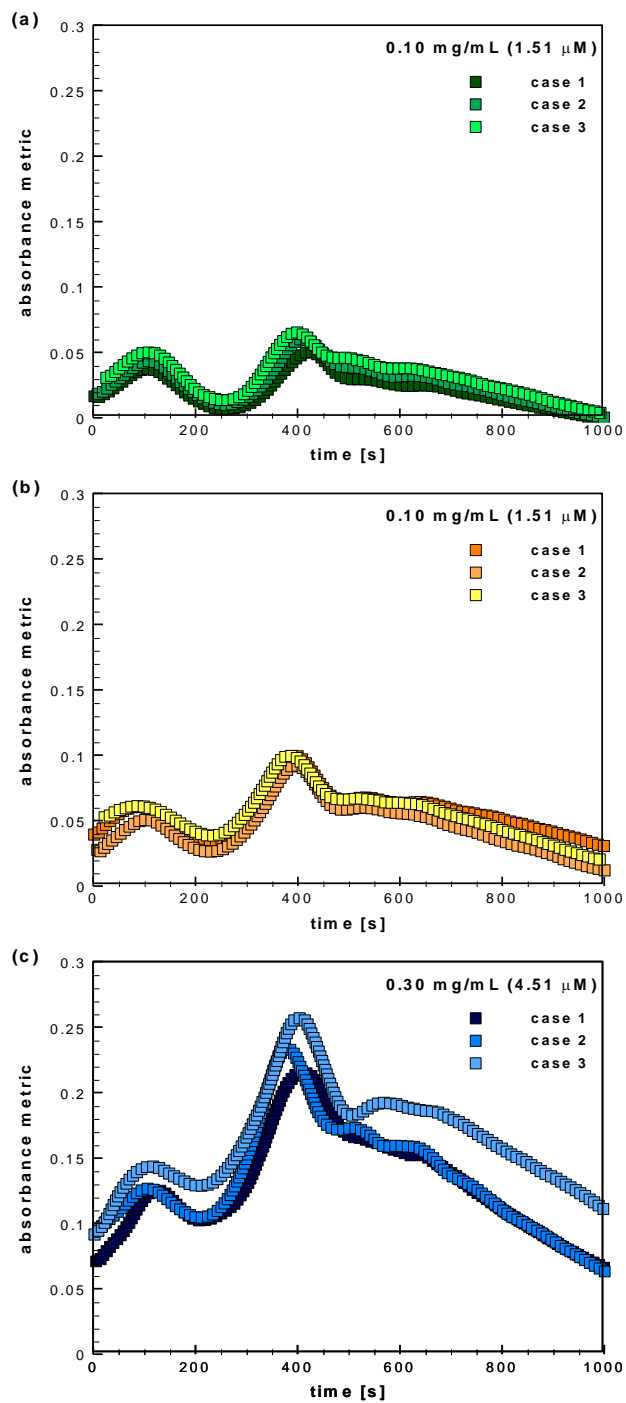


Figure 6.4. Time-resolved absorbance measurements for *in situ* mixed sample at concentrations of: (a) 1.51  $\mu$ M, (b) 2.26  $\mu$ M, and (c) 4.51  $\mu$ M.

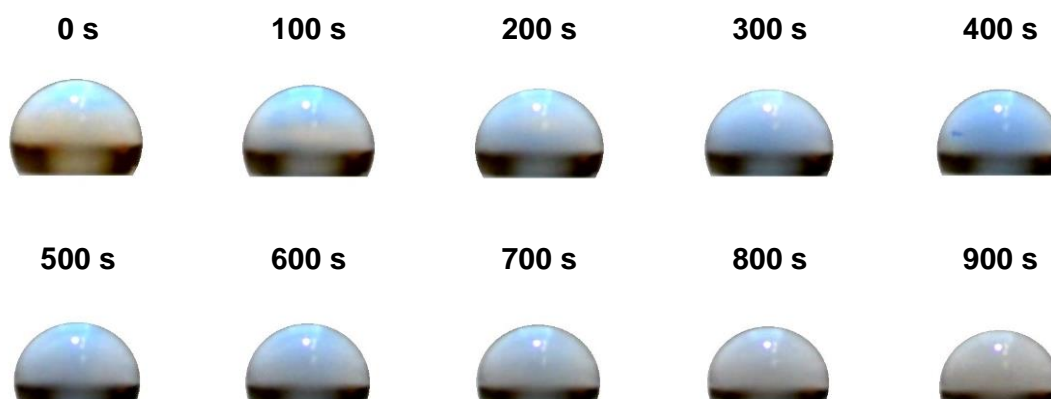


Figure 6.5. Cropped image frames, captured at 100 s increments from the droplet video for the *in situ* mixing case at a concentration of 0.3 mg/mL (4.51  $\mu$ M).

The color distribution observed in the video is analyzed to determine the dominant mechanisms that lead to the different phases of the droplet temporal absorbance signal. These phases are determined by temporally aligning the videos with the absorbance metric plot shown in Figure 6.4(c), particularly focusing on the peaks, valleys, and trends between. The phases and associated mechanisms are illustrated in the representative inset diagrams of Figure 6.6. (1) *Initially*, the protein sample amasses at the top of the droplet and the initial reaction creates a dark blue region directly within the path of the light source and the photodiode. Buoyant convection then distributes this mass through the droplet in the subsequent (2) *mixing phase*, causing more of the protein to react and resulting in the absorbance increasing slightly during. However, the mixing eventually dilutes the color faster than the reaction occurs in the (3) *dilution phase*, resulting in the droplet absorbance decreasing slightly. Once the sample is thoroughly mixed, the droplet enters a (4) *reaction phase* where the reaction dominates over dilution, thus darkening the droplet and increasing the absorbance dramatically. Once most of the protein has reacted into protein–dye complexes, the droplet enters the (5) *adsorption phase*, where the protein adsorbs onto the Teflon-coated substrate faster than any continuing reaction. This causes the droplet to revert to the reagent’s native reddish-brown color and the absorbance metric drops monotonically as the droplet tends towards the end of experiment. The time difference between the two peaks in the absorbance signal were analyzed and found to be virtually identical across all concentrations ( $293.28 \text{ s} \pm 12.88$ ) indicating that the mixing and reaction time scales do not change discernably with concentration.

This is expected due to fact that the substrate temperatures are the same in all trials, resulting in the same buoyancy-induced convection.

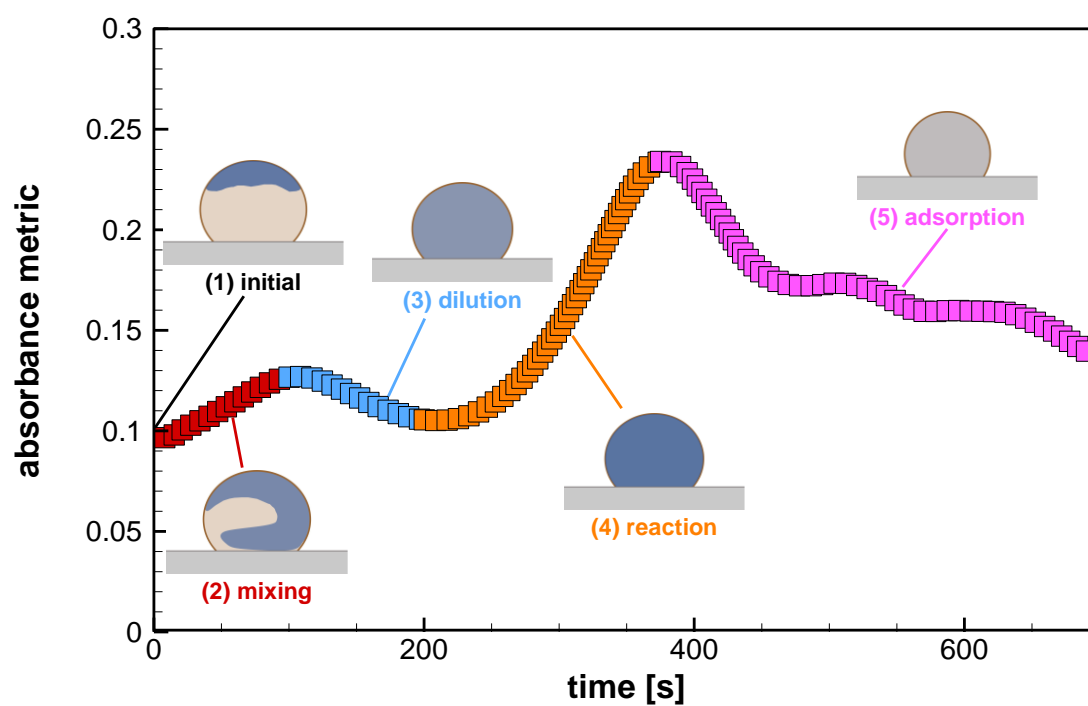


Figure 6.6. A plot of the temporal absorbance for a selected trial at a sample concentration of 0.3 mg/mL (4.51  $\mu$ M) with inset schematic drawings showing the various phases of *in situ* mixing of the reactant and sample, including: (1) the initial droplet, (2) the mixing phase, (3) the dilution phase, (4) the reaction phase, and (5) the adsorption phase.

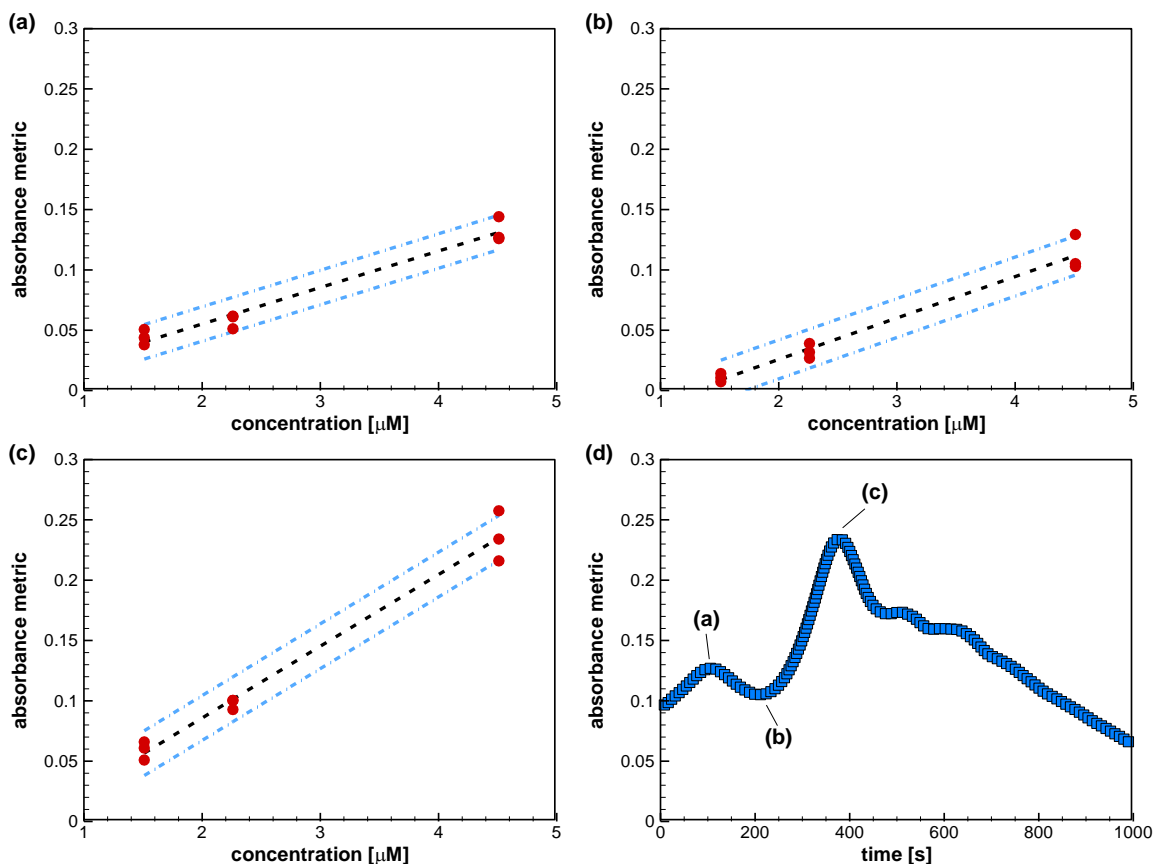


Figure 6.7. The absorbance metric at (a) the first peak, (b) the first valley, and (c) the second peak along with their respective linear fits and 80% prediction intervals are shown. Their corresponding locations on the temporal data are illustrated in (d).

Figure 6.7 shows an analysis of the measured absorbance metric at the peaks and valley. The values for the first peak, the valley, and the second peak are plotted as a function of concentration in Figure 6.7(a-c) along with a linear fit and an 80% prediction interval to determine the applicability of using these values to determine concentration. Figure 6.7(d) shows corresponding positions of these data points for a selected trial at a sample concentration of 0.3 mg/mL ( $4.51 \mu\text{M}$ ). For all three positions, the linear fit and prediction intervals show strong monotonic relationships between the absorbance metric value and the concentration. In particular, the second peak shows the strongest linear relationship, with a slope of  $0.892 \mu\text{M}^{-1}$ , compared to slopes of the first peak and valley, respectively  $0.453 \mu\text{M}^{-1}$  and  $0.515 \mu\text{M}^{-1}$ . Therefore, the second peak demonstrates the best sensitivity for a colorimetric assay.

### 6.3 Conclusion

Absorbance-based colorimetry on a sessile droplet on a nonwetting substrate is conducted. A discernable trend is demonstrated in a case where the sample and reagent are pre-mixed before measuring the resultant droplet. Then, the sample and reagent are mixed *in situ* and measured throughout the process to show the signal output resulting from competing effects between buoyancy-induced mixing, the reaction between the sample and reagent, and the adsorption of the protein molecules onto the nonwetting substrate. Analysis of videos of the reacting medium shows the regions where each of these effects dominates the droplet absorbance. Quantitative analysis demonstrates that the second peak in absorbance measurement provides the most reliable quantity to make absorbance measurements in an *in situ* mixing apparatus. Overall, this approach provides a promising alternative to microwells in high-throughput parallel assays due to the simple fabrication and the passive mixing that overcomes micromixing challenges.

## CHAPTER 7. CONCLUSIONS AND FUTURE WORK

The primary objective of this doctoral thesis is to establish thermal and fluidic characteristics of organic and aqueous droplets on nonwetting substrates and apply the knowledge thereof to a device concept. The results include physics-based understanding of the evaporation process of droplets and the relative impacts of several internal and external mechanisms. The key outcomes of this dissertation are summarized in this chapter, followed by future avenues for research to expand upon the research into applications of these mechanisms.

### 7.1 Conclusions

Chapter 3 explores the application of multiframe super-resolution as a technique for enhancing the resolution of temperature maps produced using infrared thermography. Results are shown for both experimental and simulation results to depict the bounds of super-resolution performance enhancement. Overall, multiframe super-resolution is a valuable technique to improve upon the native resolution for the camera with simple modifications.

- Multiframe super-resolution significantly improves the correction of emissivity nonuniformity in temperature maps compared to the low-resolution maps. This was shown using uniform temperature computer memory card with significant emissivity nonuniformity.
- Super-resolution shows the greatest performance benefit for capturing features approaching a single pixel size. It provides little benefit for features that are much smaller or much larger than a pixel.
- Registration uncertainty of the shifted images is a relatively minor concern when the camera position is known *a priori*. Camera noise a negligible source of error for larger features but negatively impacts the peak performance.

Chapter 4 demonstrates the application of infrared thermography to simultaneously capture the interface temperature profile. Simultaneously, the technique allows for the capture of both the volume and shape evolution of the droplet. Through this technique it is possible to develop a better understanding of droplet evaporation characteristics on nonwetting substrates to confirm results from previous modeling efforts in the area.

- A robust reflection correction algorithm is an important feature to make accurate interface temperature measurements. This becomes more significant when the angle between the droplet surface normal and the camera view increases.
- Evaporative cooling and a counteracting natural convection plays a significant role in the temperature profile of the droplet, thus significantly impacting the local evaporation profile. This concept is extremely important for accurate modeling of evaporation times and volume evolution.
- The use of an infrared camera allows for the capture of physical parameters of the droplet such as the volume, contact angle, and contact radius. This, in turn, enables the calculation of the evaporation rate of the droplet as a function of time, thus capturing the important features of the droplet's evaporation for accurate characterization and model validation.

In Chapter 5, the evaporation and flow behavior of organic liquid droplets on nonwetting surfaces are explored. Through PIV and temperature measurements, the thermofluidic characteristics of the droplet's evaporation are detailed.

- PIV measurements of the velocity profiles show the flow directions and, combined with the measurement of the temperature profile, confirms that flow in organic liquid droplets on nonwetting surfaces are driven by surface tension gradients.
- Scaling analysis shows that interface velocity is proportional to the Marangoni velocity prediction.
- A novel reduced-order model allows for the inclusion of internal advection to model the interface temperature and local evaporation rate. This model is demonstrated to be significantly more accurate at predicting experimental temperature measurements than models that do not account for evaporative cooling and internal advection.

Chapter 6 demonstrates the application of an evaporating droplet on a nonwetting substrate as a chamber for a colorimetric reaction to determine the concentration of protein sample in a solution. A sessile droplet serves as a promising alternative to complex devices and microwells for high-throughput colorimetric analysis.

- Pre-mixed solutions of sample with reagent dye are used to demonstrate that absorbance measurements can be made through droplets to accurately measure the color and, therefore, the concentration of protein in the solution.

- Mixing the sample and reagent *in situ* results in an absorbance signal that demonstrates a complex interaction between the mixing, the reaction, and the adsorption of the protein into the substrate.
- Despite complex interactions, the absorbance peak and valley values track strongly with the concentration of protein, confirming the suitability of this approach for quantitation.

## 7.2 Future Works

This section proposes plans for future studies. The overall goal is to expand upon the promising results of the previous chapter in the development of absorbance-based colorimetry in sessile droplets.

- One method to enhance the system as it exists currently is heating the substrate to increase the mixing speed of the droplet. Ideally, the increased mixing would allow the reaction to be completed more rapidly and allow for the measurement to be conducted more rapidly. The increased temperature will also have the detrimental effect of accelerating the evaporation of the droplet. An experimental study would be needed to confirm that the absorbance measurement can be conducted before the completion of evaporation. Another aspect to explore is the change in relative dominance of the mechanisms that affect the absorbance measurement. The timescale of mixing should be significantly accelerated and the temperature dependence of the reaction would also impact the absorbance signal.
- Another expansion of this concept is the use of superhydrophobic surfaces as the substrate for the device. These surfaces have three important benefits that improve colorimetric measurements of protein. The first benefit is the reduced adsorption of protein onto superhydrophobic surfaces of low roughness scales. This allows for more reliable measurements and removes an extraneous variable in the signal. The second benefit is that mixing is further enhanced on superhydrophobic surfaces, often by an order of magnitude. This is achieved without any of the additional concerns introduced by heating the substrate. Lastly, superhydrophobic substrates have significantly lower evaporation rates due to evaporation suppression via vapor confinement at the contact line. This further enhances the reliability of measurements by reducing loss of sample.
- Finally, the concepts discussed can be further applied to an array of droplets. This is the intended goal of such a method as it is an alternative method to microwells. Droplets have

a low size profile allowing for a large array of parallel measurements and achieves this without the need for complex machining or manufacturing.

## REFERENCES

- [1] Dugas, V., Broutin, J., and Souteyrand, E., 2005, “Droplet Evaporation Study Applied to DNA Chip Manufacturing,” *Langmuir*, **21**(20), pp. 9130–9136.
- [2] Angelis, F. D., Gentile, F., Mearini, F., Das, G., Moretti, M., Candeloro, P., Coluccio, M. L., Cojoc, G., Accardo, A., Liberale, C., Zaccaria, R. P., Perozziello, G., Tirinato, L., Toma, A., Cuda, G., Cingolani, R., and Fabrizio, E. D., 2011, “Breaking the Diffusion Limit with Super-Hydrophobic Delivery of Molecules to Plasmonic Nanofocusing SERS Structures,” *Nat Photon*, **5**(11), pp. 682–687.
- [3] Ebrahimi, A., Dak, P., Salm, E., Dash, S., V. Garimella, S., Bashir, R., and A. Alam, M., 2013, “Nanotextured Superhydrophobic Electrodes Enable Detection of Attomolar-Scale DNA Concentration within a Droplet by Non-Faradaic Impedance Spectroscopy,” *Lab on a Chip*, **13**(21), pp. 4248–4256.
- [4] Dak, P., Ebrahimi, A., Swaminathan, V., Duarte-Guevara, C., Bashir, R., and Alam, M. A., 2016, “Droplet-Based Biosensing for Lab-on-a-Chip, Open Microfluidics Platforms,” *Biosensors*, **6**(2), p. 14.
- [5] Dash, S., Chandramohan, A., Weibel, J. A., and Garimella, S. V., 2014, “Buoyancy-Induced on-the-Spot Mixing in Droplets Evaporating on Nonwetting Surfaces,” *Phys. Rev. E*, **90**(6), p. 062407.
- [6] Soltman, D., and Subramanian, V., 2008, “Inkjet-Printed Line Morphologies and Temperature Control of the Coffee Ring Effect,” *Langmuir*, **24**(5), pp. 2224–2231.
- [7] Dicuango, M., Dash, S., Weibel, J. A., and Garimella, S. V., 2014, “Effect of Superhydrophobic Surface Morphology on Evaporative Deposition Patterns,” *Applied Physics Letters*, **104**(20), p. 201604.
- [8] Smith, P. J., Shin, D.-Y., Stringer, J. E., Derby, B., and Reis, N., 2006, “Direct Ink-Jet Printing and Low Temperature Conversion of Conductive Silver Patterns,” *J. Mater. Sci.*, **41**(13), pp. 4153–4158.
- [9] Sekitani, T., Noguchi, Y., Zschieschang, U., Klauk, H., and Someya, T., 2008, “Organic Transistors Manufactured Using Inkjet Technology with Subfemtoliter Accuracy,” *PNAS*, **105**(13), pp. 4976–4980.

- [10] Garcia-Egido, E., Spikmans, V., Wong, S. Y. F., and Warrington, B. H., 2003, "Synthesis and Analysis of Combinatorial Libraries Performed in an Automated Micro Reactor System," *Lab Chip*, **3**(2), p. 73.
- [11] Park, S. C., Park, M. K., and Kang, M. G., 2003, "Super-Resolution Image Reconstruction: A Technical Overview," *IEEE Signal Processing Magazine*, **20**(3), pp. 21–36.
- [12] Ur, H., and Gross, D., 1992, "Improved Resolution from Subpixel Shifted Pictures," *CVGIP: Graphical Models and Image Processing*, **54**(2), pp. 181–186.
- [13] Vandewalle, P., Süsstrunk, S., and Vetterli, M., 2006, "A Frequency Domain Approach to Registration of Aliased Images with Application to Super-Resolution," *EURASIP J. Appl. Signal Process.*, **2006**, pp. 233–233.
- [14] Banham, M. R., and Katsaggelos, A. K., 1997, "Digital Image Restoration," *IEEE Signal Processing Magazine*, **14**(2), pp. 24–41.
- [15] Hong, M.-C., Kang, M. G., and Katsaggelos, A. K., 1997, "An Iterative Weighted Regularized Algorithm for Improving the Resolution of Video Sequences," *Proceedings of International Conference on Image Processing*, pp. 474–477.
- [16] Karch, B. K., and Hardie, R. C., 2015, "Robust Super-Resolution by Fusion of Interpolated Frames for Color and Grayscale Images," *Front. Phys.*, **3**, p. 28.
- [17] Kendig, D., Yazawa, K., Marconnet, A., Asheghi, M., and Shakouri, A., 2012, "Side-by-Side Comparison between Infrared and Thermoreflectance Imaging Using a Thermal Test Chip with Embedded Diode Temperature Sensors," *2012 28th Annual IEEE Semiconductor Thermal Measurement and Management Symposium (SEMI-THERM)*, pp. 344–347.
- [18] Trigg, A., 2003, "Applications of Infrared Microscopy to IC and MEMS Packaging," *IEEE Transactions on Electronics Packaging Manufacturing*, **26**(3), pp. 232–238.
- [19] Ziabari, A., Xuan, Y., Bahk, J. H., Parsa, M., Ye, P., and Shakouri, A., 2017, "Sub-Diffraction Thermoreflectance Thermal Imaging Using Image Reconstruction," *2017 16th IEEE Intersociety Conference on Thermal and Thermomechanical Phenomena in Electronic Systems (ITherm)*, pp. 122–127.
- [20] Atkinson, P. M., 2009, "Issues of Uncertainty in Super-Resolution Mapping and Their Implications for the Design of an Inter-Comparison Study," *International Journal of Remote Sensing*, **30**(20), pp. 5293–5308.

- [21] Baker, S., and Kanade, T., 2002, “Limits on Super-Resolution and How to Break Them,” *IEEE Transactions on Pattern Analysis and Machine Intelligence*, **24**(9), pp. 1167–1183.
- [22] Robinson, D., and Milanfar, P., 2006, “Statistical Performance Analysis of Super-Resolution,” *IEEE Transactions on Image Processing*, **15**(6), pp. 1413–1428.
- [23] Ng, M. K., and Bose, N. K., 2003, “Mathematical Analysis of Super-Resolution Methodology,” *IEEE Signal Processing Magazine*, **20**(3), pp. 62–74.
- [24] Milanfar, P., 2010, *Super-Resolution Imaging*, CRC Press.
- [25] Pickup, L. C., Capel, D. P., Roberts, S. J., and Zisserman, A., 2007, “Overcoming Registration Uncertainty in Image Super-Resolution: Maximize or Marginalize?,” *EURASIP J. Adv. Signal Process.*, **2007**(1), p. 023565.
- [26] Richards, C. D., and Richards, R. F., 1998, “Transient Temperature Measurements in a Convectively Cooled Droplet,” *Experiments in Fluids*, **25**(5–6), pp. 392–400.
- [27] David, S., Sefiane, K., and Tadrist, L., 2007, “Experimental Investigation of the Effect of Thermal Properties of the Substrate in the Wetting and Evaporation of Sessile Drops,” *Colloids and Surfaces A: Physicochemical and Engineering Aspects*, **298**(1–2), pp. 108–114.
- [28] Chandramohan, A., Dash, S., Weibel, J. A., Chen, X., and Garimella, S. V., 2016, “Marangoni Convection in Evaporating Organic Liquid Droplets on a Nonwetting Substrate,” *Langmuir*, **32**(19), pp. 4729–4735.
- [29] Dehaeck, S., Rednikov, A., and Colinet, P., 2014, “Vapor-Based Interferometric Measurement of Local Evaporation Rate and Interfacial Temperature of Evaporating Droplets,” *Langmuir*, **30**(8), pp. 2002–2008.
- [30] Fabien, G., Antoni, M., and Sefiane, K., 2011, “Use of IR Thermography To Investigate Heated Droplet Evaporation and Contact Line Dynamics,” *Langmuir*, **27**(11), pp. 6744–6752.
- [31] Sobac, B., and Brutin, D., 2012, “Thermal Effects of the Substrate on Water Droplet Evaporation,” *Phys. Rev. E*, **86**(2), p. 021602.
- [32] Sefiane, K., Moffat, J. R., Matar, O. K., and Craster, R. V., 2008, “Self-Excited Hydrothermal Waves in Evaporating Sessile Drops,” *Applied Physics Letters*, **93**(7), p. 074103.

- [33] Sefiane, K., Fukatani, Y., Takata, Y., and Kim, J., 2013, “Thermal Patterns and Hydrothermal Waves (HTWs) in Volatile Drops,” *Langmuir*, **29**(31), pp. 9750–9760.
- [34] Irvine, W. M., and Pollack, J. B., 1968, “Infrared Optical Properties of Water and Ice Spheres,” *Icarus*, **8**(1), pp. 324–360.
- [35] Girard, F., Antoni, M., and Sefiane, K., 2010, “Infrared Thermography Investigation of an Evaporating Sessile Water Droplet on Heated Substrates,” *Langmuir*, **26**(7), pp. 4576–4580.
- [36] Saha, A., Basu, S., Suryanarayana, C., and Kumar, R., 2010, “Experimental Analysis of Thermo-Physical Processes in Acoustically Levitated Heated Droplets,” *International Journal of Heat and Mass Transfer*, **53**(25–26), pp. 5663–5674.
- [37] Tam, D., von Arnim, V., McKinley, G. H., and Hosoi, A. E., 2009, “Marangoni Convection in Droplets on Superhydrophobic Surfaces,” *Journal of Fluid Mechanics*, **624**, pp. 101–123.
- [38] Meola, C., and Carlomagno, G. M., 2004, “Recent Advances in the Use of Infrared Thermography,” *Meas. Sci. Technol.*, **15**(9), p. R27.
- [39] Picknett, R. G., and Bexon, R., 1977, “The Evaporation of Sessile or Pendant Drops in Still Air,” *Journal of Colloid and Interface Science*, **61**(2), pp. 336–350.
- [40] Maxwell, J. C., 1890, “Diffusion,” *The Scientific Papers of James Clerk Maxwell*, Cambridge University Press, p. 625.
- [41] Deegan, R. D., Bakajin, O., Dupont, T. F., Huber, G., Nagel, S. R., and Witten, T. A., 1997, “Capillary Flow as the Cause of Ring Stains from Dried Liquid Drops,” *Nature*, **389**(6653), pp. 827–829.
- [42] Deegan, R. D., Bakajin, O., Dupont, T. F., Huber, G., Nagel, S. R., and Witten, T. A., 2000, “Contact Line Deposits in an Evaporating Drop,” *Phys. Rev. E*, **62**(1), pp. 756–765.
- [43] Hu, H., and Larson, R. G., 2002, “Evaporation of a Sessile Droplet on a Substrate,” *J. Phys. Chem. B*, **106**(6), pp. 1334–1344.
- [44] Popov, Y. O., 2005, “Evaporative Deposition Patterns: Spatial Dimensions of the Deposit,” *Phys. Rev. E*, **71**(3), p. 036313.
- [45] Pan, Z., Dash, S., Weibel, J. A., and Garimella, S. V., 2013, “Assessment of Water Droplet Evaporation Mechanisms on Hydrophobic and Superhydrophobic Substrates,” *Langmuir*, **29**(51), pp. 15831–15841.

- [46] Saada, M. A., Chikh, S., and Tadrist, L., 2010, “Numerical Investigation of Heat and Mass Transfer of an Evaporating Sessile Drop on a Horizontal Surface,” *Physics of Fluids* (1994-present), **22**(11), p. 112115.
- [47] Zheng, Z., Zhou, L., Du, X., and Yang, Y., 2016, “Numerical Investigation on Conjugate Heat Transfer of Evaporating Thin Film in a Sessile Droplet,” *International Journal of Heat and Mass Transfer*, **101**, pp. 10–19.
- [48] Carle, F., Semenov, S., Medale, M., and Brutin, D., 2016, “Contribution of Convective Transport to Evaporation of Sessile Droplets: Empirical Model,” *International Journal of Thermal Sciences*, **101**, pp. 35–47.
- [49] Dash, S., and Garimella, S. V., 2013, “Droplet Evaporation Dynamics on a Superhydrophobic Surface with Negligible Hysteresis,” *Langmuir*, **29**(34), pp. 10785–10795.
- [50] Pan, Z., Weibel, J. A., and Garimella, S. V., 2014, “Influence of Surface Wettability on Transport Mechanisms Governing Water Droplet Evaporation,” *Langmuir*, **30**(32), pp. 9726–9730.
- [51] Gleason, K., and Putnam, S. A., 2014, “Microdroplet Evaporation with a Forced Pinned Contact Line,” *Langmuir*, **30**(34), pp. 10548–10555.
- [52] Hofmann, H. E., 1932, “Evaporation Rates of Organic Liquids,” *Ind. Eng. Chem.*, **24**(2), pp. 135–140.
- [53] Levitsky, D. I., Ponomarev, M. A., Geeves, M. A., Shnyrov, V. L., and Manstein, D. J., 1998, “Differential Scanning Calorimetric Study of the Thermal Unfolding of the Motor Domain Fragments of Dictyostelium Discoideum Myosin II,” *European Journal of Biochemistry*, **251**(1–2), pp. 275–280.
- [54] Hu, H., and Larson, R. G., 2005, “Analysis of the Effects of Marangoni Stresses on the Microflow in an Evaporating Sessile Droplet,” *Langmuir*, **21**(9), pp. 3972–3980.
- [55] Hu, H., and Larson, R. G., 2006, “Marangoni Effect Reverses Coffee-Ring Depositions,” *J. Phys. Chem. B*, **110**(14), pp. 7090–7094.
- [56] Nguyen, V. X., and Stebe, K. J., 2002, “Patterning of Small Particles by a Surfactant-Enhanced Marangoni-Bénard Instability,” *Phys. Rev. Lett.*, **88**(16), p. 164501.

- [57] Ristenpart, W. D., Kim, P. G., Domingues, C., Wan, J., and Stone, H. A., 2007, "Influence of Substrate Conductivity on Circulation Reversal in Evaporating Drops," *Phys. Rev. Lett.*, **99**(23), p. 234502.
- [58] Dunn, G. J., Wilson, S. K., Duffy, B. R., David, S., and Sefiane, K., 2009, "The Strong Influence of Substrate Conductivity on Droplet Evaporation," *Journal of Fluid Mechanics*, **623**, pp. 329–351.
- [59] Sodtke, C., Ajaev, V. S., and Stephan, P., 2008, "Dynamics of Volatile Liquid Droplets on Heated Surfaces: Theory versus Experiment," *Journal of Fluid Mechanics*, **610**, pp. 343–362.
- [60] Starov, V., and Sefiane, K., 2009, "On Evaporation Rate and Interfacial Temperature of Volatile Sessile Drops," *Colloids and Surfaces A: Physicochemical and Engineering Aspects*, **333**(1–3), pp. 170–174.
- [61] Karapetsas, G., Matar, O. K., Valluri, P., and Sefiane, K., 2012, "Convective Rolls and Hydrothermal Waves in Evaporating Sessile Drops," *Langmuir*, **28**(31), pp. 11433–11439.
- [62] Hegseth, J. J., Rashidnia, N., and Chai, A., 1996, "Natural Convection in Droplet Evaporation," *Phys. Rev. E*, **54**(2), pp. 1640–1644.
- [63] Brutin, D., Sobac, B., Rigollet, F., and Le Niliot, C., 2011, "Infrared Visualization of Thermal Motion inside a Sessile Drop Deposited onto a Heated Surface," *Experimental Thermal and Fluid Science*, **35**(3), pp. 521–530.
- [64] Dunn, G. J., Wilson, S. K., Duffy, B. R., David, S., and Sefiane, K., 2008, "A Mathematical Model for the Evaporation of a Thin Sessile Liquid Droplet: Comparison between Experiment and Theory," *Colloids and Surfaces A: Physicochemical and Engineering Aspects*, **323**(1–3), pp. 50–55.
- [65] Sodtke, C., Ajaev, V. S., and Stephan, P., 2006, "Evaporation of Thin Liquid Droplets on Heated Surfaces," *Heat Mass Transfer*, **43**(7), pp. 649–657.
- [66] Im, M., Im, H., Lee, J.-H., Yoon, J.-B., and Choi, Y.-K., 2010, "A Robust Superhydrophobic and Superoleophobic Surface with Inverse-Trapezoidal Microstructures on a Large Transparent Flexible Substrate," *Soft Matter*, **6**(7), p. 1401.
- [67] Liu, T. L., and Kim, C.-J. C., 2014, "Turning a Surface Superrepellent Even to Completely Wetting Liquids," *Science*, **346**(6213), pp. 1096–1100.

- [68] Weisensee, P. B., Torrealba, E. J., Raleigh, M., Jacobi, A. M., and King, W. P., 2014, “Hydrophobic and Oleophobic Re-Entrant Steel Microstructures Fabricated Using Micro Electrical Discharge Machining,” *J. Micromech. Microeng.*, **24**(9), p. 095020.
- [69] Tuteja, A., Choi, W., Mabry, J. M., McKinley, G. H., and Cohen, R. E., 2008, “Robust Omniphobic Surfaces,” *PNAS*, **105**(47), pp. 18200–18205.
- [70] Grigoryev, A., Tokarev, I., Kornev, K. G., Luzinov, I., and Minko, S., 2012, “Superomniphobic Magnetic Microtextures with Remote Wetting Control,” *J. Am. Chem. Soc.*, **134**(31), pp. 12916–12919.
- [71] Dash, S., and Garimella, S. V., 2014, “Droplet Evaporation on Heated Hydrophobic and Superhydrophobic Surfaces,” *Phys. Rev. E*, **89**(4), p. 042402.
- [72] Chen, X., Weibel, J. A., and Garimella, S. V., 2015, “Water and Ethanol Droplet Wetting Transition during Evaporation on Omniphobic Surfaces,” *Sci Rep*, **5**, p. 17110.
- [73] Compton, S. J., and Jones, C. G., 1985, “Mechanism of Dye Response and Interference in the Bradford Protein Assay,” *Analytical Biochemistry*, **151**(2), pp. 369–374.
- [74] Georgiou, C. D., Grintzalis, K., Zervoudakis, G., and Papapostolou, I., 2008, “Mechanism of Coomassie Brilliant Blue G-250 Binding to Proteins: A Hydrophobic Assay for Nanogram Quantities of Proteins,” *Anal Bioanal Chem*, **391**(1), pp. 391–403.
- [75] Bradford, M. M., 1976, “A Rapid and Sensitive Method for the Quantitation of Microgram Quantities of Protein Utilizing the Principle of Protein-Dye Binding,” *Analytical Biochemistry*, **72**(1), pp. 248–254.
- [76] Olson, B. J. S. C., and Markwell, J., “Assays for Determination of Protein Concentration,” *Current Protocols in Protein Science*, **48**(1), pp. 3.4.1-3.4.29.
- [77] Kruger, N. J., 2009, “The Bradford Method For Protein Quantitation,” *The Protein Protocols Handbook*, J.M. Walker, ed., Humana Press, Totowa, NJ, pp. 17–24.
- [78] Srinivasan, V., K. Pamula, V., and B. Fair, R., 2004, “An Integrated Digital Microfluidic Lab-on-a-Chip for Clinical Diagnostics on Human Physiological Fluids,” *Lab on a Chip*, **4**(4), pp. 310–315.
- [79] Liu, S., Su, W., and Ding, X., 2016, “A Review on Microfluidic Paper-Based Analytical Devices for Glucose Detection,” *Sensors*, **16**(12), p. 2086.

- [80] Zhu, L., Feng, Y., Ye, X., Feng, J., Wu, Y., and Zhou, Z., 2012, “An ELISA Chip Based on an EWOD Microfluidic Platform,” *Journal of Adhesion Science and Technology*, **26**(12–17), pp. 2113–2124.
- [81] Yoon, J.-Y., and Garrell, R. L., 2003, “Preventing Biomolecular Adsorption in Electrowetting-Based Biofluidic Chips,” *Anal. Chem.*, **75**(19), pp. 5097–5102.
- [82] Pollack, M. G., Shenderov, A. D., and Fair, R. B., 2002, “Electrowetting-Based Actuation of Droplets for Integrated Microfluidics,” *Lab Chip*, **2**(2), pp. 96–101.
- [83] Li, X., Ballerini, D. R., and Shen, W., 2012, “A Perspective on Paper-Based Microfluidics: Current Status and Future Trends,” *Biomicrofluidics*, **6**(1), p. 011301.
- [84] Hernandez-Perez, R., Fan, Z. H., and Garcia-Cordero, J. L., 2016, “Evaporation-Driven Bioassays in Suspended Droplets,” *Anal. Chem.*, **88**(14), pp. 7312–7317.
- [85] Mayr, L. M., and Fuerst, P., 2008, “The Future of High-Throughput Screening,” *J Biomol Screen*, **13**(6), pp. 443–448.
- [86] Lye, J. K. K., Ng, T. W., Neild, A., and Liew, O. W., 2011, “A Capacity for Mixing in Capillary Wells for Microplates,” *Analytical Biochemistry*, **410**(1), pp. 152–154.
- [87] Sarafoff, N. I., Bieschke, J., Giese, A., Weber, P., Bertsch, U., and Kretzschmar, H. A., 2005, “Automated PrPres Amplification Using Indirect Sonication,” *Journal of Biochemical and Biophysical Methods*, **63**(3), pp. 213–221.
- [88] Oberti, S., Neild, A., and Ng, T. W., 2009, “Microfluidic Mixing under Low Frequency Vibration,” *Lab Chip*, **9**(10), pp. 1435–1438.
- [89] Yi, M., Qian, S., and Bau, H. H., 2002, “A Magneto-hydrodynamic Chaotic Stirrer,” *Journal of Fluid Mechanics*, **468**, pp. 153–177.
- [90] Sadr, R., Yoda, M., Zheng, Z., and Conlisk, A. T., 2004, “An Experimental Study of Electro-Osmotic Flow in Rectangular Microchannels,” *Journal of Fluid Mechanics*, **506**, pp. 357–367.
- [91] Schönfeld, F., Hessel, V., and Hofmann, C., 2004, “An Optimised Split-and-Recombine Micro-Mixer with Uniform ‘Chaotic’ Mixing,” *Lab on a Chip*, **4**(1), pp. 65–69.
- [92] Dash, S., and Garimella, S. V., 2013, “Droplet Evaporation Dynamics on a Superhydrophobic Surface with Negligible Hysteresis,” *Langmuir*, **29**(34), pp. 10785–10795.

- [93] Pan, Z., Dash, S., Weibel, J. A., and Garimella, S. V., 2013, “Assessment of Water Droplet Evaporation Mechanisms on Hydrophobic and Superhydrophobic Substrates,” *Langmuir*, **29**(51), pp. 15831–15841.
- [94] Chandramohan, A., Weibel, J. A., and Garimella, S. V., 2017, “Spatiotemporal Infrared Measurement of Interface Temperatures during Water Droplet Evaporation on a Nonwetting Substrate,” *Appl. Phys. Lett.*, **110**(4), p. 041605.
- [95] Dash, S., Chandramohan, A., Weibel, J. A., and Garimella, S. V., 2014, “Buoyancy-Induced on-the-Spot Mixing in Droplets Evaporating on Nonwetting Surfaces,” *Phys. Rev. E*, **90**(6), p. 062407.
- [96] Chandramohan, A., Lyons, S. K., Weibel, J. A., and Garimella, S. V., 2018, “Error Reduction in Infrared Thermography by Multiframe Super-Resolution,” *J. Electron. Packag.*, **140**(4), pp. 041008-041008–8.
- [97] Bevington, P. R., and Robinson, D. K., 2003, *Data Reduction and Error Analysis for the Physical Sciences*, McGraw-Hill.
- [98] 2007, *MATLAB Reference Manual*, The Mathworks, Inc., Natick, MA.
- [99] Vellvehi, M., Perpiñà, X., Lauro, G. L., Perillo, F., and Jordà, X., 2011, “Irradiance-Based Emissivity Correction in Infrared Thermography for Electronic Applications,” *Review of Scientific Instruments*, **82**(11), p. 114901.
- [100] Huang, S., Sun, J., Yang, Y., Fang, Y., and Lin, P., 2017, “Multi-Frame Super-Resolution Reconstruction Based on Gradient Vector Flow Hybrid Field,” *IEEE Access*, **5**, pp. 21669–21683.
- [101] Lu, H., Li, Y., Nakashima, S., Kim, H., and Serikawa, S., 2017, “Underwater Image Super-Resolution by Descattering and Fusion,” *IEEE Access*, **5**, pp. 670–679.
- [102] Modest, M. F., 2013, *Radiative Heat Transfer*, Academic Press.
- [103] Gleason, K., Voota, H., and Putnam, S. A., 2016, “Steady-State Droplet Evaporation: Contact Angle Influence on the Evaporation Efficiency,” *International Journal of Heat and Mass Transfer*, **101**, pp. 418–426.
- [104] Salm, E., Guevara, C. D., Dak, P., Dorvel, B. R., Reddy, B., Alam, M. A., and Bashir, R., 2013, “Ultralocalized Thermal Reactions in Subnanoliter Droplets-in-Air,” *PNAS*, **110**(9), pp. 3310–3315.

- [105] Ahmed, B., Barrow, D., and Wirth, T., 2006, "Enhancement of Reaction Rates by Segmented Fluid Flow in Capillary Scale Reactors," *Adv. Synth. Catal.*, **348**(9), pp. 1043–1048.
- [106] Teh, S.-Y., Lin, R., Hung, L.-H., and Lee, A. P., 2008, "Droplet Microfluidics," *Lab on a Chip*, **8**(2), p. 198.
- [107] Kim, H., Vishniakou, S., and Faris, G. W., 2009, "Petri Dish PCR: Laser-Heated Reactions in Nanoliter Droplet Arrays," *Lab on a Chip*, **9**(9), p. 1230.
- [108] Zhang, Y., Zhu, Y., Yao, B., and Fang, Q., 2011, "Nanolitre Droplet Array for Real Time Reverse Transcription Polymerase Chain Reaction," *Lab on a Chip*, **11**(8), p. 1545.
- [109] Chen, X., Weibel, J. A., and Garimella, S. V., 2015, "Superhydrophobic Surfaces: Exploiting Microscale Roughness on Hierarchical Superhydrophobic Copper Surfaces for Enhanced Dropwise Condensation (Adv. Mater. Interfaces 3/2015)," *Adv. Mater. Interfaces*, **2**(3), p. 1400480.
- [110] Cabrera, H., Marcano, A., and Castellanos, Y., 2006, "Absorption Coefficient of Nearly Transparent Liquids Measured Using Thermal Lens Spectroscopy," *Condensed Matter Physics*, **9**(2), pp. 385–389.
- [111] Xu, X., Luo, J., and Guo, D., 2010, "Criterion for Reversal of Thermal Marangoni Flow in Drying Drops," *Langmuir*, **26**(3), pp. 1918–1922.
- [112] Sefiane, K., Wilson, S. K., David, S., Dunn, G. J., and Duffy, B. R., 2009, "On the Effect of the Atmosphere on the Evaporation of Sessile Droplets of Water," *Physics of Fluids*, **21**(6), p. 062101.
- [113] Lemmon, E. W., McLinden, M. O., and Friend, D. G., 2005, "Thermophysical Properties of Fluid Systems," *NIST Chemistry Webbook, NIST Standard Reference Database 69*.
- [114] Kang, K. H., Lee, S. J., Lee, C. M., and Kang, I. S., 2004, "Quantitative Visualization of Flow inside an Evaporating Droplet Using the Ray Tracing Method," *Meas. Sci. Technol.*, **15**(6), p. 1104.
- [115] Burns, G. W., Scroger, M. G., Strouse, G. F., Croarkin, M. C., and Guthrie, W. F., 1993, "Temperature-Electromotive Force Reference Functions and Tables for the Letter-Designated Thermocouple Types Based on the ITS-90," *National Institute of Standards and Technology Monograph 175*, p. 630.

- [116] Brown, K. K., Coleman, H. W., and Steele, W. G., 1995, “Estimating Uncertainty Intervals for Linear Regression,” Proceedings of the 33rd American Institute of Aeronautics and Astronautics Aerospace Sciences Meeting and Exhibit., pp. 9–12.
- [117] Modest, M. F., 2003, *Radiative Heat Transfer*, Academic Press.
- [118] Ranz, W. E., and Marshall, W. R., 1952, “Evaporation from Drops,” Chem. Eng. Prog., **48**(3), pp. 141–146.
- [119] Frank P. Incropera, David P. Dewitt, Theodore L. Bergman, and Adrienne S. Lavine, 2011, *Fundamentals of Heat and Mass Transfer*, John Wiley & Sons.
- [120] Levi-Hevroni, D., Levy, A., and Borde, I., 1995, “Mathematical Modeling of Drying of Liquid/Solid Slurries in Steady State One-Dimensional Flow,” Drying Technology, **13**(5–7), pp. 1187–1201.
- [121] Maitra, T., Tiwari, M. K., Antonini, C., Schoch, P., Jung, S., Eberle, P., and Poulikakos, D., 2014, “On the Nanoengineering of Superhydrophobic and Impalement Resistant Surface Textures below the Freezing Temperature,” Nano Lett., **14**(1), pp. 172–182.
- [122] Barrow, H., 1985, “A Note on Frosting of Heat Pump Evaporator Surfaces,” Journal of Heat Recovery Systems, **5**(3), pp. 195–201.
- [123] Martínez-Frías, J., and Aceves, S. M., 1999, “Effects of Evaporator Frosting on the Performance of an Air-to-Air Heat Pump,” J. Energy Resour. Technol, **121**(1), pp. 60–65.
- [124] Green, B., 1986, “Cold Weather Flying,” Hospital Aviation, **5**(11), pp. 6–8.
- [125] Peck, L., Ryerson, C. C., and Martel, C. J., 2002, *Army Aircraft Icing*.
- [126] Farber, J. M., and Todd, E. C., 2000, *Safe Handling of Foods*, CRC Press.
- [127] Guo, X.-M., Chen, Y.-G., Wang, W.-H., and Chen, C.-Z., 2008, “Experimental Study on Frost Growth and Dynamic Performance of Air Source Heat Pump System,” Applied Thermal Engineering, **28**(17–18), pp. 2267–2278.
- [128] Roberts, L., 1958, “On the Melting of a Semi-Infinite Body of Ice Placed in a Hot Stream of Air,” Journal of Fluid Mechanics, **4**(05), pp. 505–528.
- [129] Tien, C., and Y. C. Yen, 1971, “Condensation-Melting Heat Transfer,” Chemical Engineering Progress Symposium Series, **67**(113).
- [130] Nusselt, W., 1916, “Die Oberflächenkondensation Des Wasserdampfes the Surface Condensation of Water,” Zetschr. Ver. Deutch. Ing., **60**, pp. 541–546.

- [131] Galamba, D., Dhir, V. K., and Taghavi, K., 1986, "Analytical and Experimental Investigation of Simultaneous Melting-Condensation on a Vertical Wall in the Presence of a Noncondensable Gas," *International Journal of Heat and Mass Transfer*, **29**(12), pp. 1869–1880.
- [132] Y. C. Yen, A. Zehnder, S. Zavoluk, and Chi Tien, 1973, "Condensation-Melting Heat Transfer in the Presence of Air," *Chemical Engineering Progress Symposium Series*, **69**(131), pp. 23–29.
- [133] Sparrow, E. M., and Lin, S. H., 1964, "Condensation Heat Transfer in the Presence of a Noncondensable Gas," *J. Heat Transfer*, **86**(3), pp. 430–436.
- [134] Taghavi-Tafreshi, K., and Dhir, V. K., 1982, "Analytical and Experimental Investigation of Simultaneous Melting-Condensation on a Vertical Wall," *J. Heat Transfer*, **104**(1), pp. 24–33.
- [135] Epstein, M., and Cho, D. H., 1976, "Laminar Film Condensation on a Vertical Melting Surface," *J. Heat Transfer*, **98**(1), pp. 108–113.
- [136] Koh, J. C. Y., Sparrow, E. M., and Hartnett, J. P., 1961, "The Two Phase Boundary Layer in Laminar Film Condensation," *International Journal of Heat and Mass Transfer*, **2**(1–2), pp. 69–82.
- [137] J. L. Wegener, and J. A. Drallmeier, 2010, "Measurement of Thin Liquid Film Characteristics Using Laser Focus Displacement Instruments for Atomization Applications," *ILASS-Americas 22nd Annual Conference on Liquid Atomization and Spray Systems, Cincinnati, OH*.
- [138] Takamasa, T., and Kobayashi, K., 2000, "Measuring Interfacial Waves on Film Flowing down Tube Inner Wall Using Laser Focus Displacement Meter," *International Journal of Multiphase Flow*, **26**(9), pp. 1493–1507.
- [139] Pope, R. M., and Fry, E. S., 1997, "Absorption Spectrum (380-700 Nm) of Pure Water. II. Integrating Cavity Measurements," *Appl. Opt.*, **36**(33), pp. 8710–8723.

## APPENDIX A. QUANTITATIVE ANALYSIS OF MULTI-FRAME SUPER-RESOLUTION FOR EMISSIVITY-MAPPED INFRARED THERMOGRAPHY OF ELECTRONIC DEVICES

### A.1 Multiframe Super-Resolution Code

This code implement multiframe super-resolution on a given set of sub-pixel shifted images.

```

%% Super Resolution
% Program to implement super-resolution on a given set of sub-pixel shifted
images.
% This file is to be copied in the folder containing the images from the
experiment (FLIR SC7650 is the default camera considered).
% Aditya Chandramohan, 09/15/2017
clear all;
close all;
clc;
%% Section 1: User defined parameters (Requires user input)

num_images = 25;           % The number of low-resolution images that are to be
combined
width = 320;              % The width of low-resolution images in pixels
height = 256;             % The height of low-resolution images in pixels
superres_factor = 5;      % The desired factor of increase in resolution along
each axis
pix_dim = 144.318262177; % Pixel dimensions in microns
hs = 0.001;              % Tunable factor for super-resolution - does not have
any influence on greyscale, motionless images.
T_min = 20;              % Minimum temperature for image scaling
T_max = 65;              % Maximum temperature for image scaling

% Uncertainty Analysis Features
uncertainty = 0.5;       % Positional uncertainty of LR displacement in
microns
iter = 1;                % iterations of sensitivity analysis
                        % if iter = 1, just the super-res is run with no
                        % uncertainty analysis.

%% Section 2: Loading input files

filelist = dir('./results/test*.mat'); % Loads images
after processing by Run.m (which in turn uses read_altair,etc.)
input_array = zeros(height,width,num_images);
X_LR = zeros(height,width,num_images);
Y_LR = zeros(height,width,num_images);

%% Section 3: User-entry of input distances (Requires user input)
% This section requires the user to enter the sub-pixel shift of each image
in pixels.
% These are to be carefully noted during the experiment.
x = [-50 -25 0 25 50];
y = [-50 -25 0 25 50];

```

```

if method == 1
    Y = -Y;
end

dis(:,:,1) = [x(1), y(1)];
dis(:,:,2) = [x(2), y(1)];
dis(:,:,3) = [x(3), y(1)];
dis(:,:,4) = [x(4), y(1)];
dis(:,:,5) = [x(5), y(1)];
dis(:,:,6) = [x(5), y(2)];
dis(:,:,7) = [x(4), y(2)];
dis(:,:,8) = [x(3), y(2)];
dis(:,:,9) = [x(2), y(2)];
dis(:,:,10) = [x(1), y(2)];
dis(:,:,11) = [x(1), y(3)];
dis(:,:,12) = [x(2), y(3)];
dis(:,:,13) = [x(3), y(3)];
dis(:,:,14) = [x(4), y(3)];
dis(:,:,15) = [x(5), y(3)];
dis(:,:,16) = [x(5), y(4)];
dis(:,:,17) = [x(4), y(4)];
dis(:,:,18) = [x(3), y(4)];
dis(:,:,19) = [x(2), y(4)];
dis(:,:,20) = [x(1), y(4)];
dis(:,:,21) = [x(1), y(5)];
dis(:,:,22) = [x(2), y(5)];
dis(:,:,23) = [x(3), y(5)];
dis(:,:,24) = [x(4), y(5)];
dis(:,:,25) = [x(5), y(5)];
dis = dis/1000;

dis_orig = dis;
diff_std = zeros((iter-1),1);
diff_mean = zeros((iter-1),1);
diff_max = zeros((iter-1),1);
for iteration = 1:iter
    disp(iteration)
    if iteration > 1
        for k = 1:num_images
            dis(1,1,k) = dis_orig(1,1,k)+uncertainty*normrnd(0,1/3)/1000;
            dis(1,2,k) = dis_orig(1,2,k)+uncertainty*normrnd(0,1/3)/1000;
        end
    end

    for i=1:num_images
        input_cell{i} = load(['./results/' filelist(i).name]);
        input_array(:, :, i) = mean(input_cell{1,i}.Temp,3); % The images
are stored in this array
        X_LR(:, :, i) = input_cell{1,i}.xx;
        Y_LR(:, :, i) = input_cell{1,i}.yy;
    end
    %% Section 4: Bad-pixel correction (camera-specific) (Requires user input)
    for k = 1:num_images
        input_array( 10,319,k) = input_array( 10,318,k);
    end
end

```

```

input_array( 10,320,k) = input_array( 10,318,k);
input_array( 11,319,k) = input_array( 11,318,k);
input_array( 11,320,k) = input_array( 11,318,k);
input_array( 12,320,k) = input_array( 11,319,k);
input_array(164,235,k) = input_array(164,236,k);
input_array(165,235,k) = input_array(165,236,k);
input_array( 92,235,k) = input_array( 91,235,k);
input_array( 93,235,k) = input_array( 94,235,k);
end

mean_val = mean(mean(mean(input_array(50:200,50:300,13))));
for k = 1:num_images
    input_array(:, :, k) = input_array(:, :, k) -
mean2(input_array(50:200,50:300,k))+mean_val;
end
%% Section 5: Flipping of images
flipped_array = zeros(height,width,num_images);
for i=1:num_images
    flipped_array(:, :, i) = flipud(input_array(:, :, i));
end
%% Section 6: Image registration
% This section aligns all images with a single grid.
% This is to be done because the images are sub-pixel shifted (not aligned)
% Image registration algorithms are not accurate enough to be used and hence
the shifts are to be measured during the experiment
registered_array = zeros(height,width,num_images);
for k = 1:num_images
    registered_array(:, :, k) = imtranslate(flipped_array(:, :, k), -
dis(:, :, k)*1000/pix_dim);
    X_LR(:, :, k) = X_LR(:, :, k) - dis(1, 1, k);
    Y_LR(:, :, k) = Y_LR(:, :, k) - dis(1, 2, k);
end
%% Section 7: Interpolation to high-resolution dimensions
% In this section, the low-resolution images are interpolated to the high
resolution grid.
% Various interpolation methods such as nearest neighbour, bilinear, bicubic,
lanczos3

interpolated_array = imresize(registered_array, superres_factor, 'lanczos3');
interpolated_images = zeros(superres_factor*height,superres_factor*width);
for k=1:num_images
    interpolated_images(:, :, k) = flipud(interpolated_array(:, :, k));
end

%% Section 8: X-coordinate and Y-coordinate matrices(for use in displaying
the images)
% Creates the coordinate grid required to display the image
x_coord = zeros(superres_factor*height,superres_factor*width);
y_coord = zeros(superres_factor*height,superres_factor*width);
for i = 1 : superres_factor*height
    for j=1 : superres_factor*width
        x_coord(i,j) = j/superres_factor * pix_dim/1000;
        y_coord(i,j) = i/superres_factor * pix_dim/1000;
    end
end
end

```

```

X_interp = zeros(superres_factor*height,superres_factor*width,num_images);
Y_interp = zeros(superres_factor*height,superres_factor*width,num_images);
for k = 1:num_images
    X_interp(:, :, k) = x_coord-dis(1,1,k)/superres_factor;
    Y_interp(:, :, k) = y_coord-dis(1,2,k)/superres_factor;
end
%% Section 9: Super-resolution

disp('Begin Super-Resolution')

POS_HR = [x_coord(:) y_coord(:)];

xlin = linspace(min(X_LR(:)),max(X_LR(:)),superres_factor*width);
ylin = linspace(min(Y_LR(:)),max(Y_LR(:)),superres_factor*height);
[X_HR,Y_HR] = meshgrid(xlin,ylin);
superres_image =
griddata(X_LR(:),Y_LR(:),input_array(:),X_HR,Y_HR,'natural');
x_coord = X_HR;
y_coord = Y_HR;
end

superres_image = wiener2(superres_image,[6 6]); % adaptive noise filter for
reconditioning

    if iteration == 1
        SR = superres_image;
    else
        mat_diff = abs(superres_image-SR);
        fringe = 300;
        top = fringe;
        bot = size(mat_diff,1)-fringe;
        lft = fringe;
        rgt = size(mat_diff,2)-fringe;
        diff_std(iteration-1) = std2(mat_diff(top:bot,lft:rgt));
        diff_mean(iteration-1) = mean2(mat_diff(top:bot,lft:rgt));
        diff_max(iteration-1) = max(max(mat_diff(top:bot,lft:rgt)));
    end
end

%% Section 10: Displaying the low-resolution image
figure(1)
pcolor(input_array(:, :, 1));
shading flat
colormap parula
str = strcat('Low-Resolution Image
(', num2str(width), 'x', num2str(height), ')');
title(sprintf('%s', str))
axis equal
axis tight
colorbar('vert','fontsize',20);
caxis([T_min T_max])
set(gca,'fontsize',20)
xlabel('Position(mm)', 'fontsize', 20);
ylabel('Position(mm)', 'fontsize', 20);
axis([500 950 500 950]/superres_factor)

```

```

%% Section 11: Displaying the interpolated image
figure(2)
pcolor(interpolated_images(:,:,1))
shading flat
colormap parula
str = strcat('Interpolated Image
(', num2str(superres_factor*width), 'x', num2str(superres_factor*height), ')');
title(sprintf('%s', str))
axis equal
axis tight
colorbar('vert', 'fontsize', 20)
caxis([T_min T_max])
set(gca, 'fontsize', 20)
xlabel('Position(mm)', 'fontsize', 20);
ylabel('Position(mm)', 'fontsize', 20);
axis([500 950 500 950])

%% Section 12: Displaying the super-resolution image
figure(3)
h=pcolor(superres_image);
set(h, 'EdgeColor', 'none');
axis equal
colormap parula
str = strcat('Super-Resolution Image
(', num2str(superres_factor*width), 'x', num2str(superres_factor*height), ')');
title(sprintf('%s', str))
axis equal
axis tight
colorbar('vert', 'fontsize', 20)
caxis([T_min T_max])
set(gca, 'fontsize', 20)
xlabel('Position(mm)', 'fontsize', 20);
ylabel('Position(mm)', 'fontsize', 20);
axis([500 950 500 950])

%% Section 13: Plotting Data in the Spatial Coordinate System
figure(7)
subplot(1,1,1)
h=pcolor(x_coord, y_coord, superres_image);
set(h, 'EdgeColor', 'none');
axis equal
colormap parula
str = strcat('Super-Resolution Image (', num2str(superres_factor*width), '...
', num2str(superres_factor*height), ')');
title(sprintf('%s', str))
axis equal
axis tight
colorbar('vert', 'fontsize', 20)
caxis([T_min T_max])
set(gca, 'fontsize', 20)
xlabel('Position(mm)', 'fontsize', 20);
ylabel('Position(mm)', 'fontsize', 20);

%% Section 14: Saving Data

```

```
filename = 'SuperRes.mat';  
SR = superres_image;  
save(filename, 'SR', 'x_coord', 'y_coord', '-v7.3');
```

## APPENDIX B. SPATIOTEMPORAL INFRARED MEASUREMENT OF INTERFACE TEMPERATURES DURING WATER DROPLET EVAPORATION ON A NONWETTING SUBSTRATE

### B.1 Calibration and Validation of Measurement Technique

A differential blackbody calibrator (DB-04, SBIR) is used to calibrate the infrared camera over a range of temperature set points from 20°C to 60°C in 5°C increments. The blackbody generates a uniform temperature field of view with an effective surface emissivity  $\geq 0.97$ . The camera integration time is set to 1000  $\mu\text{s}$  for the recording frequency of 5 Hz. This integration time is chosen to maximize the acquired signal without saturating at the maximum calibration temperature. At each set-point temperature, the infrared camera is used to capture the digital level (DL) averaged over 20 frames (4 seconds). After capturing the calibration images, the nonuniformity is calculated. A calibration algorithm fits the DL as a function of set-point temperature with a unique fourth-order polynomial for each sensor pixel. This pixel-by-pixel calibration curve is applied to the experimental data. A sample calibration curve is shown in Figure B.1.

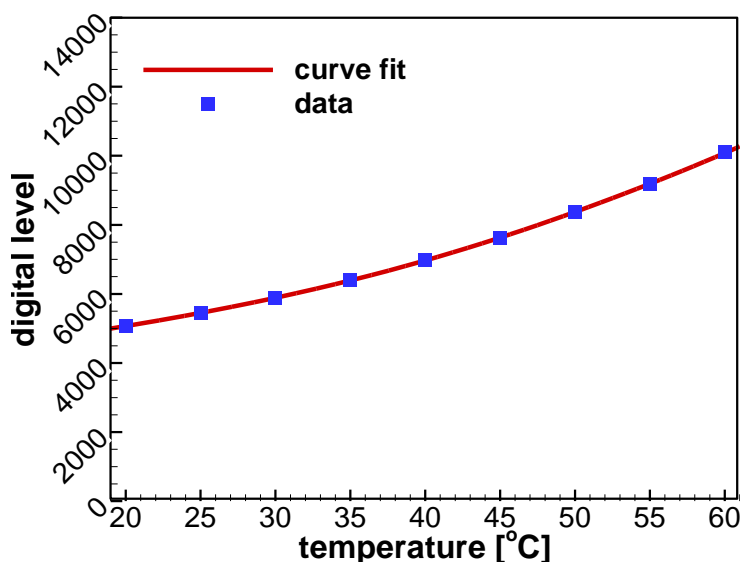


Figure B.1. Calibration curve for a single pixel in the infrared camera frame with the corresponding calibration points.

A simple experiment is used to validate the applicability of blackbody-calibrated infrared imaging to measure the temperature of a water-air interface. A small pool of water is heated uniformly from below by an insulated copper block. The copper block temperature is controlled via a feedback system (TOT-1200, Temp-o-Trol). A 75  $\mu\text{m}$ -diameter thermocouple bead is carefully submerged in the pool and positioned to within 0.2 mm of the liquid-air interface without disturbing the flat interface. This thermocouple measurement is assumed to represent the actual interface temperature of the pool because of its close proximity to the interface and small temperature gradient across the pool height. The infrared camera views the pool from above and captures an image of the surface. The infrared temperature measurements, averaged in the region around the thermocouple location, are compared to the thermocouple measurements at a range of copper block temperatures. A detailed error analysis is performed to assess the thermocouple and infrared measurement uncertainties.

The uncertainty of the thermocouple measurements is calculated using a standard propagation of errors. The thermocouple is first calibrated through the use of a dry block calibrator (CL122, Omega) based on a linear offset from a reference temperature:

$$T_{cal} - T_{ref} = m T_{ref} + b \quad (\text{D.2})$$

where  $T_{cal}$  is the calibrated thermocouple temperature,  $T_{ref}$  is the temperature reading if using the ITS-90 thermocouple calibration [115] with an ice-point reference junction,  $m$  is the slope of the linear fit, and  $b$  is the intercept. The slope and intercept are calculated based on the calibration measurements of the dry block temperature with a high-accuracy RTD (HSRTD-3-100-A-120-E, Omega), where  $T_{RTD}$  replaces the  $T_{cal}$  term. The ITS-90 temperature is calculated by converting the voltage change to a temperature value [115].

$$T_{ITS90} = c_0 + c_1 \Delta V + c_2 \Delta V^2 + c_3 \Delta V^3 + c_4 \Delta V^4 + c_5 \Delta V^5 + c_6 \Delta V^6 \quad (\text{D.3})$$

where  $\Delta V$  is the voltage change and  $c_n$  are the calibration constants[115]. The second-order terms and higher are used for the calibration, but not included in the uncertainty propagation. Because an ice-point reference is used, the measured temperature is a summation of the ice-point temperature and the thermocouple temperature.

This propagated uncertainty for calibrated and reference temperatures, including the uncertainty of the slope and intercept as a result of linear regression [116], are:

$$U_{T_{cal}} = \sqrt{U_{T_{ref}}^2 + (U_m T_{ref})^2 + (m U_{T_{ref}})^2} + U_b^2 \quad (D.4)$$

$$U_{T_{ref}} = \sqrt{U_{T_{ice}}^2 + U_{RTD}^2} \quad (D.5)$$

$$U_m = \sqrt{\frac{N (U_{T_{RTD}} - U_{T_{ref}})}{N \sum T_{ref}^2 - (\sum T_{ref})^2}} \quad (D.6)$$

$$U_b = \sqrt{\frac{U_{T_{ref}}^2 \sum T_{ref}^2}{N \sum T_{ref}^2 - (\sum T_{ref})^2}} \quad (D.7)$$

The component uncertainties specified by the equipment manufacturers include  $U_{T_{ice}} = \pm 0.1$  °C and  $U_{T_{RTD}} = \pm 0.15$  °C. The standard deviation of the temperature oscillations in time were added to the error term. The ultimate error of the calibrated thermocouples is found to be  $\pm 0.20$  °C.

In order to calculate the error of the calibrated infrared temperature measurements, the error of the pixel-by-pixel curve fit is first calculated using the error covariance matrix method, as described by Bevington and Robinson [97]. This derivation is based on a temperature calibration curve that is a fourth-order polynomial fit to the DL data:

$$T = p_0 + p_1 S + p_2 S^2 + p_3 S^3 + p_4 S^4 \quad (D.8)$$

where  $T$  is the calibrated temperature,  $S$  is the DL of the infrared signal, and  $p_n$  are the fitting coefficients (fitted to all of the calibration points via least-squares regression). Thus, the uncertainty of the measurement is a propagation of the uncertainty of the signal measurement ( $U_s$ ) and the fitting coefficients ( $U_{p,n}$ ).

$$U_T^2 = \left( \frac{dT}{dS} \right)^2 U_s^2 + \sum_{i=0}^4 \sum_{j=0}^4 \left[ \left( \frac{dT}{dp_i} \frac{dT}{dp_j} \right) U_{p_i} U_{p_j} \right] \quad (D.9)$$

The definition of the error covariance matrix is [97]:

$$\varepsilon = U_{cal}^2 (\mathbf{S}'\mathbf{S})^{-1} = \begin{bmatrix} U_{p_0}^2 & U_{p_0}U_{p_1} & \cdots & U_{p_0}U_{p_4} \\ U_{p_1}U_{p_0} & U_{p_1}^2 & \cdots & U_{p_1}U_{p_4} \\ \vdots & \vdots & \ddots & \vdots \\ U_{p_4}U_{p_0} & U_{p_4}U_{p_1} & \cdots & U_{p_4}^2 \end{bmatrix} \quad (\text{D.10})$$

where  $U_{cal}$  is the uncertainty of the calibration temperature and  $\mathbf{S}$  is the vector of all of calibration temperatures. The variance of the data is given by the uncertainty of the data. The covariance, given by Equation (D.10), defines the variation of two variables that change together (in this case, the calibration temperature and the DL). To calculate the uncertainty term from Equation (D.9), the summation terms on the right are restructured as follows:

$$\sum_{i=0}^4 \sum_{j=0}^4 \left[ \left( \frac{dT}{dp_i} \frac{dT}{dp_j} \right) U_{p_i} U_{p_j} \right] = \varepsilon \cdot (\mathbf{D}\mathbf{D}') \quad (\text{D.11})$$

$$\mathbf{D} = \begin{bmatrix} \frac{dT}{dp_0} \\ \vdots \\ \frac{dT}{dp_4} \end{bmatrix} = \begin{bmatrix} 1 \\ S \\ \vdots \\ S^4 \end{bmatrix} \quad (\text{D.12})$$

where  $U_p$  is the uncertainty of a fitting coefficient and  $\mathbf{D}$  is the vector representing the derivatives of the temperature with respect to each fitting coefficient. The absolute uncertainties of the curve fit temperature are found to be 0.41 °C.

The comparison of the infrared and thermocouple pool temperature measurements are plotted in Figure B.2; a one-to-one correlation is observed with a mean error of 0.26 °C.

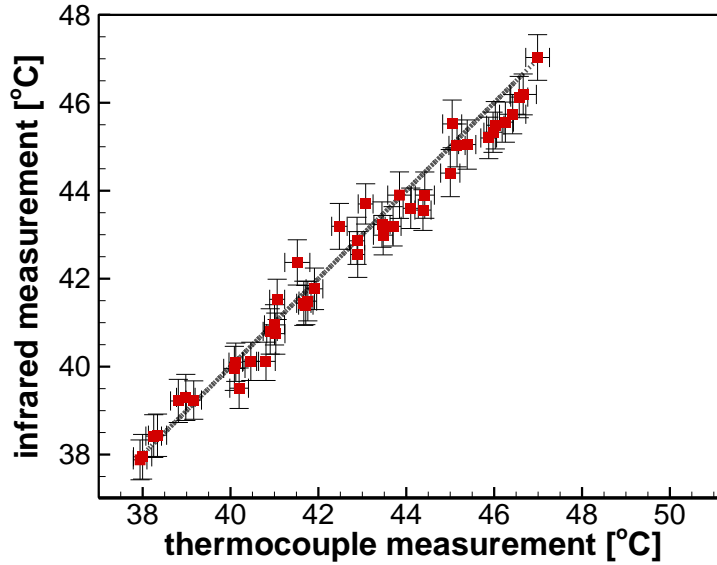


Figure B.2. Comparison of thermocouple and infrared temperature measurements plotted with a one-to-one correlation line. The horizontal and vertical error bars represent the calibrated thermocouple measurement error and the calibrated infrared measurement error, respectively.

## B.2 Infrared Measurement Correction

In order to improve the accuracy of the infrared temperature measurements, it is necessary to correct for errors caused by background radiation and nonuniform emissivity of the surface. This is done by incorporating the geometry of the droplet to find the surface normal vector. If the droplet is assumed to be a spherical cap, every position on the droplet surface can be depicted as follows:

$$F(r, \theta) = r - R - b \cos \theta \quad (\text{D.13})$$

$$b = h - R \quad (\text{D.14})$$

where  $F$  is the shape function of the droplet,  $r$  is the radial position from the bottom center of the droplet,  $R$  is the contact radius of the droplet ( $D/2$ ),  $b$  is a droplet parameter,  $h$  is the height of the droplet, and  $\theta$  is the polar angle.

The emissivity ( $\varepsilon$ ) and reflectivity ( $\rho$ ) of water are calculated based on the index of refraction ( $n$ ) and absorption coefficient ( $k$ ) data presented by Irvine and Pollack [34]. Since the camera and lens capture at a wavelength band of 1.5 to 5.1  $\mu\text{m}$ , we approximate the measurement based on the emission peak at 3  $\mu\text{m}$  [34]. The Fresnel equations can be used to calculate the reflectivity and

emissivity of the droplet surface as a function of incident angle [117]. This is a crucial step towards mapping the emissivity of a curved interface, such as a droplet, because the properties change as a function of location. The parallel and perpendicular reflectivities can be calculated using the following [117]:

$$\rho_{\perp} = \frac{(n_1 \cos \psi - u)^2 + v^2}{(n_1 \cos \psi + u)^2 + v^2} \quad (\text{D.15})$$

$$\rho_{\parallel} = \frac{\left( (n_2^2 - k_2^2) \cos \psi - n_1 u \right)^2 + (2n_2 k_2 \cos \psi - n_1 v)^2}{\left( (n_2^2 - k_2^2) \cos \psi + n_1 u \right)^2 + (2n_2 k_2 \cos \psi + n_1 v)^2} \quad (\text{D.16})$$

$$u^2 = \frac{1}{2} (n_2^2 - k_2^2 - n_1^2 \sin^2 \psi) + \frac{1}{2} \sqrt{(n_2^2 - k_2^2 - n_1^2 \sin^2 \psi)^2 + 4n_2^2 k_2^2} \quad (\text{D.17})$$

$$v^2 = -\frac{1}{2} (n_2^2 - k_2^2 - n_1^2 \sin^2 \psi) + \frac{1}{2} \sqrt{(n_2^2 - k_2^2 - n_1^2 \sin^2 \psi)^2 + 4n_2^2 k_2^2} \quad (\text{D.18})$$

$$\psi = \cos^{-1} \left\{ \frac{\cos^{-1}(r + b \cos \theta)}{\sin \theta \cos \varphi \sqrt{r^2 + b^2 \sin^2 \theta}} \right\} \quad (\text{D.19})$$

where  $\theta$  and  $\varphi$  are the polar and azimuthal angles from the center of the droplet contact area, and  $\psi$  is the angle between the surface normal and the camera image plane vector. The result of this calculation for water is shown in Figure B.3(a). For the purposes of this study, the surface reflection,  $\rho_s$ , is assumed to be unpolarized (*i.e.*, the average of the parallel and perpendicular polarization). The reflectivity drastically increases for oblique incident angles. To apply the properties to a droplet, the incident angle as a function of position on the droplet interface is calculated and used to calculate reflectivity at those positions, as shown in Figure B.3(b). The incident radiation is assumed to be from the shield (at 20 °C) for the top half of the droplet and from the substrate (at the set point temperature) for the bottom half of the droplet. The temperature is corrected using the local surface reflectivity as follows:

$$\rho_s = 1 - \varepsilon_s \quad (\text{D.20})$$

$$0.97 \sigma T_{uncorr}^4 = \varepsilon_s \sigma T_{corr}^4 + \rho_s \varepsilon_{bg} \sigma T_{bg}^4 \quad (\text{D.21})$$

where  $\varepsilon_s$  is the local emissivity,  $\sigma$  is the Stefan-Boltzmann constant,  $T_{uncorr}$  is the uncorrected temperature,  $T_{corr}$  is the corrected temperature,  $\varepsilon_s$  is the surface emissivity,  $\varepsilon_{bg}$  is the background source emissivity, and  $T_{bg}$  is the background temperature.

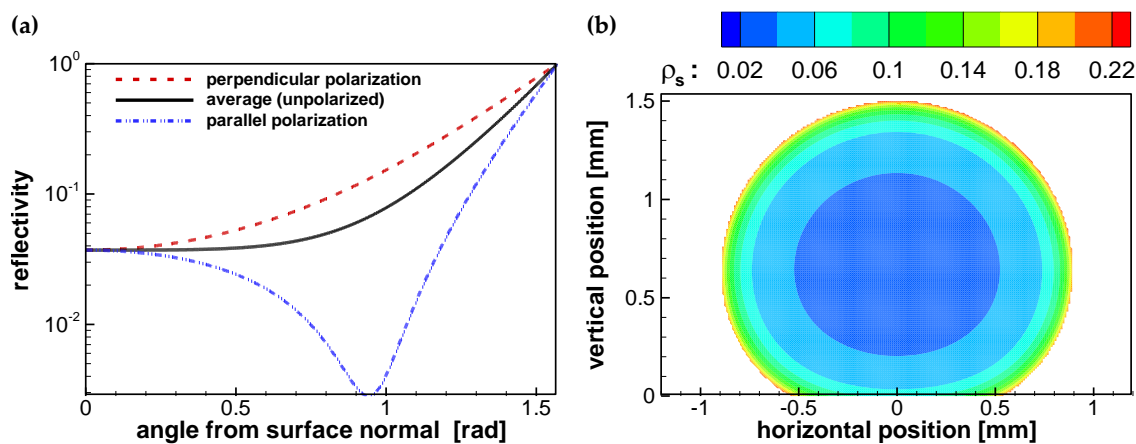


Figure B.3. The reflectivity plotted (a) as a function of the angle from the surface normal, and (b) as a function of position on the surface of an example droplet (at a volume of  $2.5 \mu\text{L}$ ).

### B.3 Temperature Data after Correcting for Background Reflections

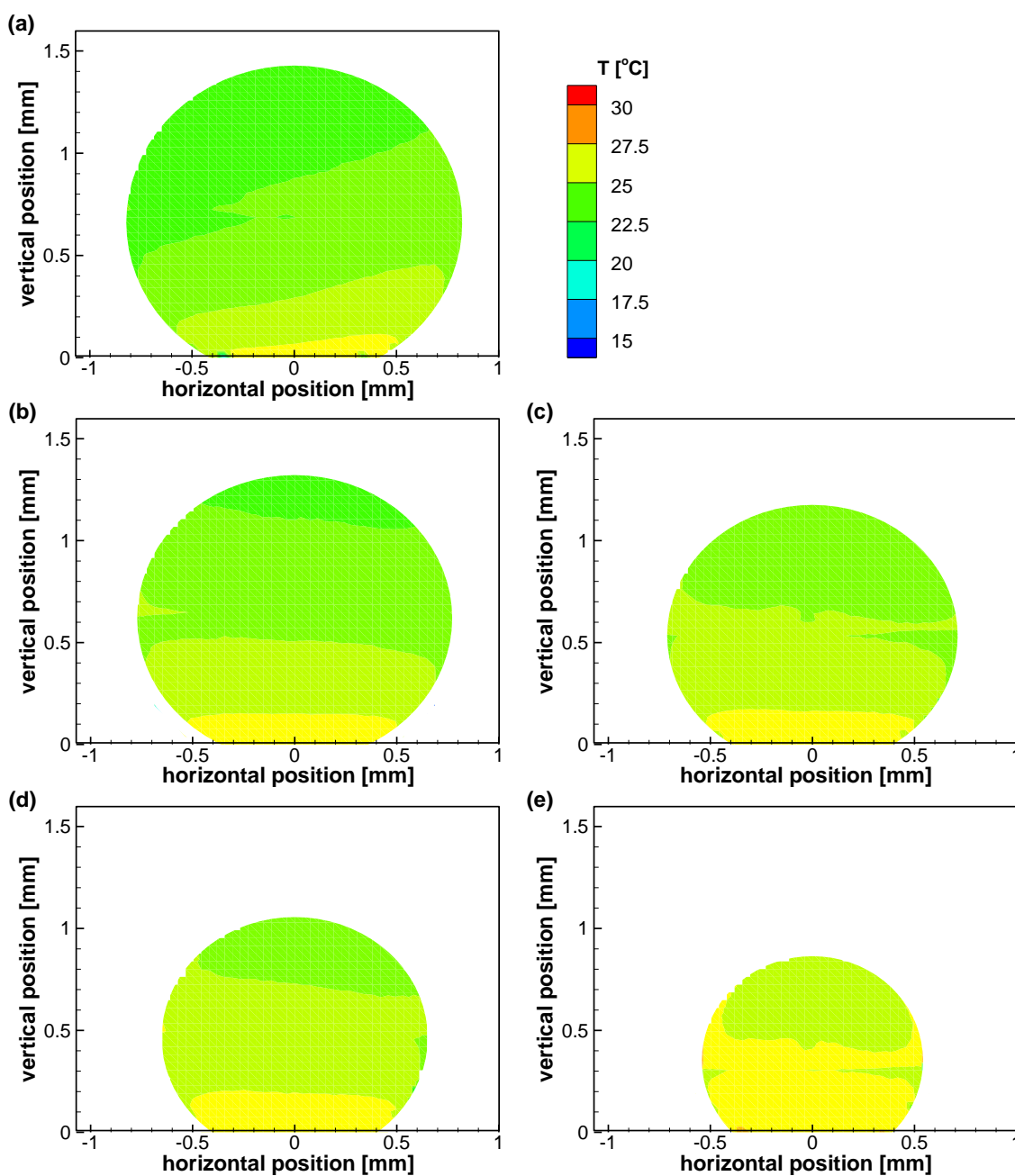


Figure B.4. Temperature data after correcting for background reflections for a substrate temperature of  $30^{\circ}\text{C}$  for droplet volumes of (a)  $3.0\ \mu\text{L}$ , (b)  $2.5\ \mu\text{L}$ , (c)  $2.0\ \mu\text{L}$ , (d)  $1.5\ \mu\text{L}$ , and (e)  $1.0\ \mu\text{L}$ .

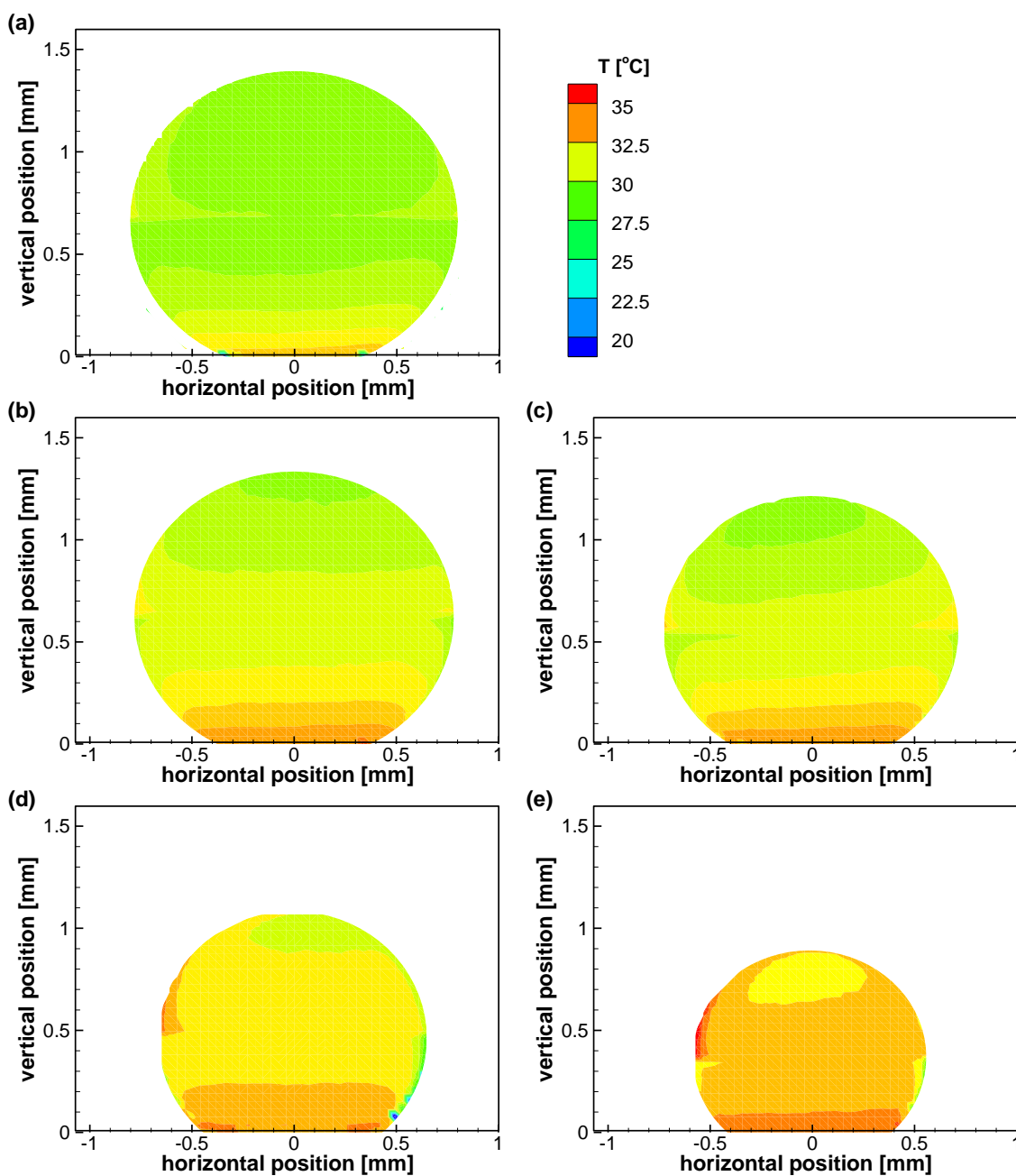


Figure B.5. Temperature data after correcting for background reflections for a substrate temperature of  $40^\circ\text{C}$  for droplet volumes of (a)  $3.0 \mu\text{L}$ , (b)  $2.5 \mu\text{L}$ , (c)  $2.0 \mu\text{L}$ , (d)  $1.5 \mu\text{L}$ , and (e)  $1.0 \mu\text{L}$ .

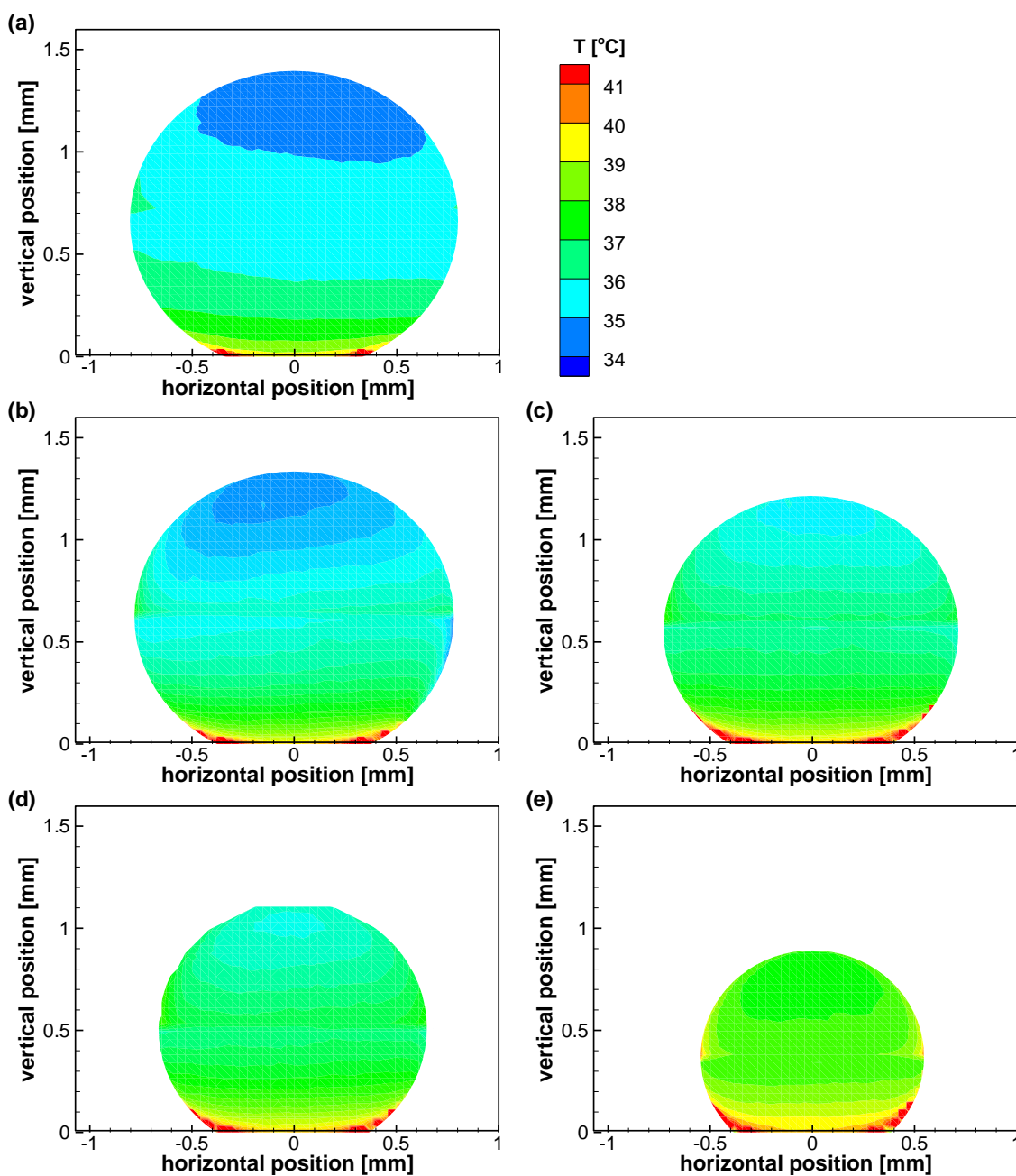


Figure B.6. Temperature data after correcting for background reflections for a substrate temperature of 50°C for droplet volumes of (a) 3.0  $\mu\text{L}$ , (b) 2.5  $\mu\text{L}$ , (c) 2.0  $\mu\text{L}$ , (d) 1.5  $\mu\text{L}$ , and (e) 1.0  $\mu\text{L}$ .

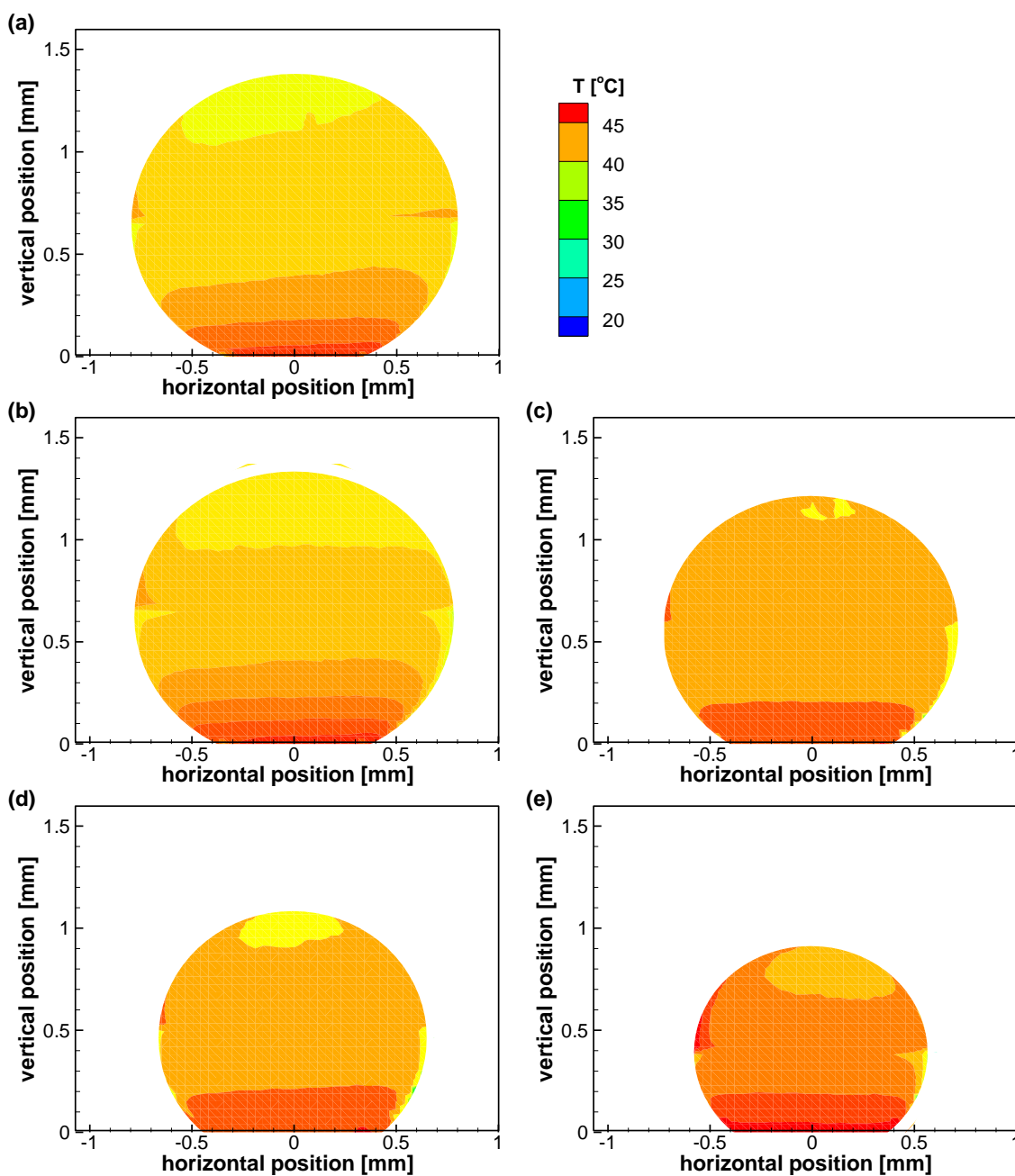


Figure B.7. Temperature data after correcting for background reflections for a substrate temperature of  $60^{\circ}\text{C}$  for droplet volumes of (a)  $3.0\ \mu\text{L}$ , (b)  $2.5\ \mu\text{L}$ , (c)  $2.0\ \mu\text{L}$ , (d)  $1.5\ \mu\text{L}$ , and (e)  $1.0\ \mu\text{L}$ .

#### B.4 Evaporation Rate Prediction

The evaporation rate of a droplet can be predicted using the interface temperature distribution and an assumed mode of species transport in the vapor-gas domain. In this section, the infrared

interface temperature measurements are directly utilized to predict evaporation rates for the purpose of comparison to the experimental results. Two different prediction approaches are explored: purely vapor-diffusion-based and purely convection-based techniques.

One common assumption for analytical solutions is that vapor species transport is governed by diffusion [44]. The evaporation flux at the interface is given as a function of the radial position from the droplet centerline.

$$J_{diff}(r) = \frac{D[c_s(T_s) - \phi c_a(T_a)]}{R_c} j(\theta) \quad (\text{D.22})$$

where  $J_{diff}(r)$  is the diffusive mass flux,  $D$  is the diffusion coefficient,  $c$  is the saturation vapor concentration,  $T$  is the temperature,  $\phi$  is the relative humidity,  $R_c$  is the droplet contact radius, and  $\theta$  is the droplet contact angle. The subscript  $s$  represents the local interface conditions and the subscript  $a$  represents the ambient conditions. The function  $j(\theta)$  is defined as follows:

$$j(\theta) = \left[ \frac{1}{2} \sin \theta + \sqrt{2} (\cosh \alpha + \cos \theta)^{3/2} \times \int_0^\infty \frac{\cosh \theta \tau}{\cosh \pi \tau} \tan [(\pi - \theta) \tau] \times P_{-(1/2)+i\tau}(\cosh \alpha) \tau d\tau \right] \quad (\text{D.23})$$

$$\cosh \alpha = \frac{\sin \theta}{(h/R)} - \cos \theta \quad (\text{D.24})$$

where  $\alpha$  is toroidal coordinate variable,  $\tau$  is time, and  $P$  is the Legendre function of the first kind. The interface temperature conditions in Equation (D.22) are set as the measured infrared temperature profile along the vertical droplet surface centerline. Examples of vertical temperature profiles are shown in Figure B.8. The evaporation flux profile is integrated over the surface area of the droplet to calculate the evaporation rate. The evaporation rate predictions of this species-diffusion-based prediction are plotted against the experiments in Figure S10.

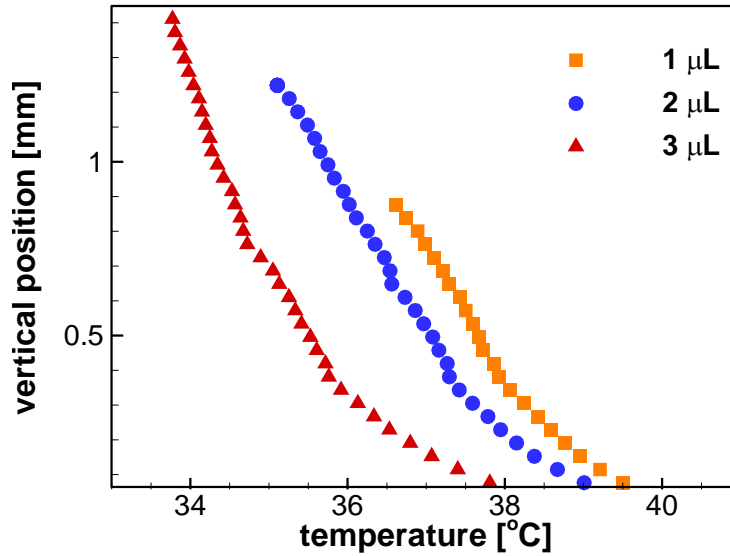


Figure B.8. Vertical infrared temperature profiles along droplet centerline during the evaporation process at 1  $\mu\text{L}$ , 2  $\mu\text{L}$ , and 3  $\mu\text{L}$  for a substrate temperature of 50°C (not corrected for reflection from the background as shown).

Convection is an alternative mechanism of species transport from the droplet interface that is considered. A simplified species-convection-based evaporation prediction is developed using a correlation by Ranz and Marshall [118] for natural convection around a droplet

$$\text{Nu} = 2.0 + 0.61 \text{Pr}^{1/3} \text{Gr}^{1/4} \quad (\text{D.25})$$

where Nu is the Nusselt number, Pr is the Prandtl number, and Gr is the Grashof number, which are defined as follows:

$$\text{Nu} = \frac{hL}{k} \quad (\text{D.26})$$

$$\text{Pr} = \frac{\nu}{\alpha} \quad (\text{D.27})$$

$$\text{Gr} = \frac{g \beta (T_s - T_a) L^3}{\nu^2} \quad (\text{D.28})$$

where  $h$  is the convective heat transfer coefficient,  $L$  is the length scale,  $k$  is the thermal conductivity of the air,  $\nu$  is the kinematic viscosity of the air,  $\alpha$  is the thermal diffusivity of the air,  $g$  is the gravitational acceleration,  $\beta$  is the coefficient of thermal expansion of the air,  $T_s$  is the

interface temperature, and  $T_a$  is the ambient temperature. The heat and mass transfer analogy [119] is utilized to calculate the mass transfer coefficient. The evaporative flux can then be calculated using the following formulation.

$$J_{con}(r) = h_m (c_s(T_s) - \varphi c_a(T_a)) \quad (\text{D.29})$$

where  $J_{con}$  is the convection mass flux,  $h_m$  is the mass transfer coefficient,  $c_s$  is the interface vapor concentration,  $\varphi$  is the relative humidity, and  $c_a$  is the ambient concentration. The local mass flux is again integrated over the droplet surface to calculate the evaporation rate using the experimental interface temperature data; the species-convection-based evaporation rate predictions are compared to the experiments in Figure B.9.

As can be seen in Figure B.9, the convection-based prediction is closer to the actual evaporation rate than the vapor-diffusion prediction. The interface-temperature-adjusted vapor-diffusion prediction consistently underpredicts the evaporation rate, with errors from 18% to 30% (increasing with substrate temperature) over all test cases. Conversely, the interface-temperature-dependent convection prediction has an average underprediction of 7.3%. The under-predictions of both approaches indicate that a coupled convection–diffusion prediction is required; however, for the purposes of comparison, these results show that the air-side natural convection contributes to evaporation to a larger extent than vapor diffusion.

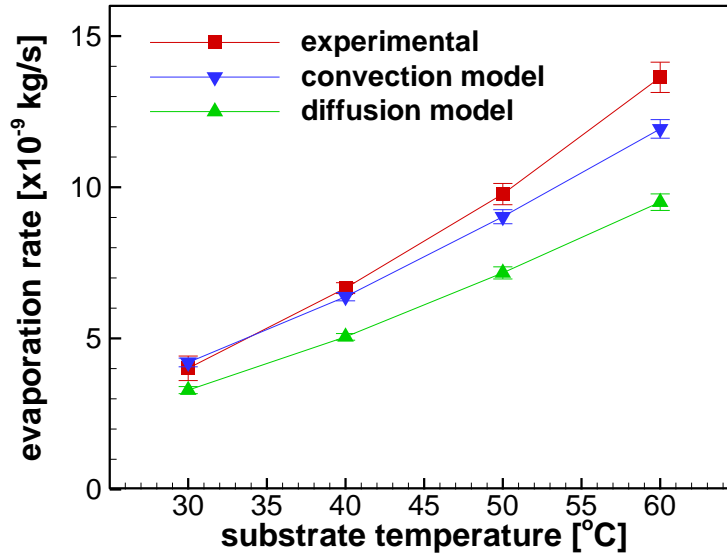


Figure B.9. The evaporation rates from the experiments, vapor-diffusion-based predictions, and natural-convection-based predictions for a droplet volume of 2.5  $\mu\text{L}$ . The error bars represent the standard deviation for all trials at that substrate temperature.

## B.5 Infrared Reflection Correction Code

This code corrects for reflection errors in infrared measurements of droplet interfaces. It assumes that the droplet is water in a spherical cap configuration.

```
%% Description
% This code corrects for reflection errors in infrared measurements of
% droplet interfaces. It assumes that the droplet is water in a spherical
% cap configuration.
% Iteration:
% 1: just view the droplet. Use this to ascertain the left and right
% contact points of the droplet as well as the top and the bottom.
% 2: enter the values that you got from 1 into the prompt for the analysis.
% By: Aditya Chandramohan, August 2016

%% prompt for user input

prompt = {'filename: '... % filename
         'Iteration? (> 2 means fill below): ',... % 1 is for initial read, 2 is
         % for correcting the data
         'Left x: '... % left contact line x [pix]
         'Right x: '... % right contact line x [pix]
         'Bottom y: '... % bottom of droplet y [pix]
         'Top y: '}; % apex of droplet y [pix]
dlg_title = 'Data Analysis';
```

```

num_lines = 1;

%% default entries
def = {'test1.mat'...
      '1',...
      '155',...
      '183',...
      '123',...
      '166'};
answer = inputdlg(prompt,dlg_title,num_lines,def);

%% Enter Data
filename = answer{1};
reading = str2num(answer{2}); %#ok<*ST2NM>
x_left = str2num(answer{3});
x_right = str2num(answer{4});
y_bottom = str2num(answer{5});
y_top = str2num(answer{6});
T_sub = 30; % substrate temperature
T_atm = 20; % ambient temperature
lowT = 30; % top temperature of color map
highT = 40; % lowest temperature of color map
timestep = 400; % specific data point

clearvars answer

%% Load Data
A = load(filename);
disp(size(A.Temp,3));
Temperature = A.Temp(:,:,timestep);

%% Selecting Modes
% 1 is viewing mode, 2 is correction mode after selecting viewing
% parameter.

switch reading
case 1 % plotting uncorrected data
figure('units','normalized','outerposition',[0 0 1 1])
pcolor(Temperature) % mean taken across the 3rd
                    % dimension (mean of each
                    % pixels across all frames at
                    % one temperature)
                    % formatting figure for view
shading flat
colormap(jet)
axis equal
axis tight
colorbar('vert','fontsize',20)
caxis([lowT highT])
set(gca,'fontsize',20)
xlabel('Position (mm)','fontsize',20)
ylabel('Position (mm)','fontsize',20)
otherwise % correcting and plotting
% Plot uncorrected temperature
figure (1000)
pcolor(Temperature((x_left-5):x_right+5,(y_bottom-5):(y_top+5)))
                    % mean taken across the 3rd

```

```

% dimension (mean of each
% pixels across all frames at
% one temperature)
% formatting for view

shading flat
colormap(jet)
axis equal
axis tight
colorbar('vert','fontsize',20)
caxis([lowT highT])
set(gca,'fontsize',20)
xlabel('Position (mm)','fontsize',20)
ylabel('Position (mm)','fontsize',20)

% Droplet parameters
center_x = round((x_right+x_left)/2); % center of droplet (x)
center_y = y_bottom; % bottom of droplet (y)
R = (x_right-x_left)/2; % contact radius of droplet
h = y_top-y_bottom; % height of droplet
b = h-R; % spherical cap param.

% the following correction code assumes the use of the FLIR SC7650
% with a 320x256 pixel resolution.
% The parameters of the droplet shape are calculated based on the
% spherical cap assumption.
[x,y] = meshgrid(1:320,1:256); % create mesh
x = x-center_x; % shift axis to center around droplet contact area.
y = y-center_y; % see above
r = (R + sqrt(R+4*b*y))/2; % calculate radial position from origin
z = sqrt(r.^2 - x.^2-y.^2); % out-of-plane position.
thet = acos(y./r); % spherical coordinates
phi = atan(x./z);
magF = sqrt(r.^2+b^2*sin(thet).^2)./r; % magnitude of F vector
Nu = sqrt(x.^2+y.^2);
Ni =
(1./magF).*sin(thet).*sin(phi)+b*sin(thet).*cos(thet).*sin(phi)./r);
Nj = (1./magF).*cos(thet)-b*sin(thet).^2./r);
Nk =
(1./magF).*sin(thet).*cos(phi)+b*sin(thet).*cos(thet).*cos(phi)./r);

% removes all data outside of this radial position
radial_threshold = 0.9;
Ni(Nu/R > radial_threshold*(1+(b/R)*(y./Nu))) = 0;
Nj(Nu/R > radial_threshold*(1+(b/R)*(y./Nu))) = 0;
Nk(Nu/R > radial_threshold*(1+(b/R)*(y./Nu))) = 0;
z (Nu/R > radial_threshold*(1+(b/R)*(y./Nu))) = 0;

psi =
acos((r+b*cos(thet))./sqrt(r.^2+b^2*sin(thet).^2).*sin(thet).*cos(phi));
psi(Nu/R > (1+(b/R)*(y./Nu))) = 0;

n2 = 1.371; % water refraction properties
k2 = 0.272;
n1 = 1; % air refraction properties
k1 = 0;

% Fresnel Equations

```

```

u2 = (n2^2-k2^2-n1^2*sin(psi).^2)/2+...
sqrt((n2^2-k2^2-n1^2*sin(psi).^2).^2+4*n2^2*k2^2)/2;

v2 = -(n2^2-k2^2-n1^2*sin(psi).^2)/2+...
sqrt((n2^2-k2^2-n1^2*sin(psi).^2).^2+4*n2^2*k2^2)/2;

% perpendicular polarized reflection
rho_per = ((n1*cos(psi)-sqrt(u2)).^2+v2)./...
((n1*cos(psi)+sqrt(u2)).^2+v2);

% parallel polarized reflection
rho_par = (((n2^2-k2^2)*cos(psi)-n1*sqrt(u2)).^2+(2*n2*k2*cos(psi)-
n1*sqrt(v2)).^2)./...
(((n2^2-
k2^2)*cos(psi)+n1*sqrt(u2)).^2+(2*n2*k2*cos(psi)+n1*sqrt(v2)).^2);

% get average and get the real component
rho_av = (rho_per+rho_par)/2;
rho_av(Nu/R > (1+(b/R)*(y./Nu))) = 0;
rho_av = real(rho_av);

% Final Calculations
eps = 1-rho_av; % emissivity
T = mean(Temperature,3)+273.15; % temperature plot

% corrected temperature
T_corr = ((0.97*(T.^4)-rho_av*0.8*(T_sub+273.15)^4)./eps).^0.25;
T_top = ((0.97*(T.^4)-rho_av*(T_atm+273.15)^4)./eps).^0.25;
T_corr(Nj>=0) = T_top(Nj>=0);
T_corr = real(T_corr)-273.15;
T_corr(Nu/R > radial_threshold*(1+(b/R)*(y./Nu))) = 0;

%% Uncorrected Figure
figure(1001)
T = T - 273.15;
T(Nu/R > radial_threshold*(1+(b/R)*(y./Nu))) = 0;
T(y<0)=0;
pcolor(T) % mean taken across the 3rd dimension (mean of each
% pixels across all frames at one temperature)
shading flat
colormap(jet)
axis equal
axis tight
colorbar('vert','fontsize',20)
caxis([lowT highT])
set(gca,'fontsize',20)
xlabel('Position (mm)','fontsize',20)
ylabel('Position (mm)','fontsize',20)

figure(1002)
scatter(y(:,160)+y_bottom,T(:,(center_x-2)), 'k')
hold on;
scatter(y(:,161)+y_bottom,T(:,(center_x-1)), 'k')
scatter(y(:,162)+y_bottom,T(:,(center_x-0)), 'k')
scatter(y(:,163)+y_bottom,T(:,(center_x+1)), 'k')

```

```

scatter(y(:,163)+y_bottom,T(:, (center_x+2)), 'k')
axis([y_bottom y_top 0 highT])

%% Corrected Figure
figure(1001)
T_corr(y<0)=0;
pcolor(T_corr) % mean taken across the 3rd dimension (mean of
               % each pixels across all frames at one temperature)

shading flat
colormap(jet)
axis equal
axis tight
colorbar('vert','fontsize',20)
caxis([lowT highT])
set(gca,'fontsize',20)
xlabel('Position (mm)','fontsize',20)
ylabel('Position (mm)','fontsize',20)

%% Scatter Plot of Positions
figure(1003)
scatter(y(:,160)+y_bottom,T_corr(:, (center_x-2)), 'k')
hold on;
scatter(y(:,161)+y_bottom,T_corr(:, (center_x-1)), 'k')
scatter(y(:,162)+y_bottom,T_corr(:, (center_x-0)), 'k')
scatter(y(:,163)+y_bottom,T_corr(:, (center_x+1)), 'k')
scatter(y(:,163)+y_bottom,T_corr(:, (center_x+2)), 'k')
axis([y_bottom y_top 0 highT])

end

```

## APPENDIX C. MARANGONI CONVECTION IN EVAPORATING ORGANIC LIQUID DROPLETS ON A NONWETTING SUBSTRATE

### C.1 Dependence of Velocity Field on Droplet Volume

The measured velocities inside the droplet show no discernable trend with droplet volume, within the range of volumes tested, as shown in Figure S1. At a given substrate temperature, the differences in the measured maximum velocities are either negligible for a change in volume, as in Figure C.1(a) and (d), or there is a small variation without any monotonic correlation, as in Figure C.1(b) and (c).

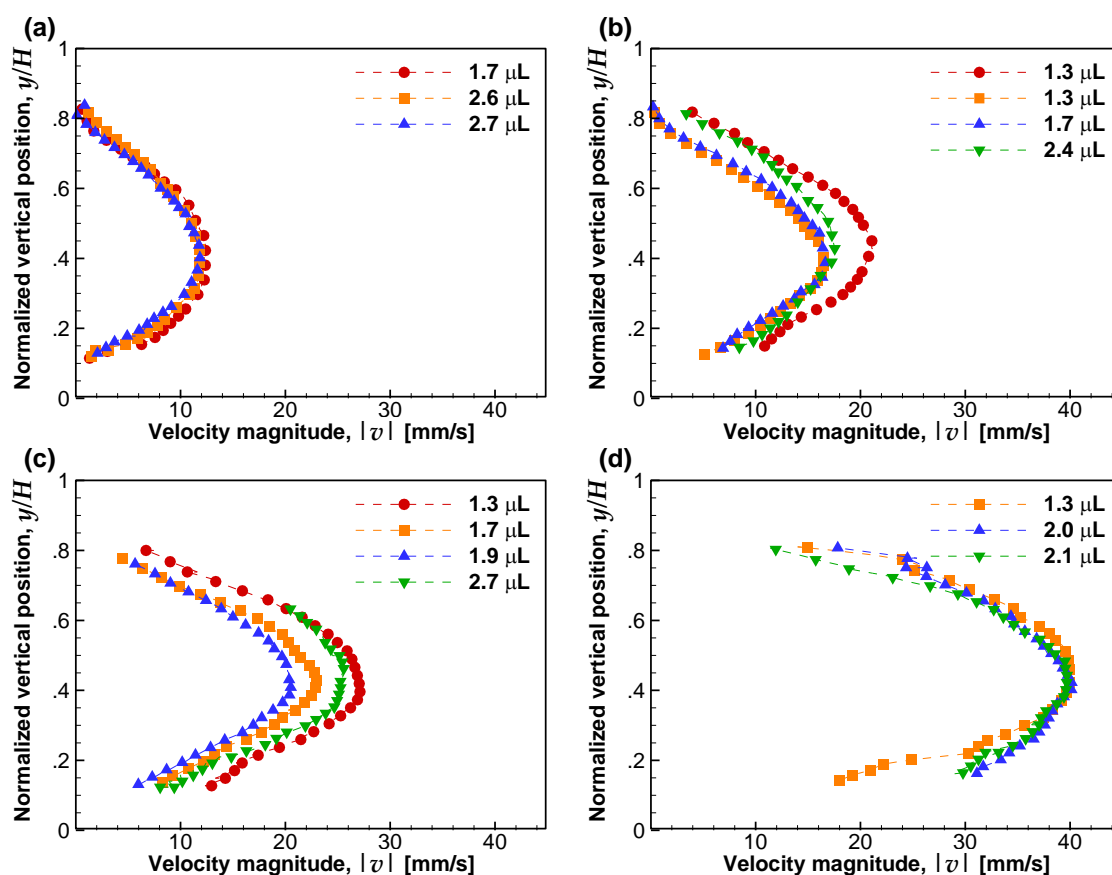


Figure C.1. The centerline vertical velocity profile is shown at multiple volumes for substrate temperatures of: (a) 5 °C, (b) 10 °C, (c) 15 °C, and (d) room temperature.

## C.2 Marangoni Number Scaling

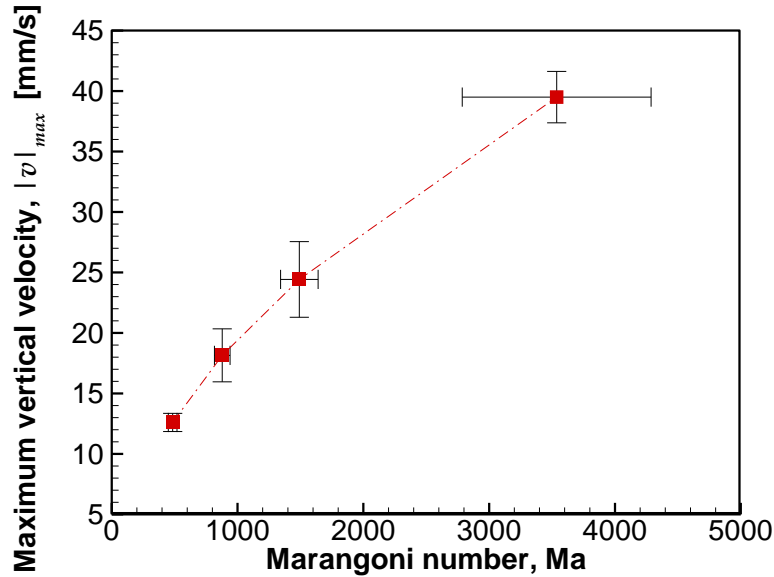


Figure C.2. Relationship between the Marangoni number and maximum velocity. The error bars represent standard deviations over all four tests at each substrate temperature (5 °C, 10 °C, 15 °C, and room temperature).

## C.3 Estimation of the Droplet Interface Velocity

A comparison between the velocity data and the Marangoni velocity scale is only possible for near-interface velocities. It is necessary to estimate the interface velocity, which is masked by the curvature of the droplet, from the available data and flow field pattern. Assuming that the system is in a quasi-static state, it is possible to calculate the recirculating mass flow rate in the droplet based on the downward flow passing through a horizontal circular cross-section of the droplet. In particular, all downward velocity data are available at a horizontal cross-section passing through the vortex center. The upward flow velocities in the peripheral regions can then be estimated via mass conservation. At the same horizontal cross-section, it is known that the upward velocity is zero at the vortex center; it is assumed that the velocity increases linearly in the radial direction, as pictured in Figure C.3. From this assumed upward profile, the velocity at the interface can be estimated based on the total recirculating mass flow rate, and compared to the scaled velocity.

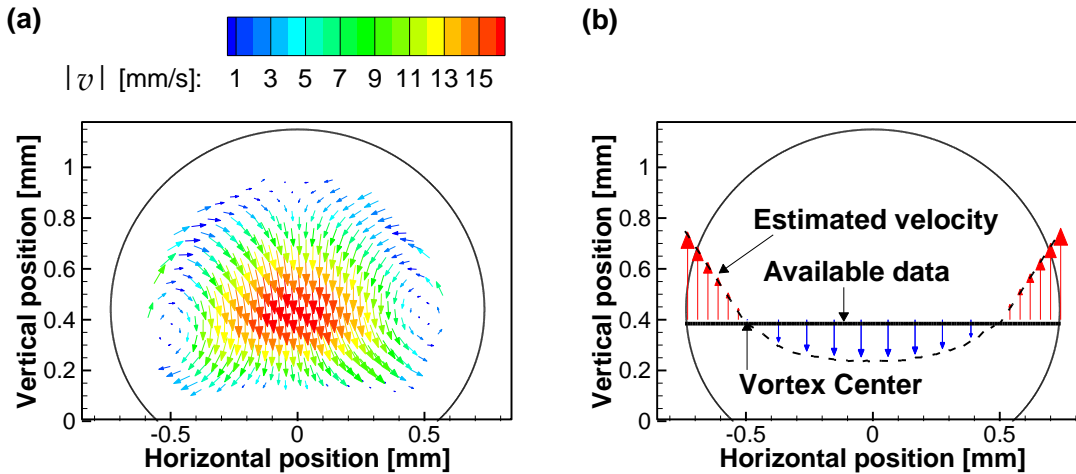


Figure C.3. (a) An example experimental velocity field (at a substrate temperature of 10 °C and droplet volume of 1.34  $\mu\text{L}$ ) is shown to illustrate the estimation of the near-interface upward velocity in the droplet. (b) The vertical velocity vectors are plotted at a horizontal plane of the droplet passing through the vortex center; the upward velocities in the outer region (depicted in red) are estimated based on conserving the mass flow rate from the available experimental data (depicted in blue).

#### C.4 Reduced-Order Model Description

Popov[44] derived an exact, closed-form solution for the evaporation of a sessile droplet via a vapor-diffusion model. The model assumed that the droplet and liquid-vapor interface are at a uniform temperature equal to the substrate temperature. For a given interface temperature, the vapor concentration at the droplet interface was assumed to be the value calculated at the saturated vapor pressure. The Laplace equation for diffusion in the concentration field was solved to analytically model quasi-static evaporation in the toroidal domain. The interfacial evaporation flux with radial position from the center line,  $J(r)$ , was defined as [31,44]

$$J(r) = \frac{D[c_s(T_s) - \varphi c_a(T_a)]}{R_c} j(\theta) \quad (\text{D.1})$$

where  $D$  is the diffusion coefficient,  $c_s$  is the saturation concentration of the vapor,  $T_s$  is the substrate temperature,  $\varphi$  is the ambient relative humidity (of the droplet fluid),  $c_a$  is the saturation

concentration at the ambient temperature,  $T_a$  is the ambient temperature,  $R_c$  is the contact radius of the droplet,  $\theta$  is the contact angle of the droplet, and  $j(\theta)$  was defined as:

$$j(\theta) = \left[ \frac{1}{2} \sin \theta + \sqrt{2} (\cosh \alpha + \cos \theta)^{3/2} \times \int_0^{\infty} \frac{\cosh \theta \tau}{\cosh \pi \tau} \tan [(\pi - \theta) \tau] \times P_{-(1/2)+i\tau}(\cosh \alpha) \tau d\tau \right] \quad (\text{D.2})$$

Dash and Garimella[71] modified this model for evaporation of water droplets on superhydrophobic surfaces, where evaporative cooling significantly depresses the temperature of the interface due to the large thermal resistance of the droplet (due to its large height-to-diameter aspect ratio). This model incorporated one-dimensional thermal conduction along the vertical axis of the droplet to account for this effect, and predicted the interface temperature along the height of the droplet. Thus, the local evaporative flux was a function of the local interface temperature.

In the current study, a model is developed for the evaporation of organic liquid droplets on nonwetting surfaces that incorporates advective transport. The model estimates the recirculating mass flowrate in the droplet based on the Marangoni velocity, and assumes a simplified convective recirculation pattern for which coupled advection and diffusion transport is incorporated. For prediction of the temperature profile of the droplet during evaporation, the droplet is divided into several different regions based on the recirculating flow pattern observed in the experiments. Advective transport is considered in a central core of the droplet where the flow is downward and an outer peripheral region where the flow is upward, based on the mass conservation displayed in Figure C.3(b). These regions are coupled at the top and bottom of the droplet by diffusion-dominated regions, where one-dimensional conduction is assumed in the vertical direction as in the conduction-only model of Dash and Garimella [71]. The model also incorporates convective heat transfer between the droplet and the ambient air. To predict a temperature drop across the height of the droplet, the substrate temperature is fixed and evaporative cooling at the interface is predicted for vapor-species diffusion to the ambient [44,71]. At the liquid-vapor interface, the boundary condition is a combination of evaporative cooling and convective transport to the ambient.

A few additional assumptions are necessary to simplify the transport model. It is assumed that the upward and downward flow regions do not interact (except at the top and bottom of the droplet to maintain mass continuity). The time scale of diffusion-limited evaporative mass transfer at the

liquid-vapor interface[44],  $t_D$ , is on the order of  $10^{-10}$  s, while the time scale of advection,  $t_A$ , is at most 0.026 s for methanol ( $t_A=H/v$ , where  $H$  is the droplet height and  $v$  is the maximum vertical velocity for the room temperature case). Because of the drastic difference between the time scales of vapor transport and advection, the system can be assumed to be quasi-static (*i.e.*, evaporative mass loss is neglected) in order to simplify overall mass continuity. Since it is observed that the flow velocity magnitudes are largest in the vertical direction at the height of the vortex center within the droplet core, the system mass flowrate is calculated based on the total vertical flow across this plane. Advection due to mass flow in the vertical direction is considered in the central core and outer periphery domains. In the conduction-dominated regions, the vertical velocity is close to zero; the horizontal velocities in this region traverse isotherms and, thus, do not contribute to the advective transport. Based on experimental evidence, this conduction-dominated region is found to be 10% of the droplet height at both the top and bottom of the droplet.

Per the simplified flow field and transport mechanisms assumed, the regions of the droplet used to construct the model are shown in Figure C.4. The conduction-dominated region is discretized into a series of disk-shaped control volumes spanning the diameter of the droplet, as displayed in Figure C.4(b). The energy balance in each control volume may be characterized with the following governing equation:

$$-kA_{bot} \left. \frac{dT}{dz} \right|_{bot} = -kA_{top} \left. \frac{dT}{dz} \right|_{top} + J(r) h_{fg} dS + h(T - T_{amb}) dS \quad (D.3)$$

where  $k$  is the liquid thermal conductivity,  $A_{bot}$  and  $A_{top}$  are the bottom and top areas,  $J(r)$  is the local evaporative flux,  $h_{fg}$  is the latent heat of evaporation,  $h$  is the convective heat transfer coefficient,  $T$  is the temperature of the current volume,  $T_{amb}$  is the ambient temperature, and  $dS$  is the infinitesimal liquid-air interface of the control volume. Note that the temperature inside each control volume is assumed to be uniform.

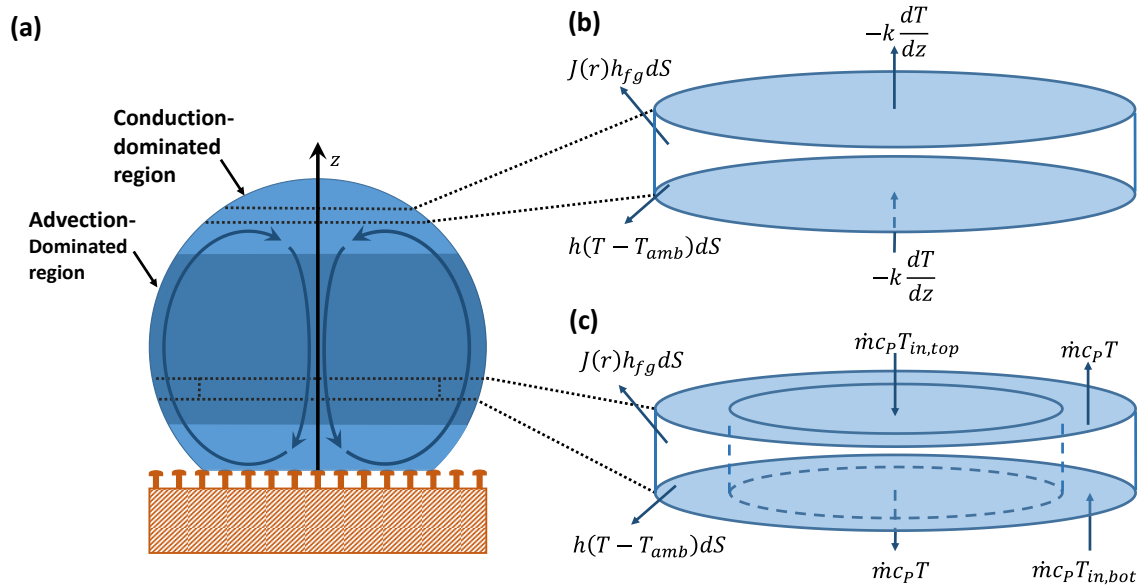


Figure C.4. (a) Schematic diagram of the evaporating droplet on a substrate with recirculating flow. The conduction-dominated and advection-dominated regions of the droplet are shown in lighter and darker shades, respectively. Representative discretized control volumes for the (b) conduction-dominated and (c) advection-dominated regions of the droplet are also shown.

In the advection-dominated region, thermal diffusion is ignored. Due to the recirculating flow, this region incorporates a cylindrical domain in the core of the droplet where the flow is downwards, and a surrounding annular domain where the flow is upwards along the interface. The discretized disk-shaped control volumes for this region are illustrated in Figure C.4(c). Energy transport in the outer annular region may be defined as follows:

$$\dot{m} c_p T_{bot} = \dot{m} c_p T + J(r) h_{fg} dS + h(T - T_{amb}) dS \quad (\text{D.4})$$

where  $\dot{m}$  is the mass flowrate,  $c_p$  is the liquid specific heat capacity,  $T_{bot}$  is the temperature from the control volume below the current one. The inner cylindrical domain uses the same equation, excluding the evaporative and convective terms on the right hand side.

The fluid properties are allowed to vary with temperature. The convective heat transfer coefficient is calculated using a Nusselt number of 2, which represents stagnant air [118,120,121]. Due to the sub-ambient temperature substrate, the convective heat transfer adds heat to the droplet. The recirculating mass flowrate is calculated using the Marangoni velocity as the interface velocity

assuming the same velocity profile as described in the previous section on estimation of the droplet interface velocity. Since the temperature drop across the droplet height is not known *a priori*, the Marangoni velocity is initialized using the temperature drop estimated via a conduction-only model [71]. The velocity is iterated with the temperature drop calculated using the model developed herein that includes advection.

The model is implemented in an in-house MATLAB [98] code that uses a finite volume method with a first-order upwinding scheme for advective transport and first-order forward differencing for conductive transport. The energy equations are solved by iterating and updating all thermophysical properties after each iteration. Solution convergence is achieved when the control volume temperatures remain constant (within a pre-defined threshold of  $10^{-7}$  °C).

### C.5 Advection-Driven Droplet Evaporation Code

This code modes advection-driven energy transport within a methanol droplet to estimate the vertical temperature profile and the global evaporation rate of the droplet.

```
clear all; close all; clc;
%% Description
% This code conducted advection-driven energy transfer within a methanol
% droplet to estimate the vertical temperature profile and the global
% evaporation rate of the droplet.
% By: Aditya Chandramohan (March 2016)

%% Important Notes:
% For the temperature array:
% Column 1 is the exterior annulus
% Column 2 is the interior disk

%% Reading the functional dependence of CA and angular position on Flux;
TempDrop = zeros(4,1);
Jre = xlsread('f_theta_in_expression_J_r','c6:c504'); %for 120 deg CA
                                                % tabulated solution
                                                % of Popov solution

%% Input
for j = 1:4
Vol = 1.87; % in uL
sub = [5, 10, 15, 20]; % substrate temperatures from experiments
iter = 9; % iterations for test

for l = 1:iter
```

```

if l == 1           % first order approximation is conduction.
                   % the following iteration uses this at the
                   % initialization
    model = 'cond';
else
    mu = (0.000817-0.000578)*(20-sub(j))/20+0.000578;
    dsig = 0.0812;
    u_Ma = TempDrop(j)*dsig/mu/1000;
    model = 'conv';
end

Tsub = sub(j) + 273.15; % substrate
Nu = 2; % convection from air

%% Droplet Geometry

theta = 120*pi/180;
Rad=(3*Vol/pi/(1-cos (theta))^2/(2+ cos (theta)))^(1/3)*1e-3; % Rad of
                                                             % droplet (in m)

Rc = Rad*sin(theta); %CR of droplet (in m)
height = Rad-Rad*cos(theta); %height of the droplet in m
V0 = Vol*1e-9; %in m3
h0 = height; %(ht in m)
Tot_SurfAr = 2*pi*(Rad)*h0; % surface area of droplet

%% Universal Constants

R = 8.3145; %J/mol.K
M = 0.032; %kg/mol - molecular mass of methanol
H = 0; % far field humidity [%]

%% Temperatures

Tamb = 21 + 273.15; % ambient
Tref = 300; % reference for properties

%% Fluid Properties

Dref = 14*10^(-6); %diffusion coeff of methanol in air at 300K
Psat_ref = 18.6107*10^3; %Psat of methanol at 300 K in Pascal
kliq = 0.204; %W/mK: conductivity of methanol

%% Domain Discretization

N = 500; % number of divisions

% height discretization
deltah = h0/N;
h_r = zeros(N,1);
h_r(1:(N-1),1) = h0-(1:(N-1))*deltah;
r = real(sqrt(-h_r.^2 + Rc.^2 - 2*h_r.*Rc./tan(theta)));
r(N) = Rc;
h_r(N,1) = 0;

```

```

% Areas for the control volume interfaces
A_top = zeros(N,1);
A_bot = zeros(N,1);
for i = 1:N-1
    h_top = h_r(i)+deltah/2;
    h_bot = h_r(i)-deltah/2;
    r_top = real(sqrt(-h_top^2 + Rc^2 - 2*h_top*Rc/tan(theta)));
    r_bot = real(sqrt(-h_bot^2 + Rc^2 - 2*h_bot*Rc/tan(theta)));
    A_top(i,1) = pi*r_top^2;
    A_bot(i,1) = pi*r_bot^2;
end

%% Calculating Ambient and Substrate Properties

[hfg_Tamb,Psat_Tamb,Cs_Tamb,Damb] = prop(Tamb,Tref,Psat_ref,Dref,M,R);
[hfg_Tsub,Psat_Tsub,Cs_Tsub,Dsub] = prop(Tsub,Tref,Psat_ref,Dref,M,R);
J_diff = Jre*(Cs_Tsub-H*Cs_Tamb)/(Rc/Dsub);

%% calculating stripe area

dels(1:N,1) = Tot_SurfAr/N; % since dels is equal for same thickness
                        % strips on spherical cap

%% Solve

T = Tsub*ones(N,2); %Initializing temperature

% thermal mass flowrate through system
A_ratio = 0.6467; % area of the central circle vs the entire cross-section
A_avg = max(A_bot(1:N-1))*A_ratio; % average interface area
rho = (293.15-Tsub)*0.9+791; %kg/m^3: density of methanol
cp = (Tsub-273.15)*2+2420; % specific heat capacity
rhocp = rho*cp;

if l > 1 % calculating mass flow-rate
    r_botmax = sqrt(max(A_bot(1:N-1))/pi);
    r_botdisc = sqrt(r_botmax^2*A_ratio);
    u_slope = u_Ma/(r_botmax-r_botdisc);
    int_u = (1/3)*pi*u_slope*(r_botdisc-r_botmax)^2*(r_botdisc+2*r_botmax);
    mcp = rhocp*int_u;
    disp('mcp =')
    disp(mcp)
end

h_ncbot = 0.1*N; % bottom of droplet where flow is horizontal
h_nctop = 0.1*N; % top fo droplet where flow is horizontal
k_air = 0.0259; % thermal conductivity of air

% initializing arrays
hfg = zeros(N,1);
Psat = zeros(N,1);
Cs = zeros(N,1);

```

```

D    = zeros(N,1);
J    = zeros(N,1);
delC = zeros(N,1);
S    = zeros(N,1);

for n = 1:150000
    T_old = T; % initialized from previous iteration
    T_vort = max(T(r==max(r))); % Temperature at vortex height
    rho = (293.15-T_vort)*0.9+791; %kg/m^3: density of methanol
    cp = (T_vort-273.15)*2+2420; % specific heat capacity
    rhocp = rho*cp;

    % calculate all the properties near substrate
    [hfg(1),Psat(1),Cs(1),D(1)] = prop(T(1,1),Tref,Psat_ref,Dref,M,R);
    delC(1) = Cs(1)-H*Cs_Tamb;
    J(1) = Jre(1)*delC(1)/(Rc/D(1));

    % air-side convection parameters
    L = 2*max(r);
    h_conv = Nu*k_air/L;

    % energy transfer calculation at liquid-air interface
    S(1) = J(1)*delS(1)*hfg(1)-h_conv*delS(1)*(Tamb-T(1,1));

    % heat transfer based on energy transfer mode within the droplet
    switch model
        case 'cond'
            T(1,1) = T(2,1) - S(1)*deltah/(k_liq*A_bot(1));
        case 'conv'
            T(1,1) = (T(2,1)+T(2,2))/2 - S(1)*deltah/(k_liq*A_bot(1));
    end
    T(1,2) = T(1,1); % ignore horizontal temperature variation.
    for i = 2:N-1 % scan each vertical slice of the droplet
        % properties of the current slice
        [hfg(i),Psat(i),Cs(i),D(i)] = prop(T(i,1),Tref,Psat_ref,Dref,M,R);
        delC(i) = Cs(i)-H*Cs_Tamb;
        J(i) = Jre(i)*delC(i)/(Rc/D(i));

        % energy transfer calculation at liquid-air interface
        S(i) = J(i)*delS(i)*hfg(i)-h_conv*delS(i)*(Tamb-T(i,1));

        % heat transfer based on energy transfer mode within the droplet
        switch model
            case 'cond'
                T(i,1) = (T(i-1,1)*A_top(i) + T(i+1,1)*A_bot(i))/(...
                    A_top(i)+A_bot(i)) - S(i)*deltah/(k_liq*(A_top(i)...
                    +A_bot(i)));
            case 'conv'
                if i < h_nctop || i > N-h_ncbot % middle section of droplet
                    T(i,1) = ((T(i-1,1)+T(i-1,2))/2*A_top(i) + (T(i+1,1)+...
                        T(i+1,2))/2*A_bot(i))/(A_top(i)+A_bot(i)) - ...
                        S(i)*deltah/(k_liq*(A_top(i)+A_bot(i)));
                    T(i,2) = T(i,1);
                else % top and bottom of the droplet
                    T(i,1) = (mcp*T(i+1,1)-S(i))/mcp;
                end
            end
        end
    end
end

```

```

        T(i,2) = T(i-1);
    end
end
end
T(N,1:2) = Tsub;           % set substrate temperature at bottom
hfg(N) = hfg_Tsub;        % set properties at bottom
J(N) = 0;
h_r(N) = 0;
resid = max(abs(T_old(:,1)-T(:,1))); % calculate residual
end

% display data for monitoring the iterations
disp('residual =')
disp(resid)
disp('Temperature Drop =')
disp(Tsub-T(1,1))
TempDrop(j) = (Tsub-T(1,1));
if l > 1
    flowrate(j) = mcp;
end
end

% mass loss from evaporation
dMdt(j) = sum(J.*dels);

% plotting temperature profile
figure(j); plot(h_r/h0,T(:,1)-273.15)
end

function [hfg,Psat,Cs,D] = prop(T,Tref,Psat_ref,Dref,M,R)
%Calculate all the properties at each temperature
%Note: this is for methanol only
% By Aditya Chandramohan March 2016
hfg = -10.286*(T)^2 + 4942.6*T + 598476; % phase change
Psat = Psat_ref*exp(M*hfg/R*(1/Tref - 1/T)); % saturation pressure
Cs = Psat/(R*T) * M; % concentration of vapor at liquid-air interface
D = Dref.*(T/Tref)^(3/2); % diffusion coefficient
end

```

## APPENDIX D. THE ROLE OF CONDENSATION FROM HUMID AIR ON MELTING OF ICE

### D.1 Nomenclature

$D$	species diffusion coefficient (m <sup>2</sup> /s)
$M$	molecular mass (g/mol)
$Pr$	Prandtl number, $\nu/\alpha$
$RH$	relative humidity (%)
$Sc$	Schmidt number, $\nu/D$
$T$	temperature (K)
$cp$	constant pressure specific heat capacity (J/(kg K))
$f$	nondimensional stream function
$g$	gravitational constant (m/s <sup>2</sup> )
$h$	latent heat (J/kg)
$k$	thermal conductivity (W/(m K))
$m$	mass fraction
$m''$	mass flux (kg/(m <sup>2</sup> s))
$u$	velocity in x-direction (m/s)
$v$	velocity in y-direction (m/s)
$x$	axis parallel to ice surface (m)
$y$	axis normal to ice surface (m)

#### D.1.1 Greek symbols

$\alpha$	thermal diffusivity (m <sup>2</sup> /s)
$\delta$	liquid film thickness (m)
$\epsilon$	normalized vapor-gas temperature
$\eta$	similarity variable
$\theta$	normalized liquid temperature
$\mu$	dynamic viscosity (kg/(m s))

$\nu$	kinematic viscosity (m <sup>2</sup> /s)
$\rho$	mass density (kg/m <sup>3</sup> )
$\phi$	normalized mass fraction
$\psi$	stream function

### D.1.2 Subscripts

$\infty$	ambient
<i>cond</i>	condensation
<i>g</i>	gas
<i>i</i>	liquid-air interface
<i>l</i>	liquid
<i>lg</i>	vaporization
<i>melt</i>	melting
<i>mp</i>	melting point
<i>sl</i>	fusion
<i>tot</i>	combined (vapor and gas)
<i>v</i>	vapor
$\delta$	liquid-gas interface

### D.1.3 Superscripts

<i>o</i>	normalized
----------	------------

## D.2 Introduction

The formation and melting of ice are of significant concern to various applications including refrigeration systems [122,123], aircraft maintenance [124,125], and frozen food processing [126]. For example, it is well known that icing adversely affects aircraft aerodynamics [125] and evaporator performance in refrigeration systems [127]. In addition, it is recommended that frozen food not be refrozen after melting due to health risks posed by bacterial growth [126]. Prediction and understanding of melting behavior under ambient conditions is vital for aircraft, which are typically placed in a warm hangar in advance of other intensive deicing procedures [125], and food

processing, where the melting rate determines the length of time that frozen food can remain under ambient conditions before it must be consumed [126].

Early studies of melting in dry air were conducted by Roberts [128] using similarity solutions. Simultaneous condensation and melting was first studied by Tien and Yen [129] by treating the gas domain as saturated vapor (as was done in Nusselt's original condensation study [130]); the liquid arising from condensation and melting were treated as one layer. Galamba *et al.* [131] accounted for the presence of noncondensable gases in the vapor, while also considering the condensate and melt as distinct, immiscible liquid layers. Yen *et al.* [132] studied cases where noncondensable gases constituted a large percentage of the vapor-gas domain (up to 70% by mass). Both of these studies [131,132] incorporated the model for thermal and species transport in the vapor-gas mixture during film condensation developed by Sparrow and Lin [133]. All of these prior studies considered saturated steam at atmospheric pressure in the vapor-gas domain based on the applications of interest, *viz.* emergency reactor cooling [132] and freeze desalination [131]. Studies of condensation-melting under atmospheric conditions, where the vapor mass fraction is very low ( $\sim 1\%$ ), has not been explored.

Existing analytical solutions for both condensation-only and condensation-melting problems exploit stream functions and similarity variables to reduce the dimensionality of the equations. The liquid domain is commonly simplified by neglecting inertial terms to allow for a closed-form integral solution [129,134]. Other studies assume heuristic polynomial profiles for the solution liquid domain variables to simplify the integration process [135]. Such simplifications are not possible in the low-Prandtl number vapor-gas domain; Sparrow and Lin solved the stream function formulations using an iterative integral approach, where an assumed profile was iterated upon until the velocity fields converged [133]. Galamba *et al.* used an iterative Runge-Kutta routine to arrive at a solution for which the mass fraction of noncondensable gases matched the prescribed atmospheric boundary conditions [131]. Several studies [131,132,134] measured the change in mass of the solid phase to experimentally validate the models. The measured change in mass was used to estimate the heat transfer coefficient, which was then compared to the respective model predictions. Experimental validations have been limited to such indirect measurement techniques.

The current study formulates normalized governing equations to predict combined condensation and melting under typical atmospheric conditions. The liquid film thickness is experimentally measured to experimentally compare to the model predictions. The predicted liquid and vapor-gas domain solutions are analyzed to explain the predominant physical mechanisms leading to melting of the solid phase as a function of the atmospheric conditions.

### D.3 Methods

#### D.3.1 Model Formulation

To solve the system of governing equations for the combined condensation-melting process, the system is divided into separate liquid and vapor-gas domains, as shown in Figure D.1. Steady-state transport is assumed in both domains. Filmwise condensation on an ice sheet with a vertical melting front is assumed. The external boundaries of the system are defined by the ice melting point and the far-field ambient air temperature, vapor mass fraction, and velocity (stagnant). The liquid has zero velocity at the melting front.

The governing equations for mass, momentum, and energy transport are the same for the liquid and vapor-gas domains:

$$\frac{\partial u}{\partial x} + \frac{\partial v}{\partial y} = 0 \quad (\text{D.1})$$

$$u \frac{\partial u}{\partial x} + v \frac{\partial u}{\partial y} = g \left[ 1 - \frac{\rho_{g\infty}}{\rho} \right] + \nu \frac{\partial^2 u}{\partial y^2} \quad (\text{D.2})$$

$$u \frac{\partial T}{\partial x} + v \frac{\partial T}{\partial y} = \alpha \frac{\partial^2 T}{\partial y^2} \quad (\text{D.3})$$

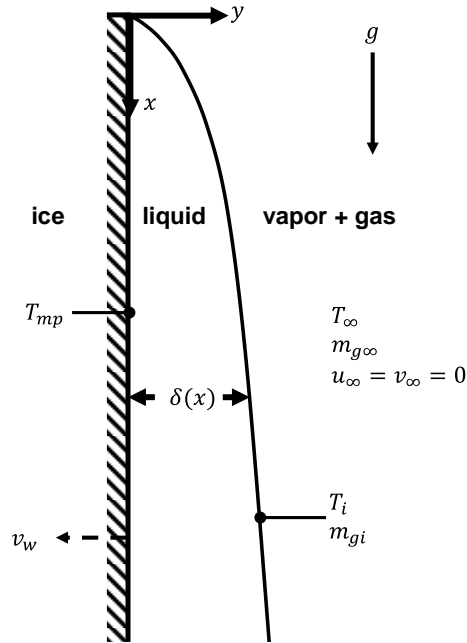


Figure D.1. Schematic diagram of the melting system is shown, including the boundary conditions ( $T_{mp}$ ,  $T_{\infty}$ ,  $m_{g\infty}$ ) and selected calculated physical parameters ( $v_w$ ,  $\delta(x)$ ,  $T_i$ , and  $m_{gi}$ ).

Species transport of vapor in the vapor-gas domain, a mixture of vapor and noncondensable gases, is governed by:

$$u \frac{\partial m_g}{\partial x} + v \frac{\partial m_g}{\partial y} = D \frac{\partial^2 m_g}{\partial y^2} \quad (\text{D.4})$$

At the solid-liquid interface, a no-slip boundary condition is applied, with liquid assumed to be at the melting point temperature. The melting rate is governed by an energy balance between conduction from liquid and the latent heat of fusion.

$$u_l(0) = 0 \quad (\text{D.5})$$

$$T_l(0) = T_{mp} \quad (\text{D.6})$$

$$v_l(0) = \frac{k_l}{\rho_l h_{sl}} \left( \frac{\partial T_l}{\partial y} \right)_{y=0} \quad (\text{D.7})$$

At the liquid-gas interface, temperature is continuous with the gas domain and there is zero shear stress (due to the much higher viscosity of the liquid compared to the gas). An energy balance at

the free interface defines the condensation rate, while accounting for the change in liquid film thickness.

$$T_l(y = \delta) = T_i \quad (\text{D.8})$$

$$\left( \frac{\partial u_l}{\partial y} \right)_{y=\delta} = 0 \quad (\text{D.9})$$

$$k_l \left( \frac{\partial T_l}{\partial y} \right)_{y=\delta} + \rho_l h_{fg} \left[ v_l - u_l \left( \frac{d\delta}{dx} \right) \right]_{y=\delta} = 0 \quad (\text{D.10})$$

At the liquid-gas interface, the boundary conditions for the vapor-gas domain include vapor species convective flux across the interface, no-slip velocity, temperature continuity, and enforcement of the noncondensable nature of the other gases in the air:

$$\left( \rho u \frac{d\delta}{dx} - \rho v \right)_{y=\delta} = \left( \rho_l u_l \frac{d\delta}{dx} - \rho_l v_l \right)_{y=\delta} \quad (\text{D.11})$$

$$u(y = \delta) = u_l(y = \delta) \quad (\text{D.12})$$

$$T(y = \delta) = T_i \quad (\text{D.13})$$

$$\left( \rho u m_g \frac{d\delta}{dx} + \rho D \frac{\partial m_g}{\partial y} - m_g \rho v \right)_{y=\delta} = 0 \quad (\text{D.14})$$

Far from the interface, the vapor-gas domain is bounded by the ambient temperature, noncondensable gas mass fraction, and zero velocity.

$$T(y = \infty) = T_\infty \quad (\text{D.15})$$

$$m_g(y = \infty) = m_{g_\infty} \quad (\text{D.16})$$

$$u(y = \infty) = 0 \quad (\text{D.17})$$

Similarity variable and stream function definitions are introduced to reduce the two-dimensional problem to a series of one-dimensional ordinary differential equations. For the liquid layer, as in Ref. [129]:

$$\eta_l = \left[ \frac{g c_{p,l} (\rho_l - \rho_\infty)}{4 \nu_l k_l} \right]^{1/4} \frac{y}{x^{1/4}} \quad (\text{D.18})$$

$$\psi_l = 4\alpha \left[ \frac{g c_{p,l} (\rho_l - \rho_\infty)}{4\nu_l k_l} \right]^{1/4} x^{3/4} f_l(\eta_l) \quad (\text{D.19})$$

$$u = \frac{\partial \psi_l}{\partial y} \quad (\text{D.20})$$

$$v = -\frac{\partial \psi_l}{\partial x} \quad (\text{D.21})$$

where  $f_l(\eta_l)$  is the nondimensional liquid stream function. The nondimensional temperature in the liquid is defined as:

$$\theta(\eta_l) = \frac{T_l - T_{mp}}{T_i - T_{mp}} \quad (\text{D.22})$$

Because the film thickness is an unknown variable, we take a unique approach to move the film thickness from the boundary condition into the system of governing equations. The similarity value at  $y = \delta$  is a constant value defined as  $\eta_\delta$ ; thus, a new variable,  $\eta^\circ$ , can be introduced to normalize the system of equations as  $\eta^\circ = \eta/\eta_\delta$ . The transformed, normalized momentum and energy equations can be written as:

$$f_l''' + \frac{\eta_\delta}{\text{Pr}} \left[ 3f_l'' - 2(f_l')^2 \right] + \eta_\delta^3 = 0 \quad (\text{D.23})$$

$$\theta'' + 3\eta_\delta f_l \theta' = 0 \quad (\text{D.24})$$

The transformed boundary conditions (Equations (D.5)-(D.10), respectively) are:

$$f_l'(0) = 0 \quad (\text{D.25})$$

$$\theta(0) = 0 \quad (\text{D.26})$$

$$f_l(0) = -\frac{1}{3} \frac{c_{p,l} (T_i - T_{mp})}{h_{s,l}} \frac{\theta'(0)}{\eta_\delta} \quad (\text{D.27})$$

$$\theta(\eta^\circ = 1) = 1 \quad (\text{D.28})$$

$$f_l''(\eta^\circ = 1) = 0 \quad (\text{D.29})$$

$$f_l(\eta^\circ = 1) = \frac{1}{3} \frac{c_{p,l} (T_i - T_{mp})}{h_{s,g}} \frac{\theta'(\eta^\circ = 1)}{\eta_\delta} \quad (\text{D.30})$$

The methodology for deriving the governing equations for the vapor-gas domain, and condensation at the liquid-gas interface, is the same as in [133] and [136]. The similarity variable and stream function are:

$$\eta = \left[ \frac{g (M_g - M_v)}{4\nu^2 (M_g - (M_g - M_v) m_{g\infty})} \right]^{1/4} \left( \frac{y - \delta}{x^{1/4}} \right) \quad (\text{D.31})$$

$$\psi = 4\nu \left[ \frac{g (M_g - M_v)}{4\nu^2 (M_g - (M_g - M_v) m_{g\infty})} \right]^{1/4} f(\eta) \quad (\text{D.32})$$

where  $f(\eta)$  is the nondimensional vapor-gas stream function. A mass fraction difference  $\phi = m_g - m_{g\infty}$  and nondimensional temperature  $\varepsilon = T/T_\infty$  are also defined. This allows the buoyancy term to be represented as:

$$1 - \frac{\rho}{\rho_\infty} = \frac{(\phi\varepsilon + (1 - \varepsilon)(M_{tot} - m_{g\infty}))}{M_{tot} - m_{g\infty}} \quad (\text{D.33})$$

where  $M_{tot} = M_g / (M_g - M_v)$ . Thus, the system of governing equations becomes

$$f''' + 3ff'' - 2(f'')^2 + \phi\varepsilon + (1 - \varepsilon)(M_{tot} - m_{g\infty}) = 0 \quad (\text{D.34})$$

$$\phi'' + 3Sc f \phi' \quad (\text{D.35})$$

$$\varepsilon'' + Pr f \varepsilon' = 0 \quad (\text{D.36})$$

The transformed boundary conditions (Equations (D.11)-(D.17)), respectively) are:

$$f(0) = \left( \frac{\rho_l \mu_l}{\rho \mu} \right)^{1/4} \left[ \frac{M_g - M_v}{M_g - (M_g - M_v) m_{g\infty}} \right]^{-1/4} \frac{f_l(\eta^o = 1)}{\text{Pr}_l^{-3/4}} \quad (\text{D.37})$$

$$f'(0) = \frac{1}{2} \frac{\eta_\delta^2}{\text{Pr}_l^{1/2}} \left[ \frac{M_g - M_v}{M_g - (M_g - M_v) m_{g\infty}} \right]^{-1/2} \quad (\text{D.38})$$

$$\varepsilon(0) = \frac{T_i}{T_\infty} \quad (\text{D.39})$$

$$\phi'(0) + 3f(0)Sc(\phi(0) + m_{g\infty}) = 0 \quad (\text{D.40})$$

$$\varepsilon(\infty) = 1 \quad (\text{D.41})$$

$$\phi(\infty) = 0 \quad (\text{D.42})$$

$$f'(\eta = \infty) = 0 \quad (\text{D.43})$$

### D.3.2 Solution Approach

We assume constant properties to solve the model; liquid and gas properties are evaluated at reference temperatures defined respectively as:

$$T_{ref,l} = 0.5(T_i + T_{mp}) \quad (\text{D.44})$$

$$T_{ref,g} = \frac{1}{3}(T_i + T_\infty) \quad (\text{D.45})$$

The system of equations was solved using an in-house algorithm implemented in MATLAB [98]. An initial guess is made for the interface temperature. The governing equations for the liquid domain are then solved based on this interface temperature using a boundary value problem solver (*bvp4c*), with the film thickness as a free parameter. Using this solution for the liquid domain, the mass flux boundary conditions at the liquid-gas interface are calculated for the vapor-gas domain. The vapor-gas domain equations are then solved using the same boundary value problem solver. The calculated interfacial vapor concentration is compared to the saturation vapor concentration of the initial guess temperature. If the values do not agree within a tolerance of  $1 \times 10^{-4}$ , the interface temperature guess is adjusted; this iteration continues until the solution for the interfacial mass fraction converges.

### D.3.3 Experiment

An experimental facility is designed to allow for the study of condensation-melting from a vertical ice sheet under known environmental conditions. A thermoelectric cooling stage controls the temperature of the ice sheet, and the thickness of the liquid film that develops is measured. A three-dimensional drawing of the experimental facility is shown in Figure D.2.

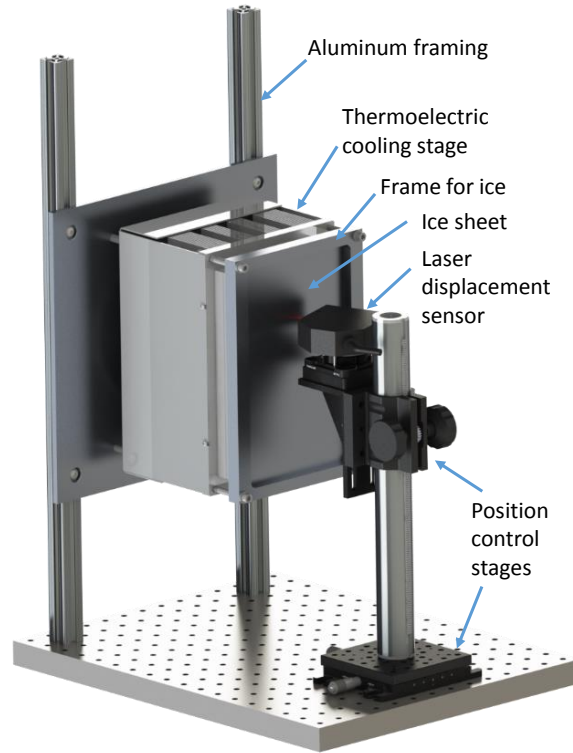


Figure D.2. Three-dimensional drawing of the experimental setup.

The ice sheet was fabricated onto a thermoelectric cooling stage (CP-200, TE Technology, Inc.), with an attached aluminum mold to shape the ice into a 22.9 cm  $\times$  14.6 cm  $\times$  0.5 cm rectangular sheet. To fabricate the ice, the stage was oriented horizontally and a thin layer ( $\sim$ 1 mm) of deionized water was poured into the mold. The temperature of the cooling stage was reduced slowly ( $\sim$ 0.5  $^{\circ}$ C every 30 min) from 0  $^{\circ}$ C until the water was completely frozen. Additional water was then added to form the ice sheet layer by layer. This process allowed bubbles, formed from dissolved gas in the water, to purge from the ice during freezing, forming a clear, defect-free sheet. The thermoelectric stage and ice sheet were then oriented into a vertical position using aluminum framing. To initiate a condensation-melting test, the cooling stage temperature was raised to a fixed value of 0  $^{\circ}$ C. The ambient temperature and relative humidity are measured with a thermocouple and a hygrometer, respectively.

The liquid film thickness is measured using a laser displacement sensor. Such displacement sensors have been used previously for measuring a liquid film on a flat surface [137] and a liquid-vapor interface in a dynamic two-phase flow environment [138]. A laser displacement sensor head

(Keyence LK-G37) connected to a controller (Keyence LK-G3000) was placed on a translational stage to position the measurement location along the ice sheet. There is negligible heating by the laser (0.95 mW) due to the low absorption coefficient of water ( $3.71 \times 10^{-3} \text{ cm}^{-1}$  [139]) at the measurement wavelength (655 nm). Due to the matching index of refraction for liquid water and ice, a measurement of this interface position with respect to the liquid-air interface during condensation-melting was not possible. Instead, the location of the liquid-air interface was first measured; swift subsequent wiping away of the liquid film allowed the displacement sensor to capture the exposed ice-liquid interface. The difference between the two positions was recorded as the film thickness. The liquid film was allowed to redevelop for 60 s between measurements; this period was observed to be sufficient to achieve a steady thickness. The sensor head was moved along the vertical direction, in 25.4 mm increments to conduct this film thickness measurement at various heights. Film thickness measurements were conducted six times at each height.

#### D.4 Results and Discussion

The model was first evaluated for a base case at the experimental conditions, an ambient temperature of 26 °C with a relative humidity of 40%. The outputs of the model are depicted in Figure D.3. While these unsaturated air conditions have not been previously investigated, trends in the stream function derivative and gas mass fraction can be compared to studies of vapor condensation with noncondensable gas in the literature [133] to validate the new model formulation. The derivative of the nondimensional vapor-gas stream function,  $f'(\eta)$ , is representative of the two-dimensional velocity field as shown in Equations (D.19)-(D.21). Figure D.3(a) displays a peak in this value due to natural convection in the air induced by the interfacial heating during condensation-melting; the value is nonzero at the liquid-air interface due to downward flow at the liquid film. The gas mass fraction shown in Figure D.3(a) has a maximum value at the liquid-air interface. The change from the far field value is due to condensation at the interface. Both of these profiles follow the same trends as presented by Sparrow and Lin [133]. The derivative of the nondimensional liquid stream function,  $f_l'(\eta)$ , is representative of the liquid velocities; the velocities in the liquid are predominantly vertical. Since one interface is non-slip and the other zero shear, the gravity-driven flow is expected to assume a quadratic flow velocity profile. The shape of  $f_l'(\eta)$  in Figure D.3(b) follows this profile. The near-linear non-dimensional

temperature profile shown on the second axis of Figure D.3(b) is anticipated due to the small (conduction-dominated) thickness of the liquid film.

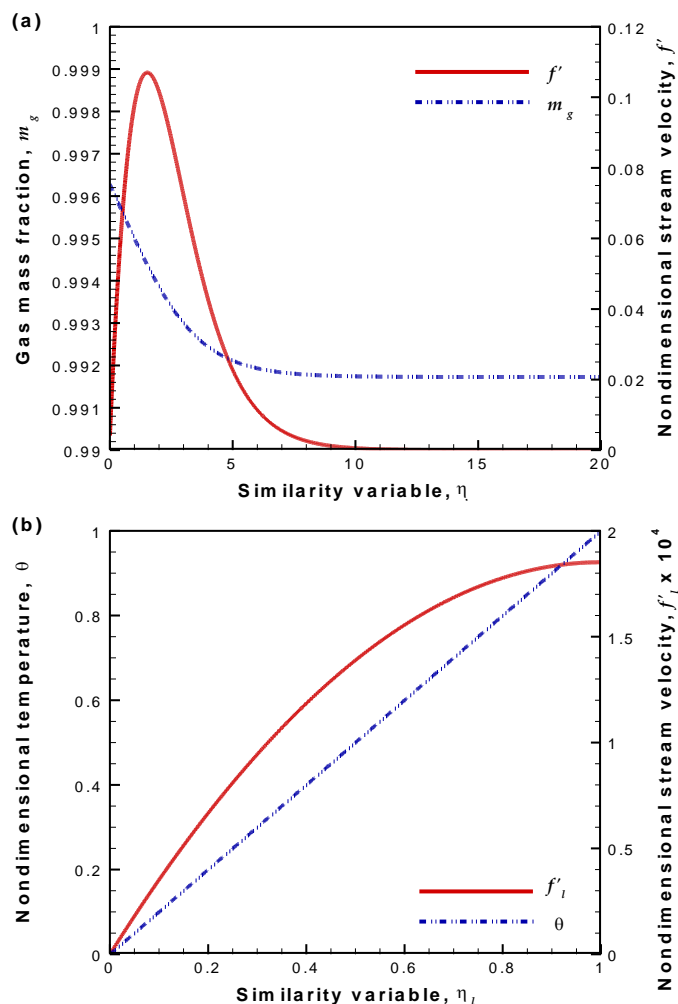


Figure D.3. (a) Derivative of the nondimensional vapor-gas stream function,  $f'(\eta)$ , and the gas mass fraction in the vapor-gas domain. (b) Derivative of the nondimensional liquid stream function,  $f'_l(\eta_l)$ , and the nondimensional temperature profile in the liquid domain.

The liquid film thickness was calculated from the solution by solving the similarity variable equation for  $\delta$ . Figure D.4(a) shows the experimental film thickness measurements along with the model predictions. Close agreement is observed, supporting the validity of the model.

The condensation and melting interfacial mass fluxes are calculated from the solutions as:

$$m''_{melt} = k_l \left( \frac{\partial T_l}{\partial y} \right)_{y=0} = k_l (T_i - T_{mp}) \left[ \frac{g c_{p,l} (\rho_l - \rho_\infty)}{4 \nu_l k_l} \right]^{1/4} \frac{\theta'(0) \eta_\delta}{h_{sl}} x^{-1/4} \quad (D.46)$$

$$m''_{cond} = k_l \left( \frac{\partial T_l}{\partial y} \right)_{y=0} = k_l (T_i - T_{mp}) \left[ \frac{g c_{p,l} (\rho_l - \rho_\infty)}{4 \nu_l k_l} \right]^{1/4} \frac{\theta'(\eta^\circ = 1) \eta_\delta}{h_{lg}} x^{-1/4} \quad (D.47)$$

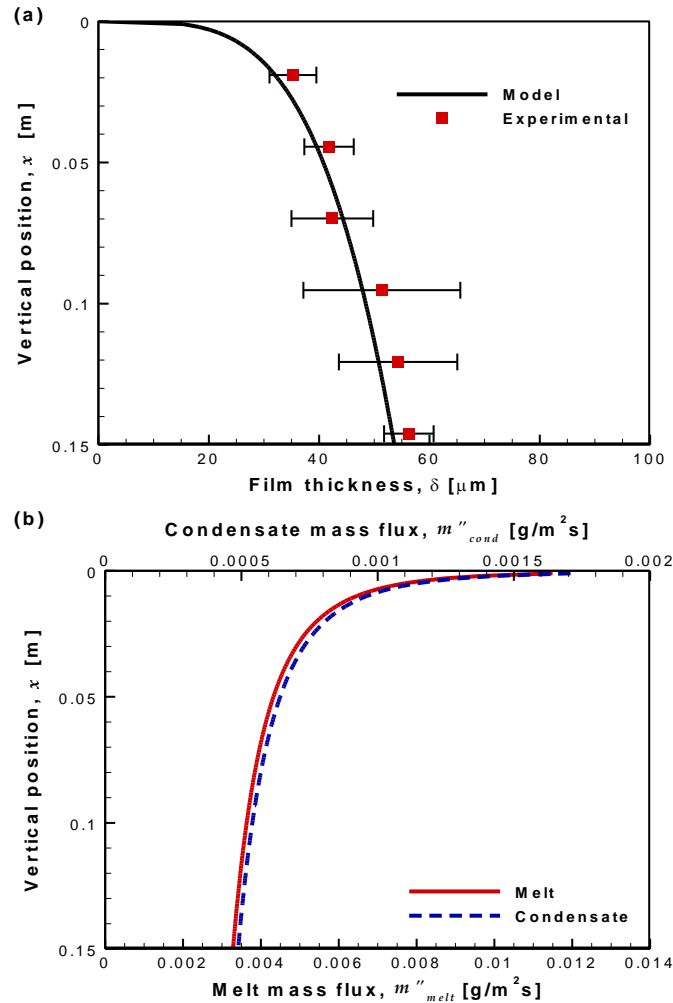


Figure D.4. (a) Predicted and measured liquid film thickness results and (b) melting and condensation mass fluxes along the vertical direction at ambient conditions ( $T_\infty = 26^\circ\text{C}$ , RH = 40%); the error bars represent the standard deviation of the measurements.

Figure D.4(b) shows the profiles of the melting and condensing mass fluxes as a function of vertical position. It is noted that the maximum in both these fluxes occurs where the film is thinnest. This is expected since the liquid film poses a thermal resistance (as illustrated by the temperature

gradient in this film) and inhibits condensation. The mass flux profiles of condensation and melting are nearly identical, which suggests that the melting process is primarily driven by the release of latent heat by condensation. The higher magnitude of melting is a result of the latent heat of fusion being an order of magnitude lower than the latent heat of vaporization.

Given the condensation-driven nature of the melting process, we explore the important of relative humidity on the melting process at an ambient temperature of 26 °C. The liquid film thickness, melting mass flux, and condensate mass flux are shown as a function of relative humidity (or gas mass fraction) in Figure D.5. The film thickness and mass fluxes directly increase with the relative humidity. The amount of vapor content in the air is revealed to have a strong influence on the melting rate; an increase in the relative humidity from 25% to 75% is predicted to increase the melting mass flowrate per unit depth (integrated over the  $x$ -direction) by approximately two orders of magnitude. The humidity must therefore be carefully considered for applications in which the melting rate under ambient conditions is critical.

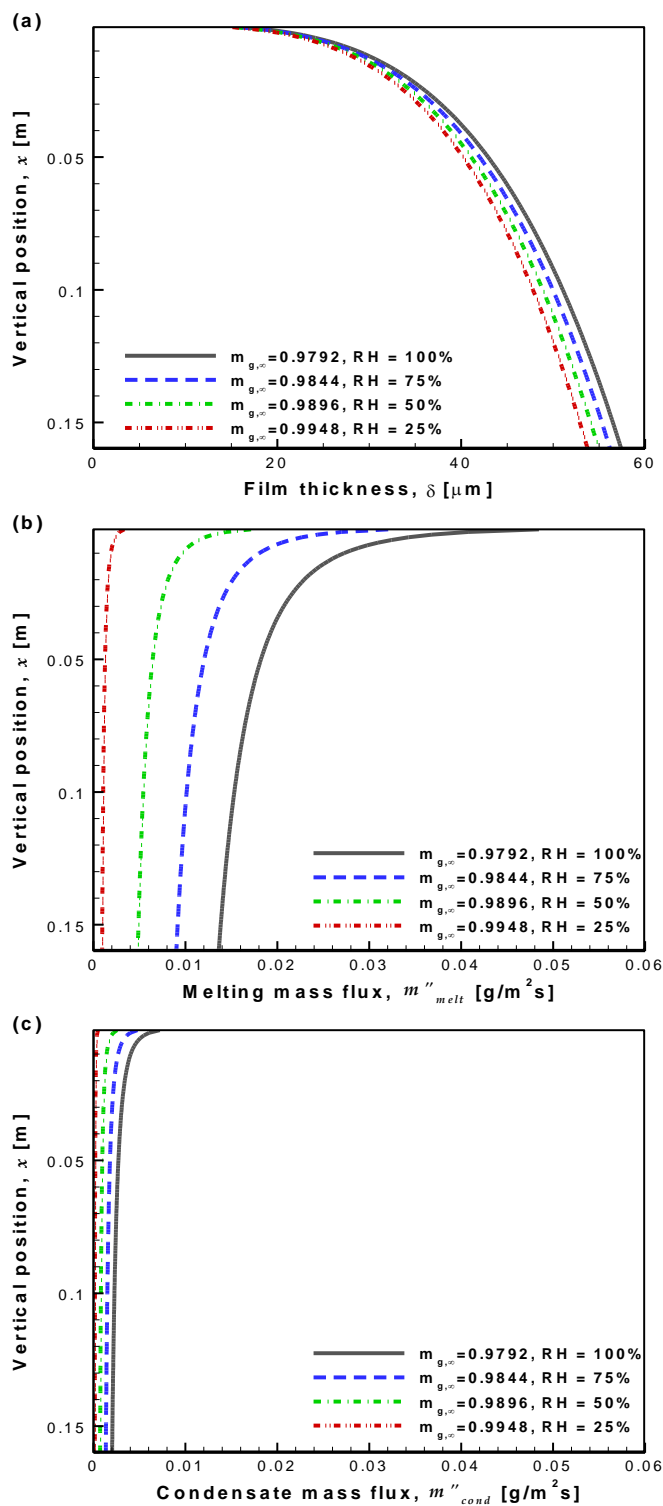


Figure D.5. (a) Liquid film thickness, (b) melting mass flux, and (c) condensate mass flux are shown with vertical position for four different levels of ambient relative humidity.

## **D.5 Conclusions**

An analytical model was developed to investigate the simultaneous condensation and melting processes under typical ambient conditions, a process of critical importance to refrigeration, aircraft maintenance, frozen food processing, and other applications. The model was first validated for a baseline case via analysis of the predicted flow and temperature fields and comparison to experimentally measured liquid film thickness. Interrogation of the local interfacial fluxes indicated that condensation is the predominant transport mechanism that governs the melting rate. Given the condensation-driven nature of the melting process, a parametric study was conducted to demonstrate the strong sensitivity of the melting rate to the relative humidity of the ambient air.

## APPENDIX E. ABSORBANCE-BASED COLORIMETRIC QUANTITATION IN EVAPORATING, SESSILE DROPLETS ON A NONWETTING SUBSTRATE

### E.1 Droplet Volume and Height Evolution

Figure E.1 shows the goniometric measurements of a droplet parameters (volume and height) for a case where the sample has 0 mg/ml (0  $\mu$ M) protein and one with 0.15 mg/mL (2.26  $\mu$ M). As can be seen, there is no significant different in the evolution of either height or volume evolution between the two cases.

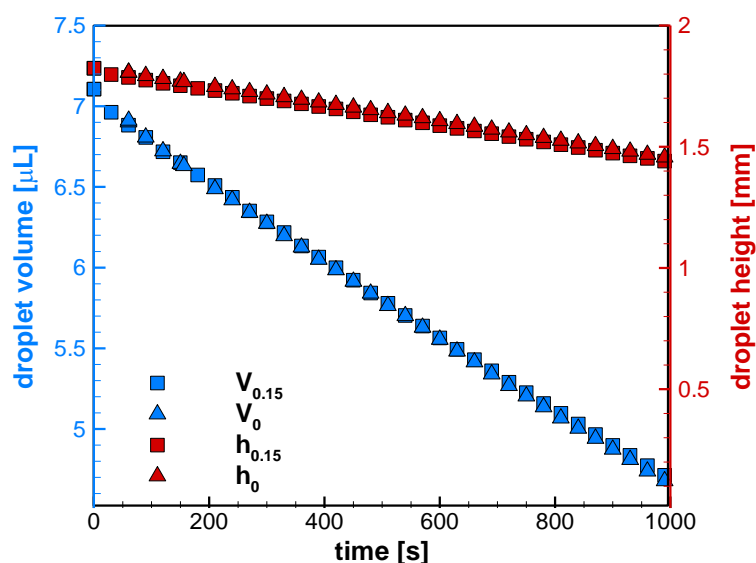


Figure E.1. The droplet volume evolution is shown (in blue) alongside the droplet height (in red) for two droplets with sample concentrations of 0 mg/mL (0  $\mu$ M) and 0.15 mg/mL (2.26  $\mu$ M).

### E.2 Raw Signal Measurements

Figure E.2 shows the raw voltage measurements by the photodiode for the premixed test case for three concentrations: 0.10 mg/mL (1.51  $\mu$ M), 0.15 mg/mL (2.26  $\mu$ M), and 0.30 mg/mL (4.51  $\mu$ M). Overall, the signal decreases monotonically with concentration. This is expected because the absorbance increases with higher concentration.

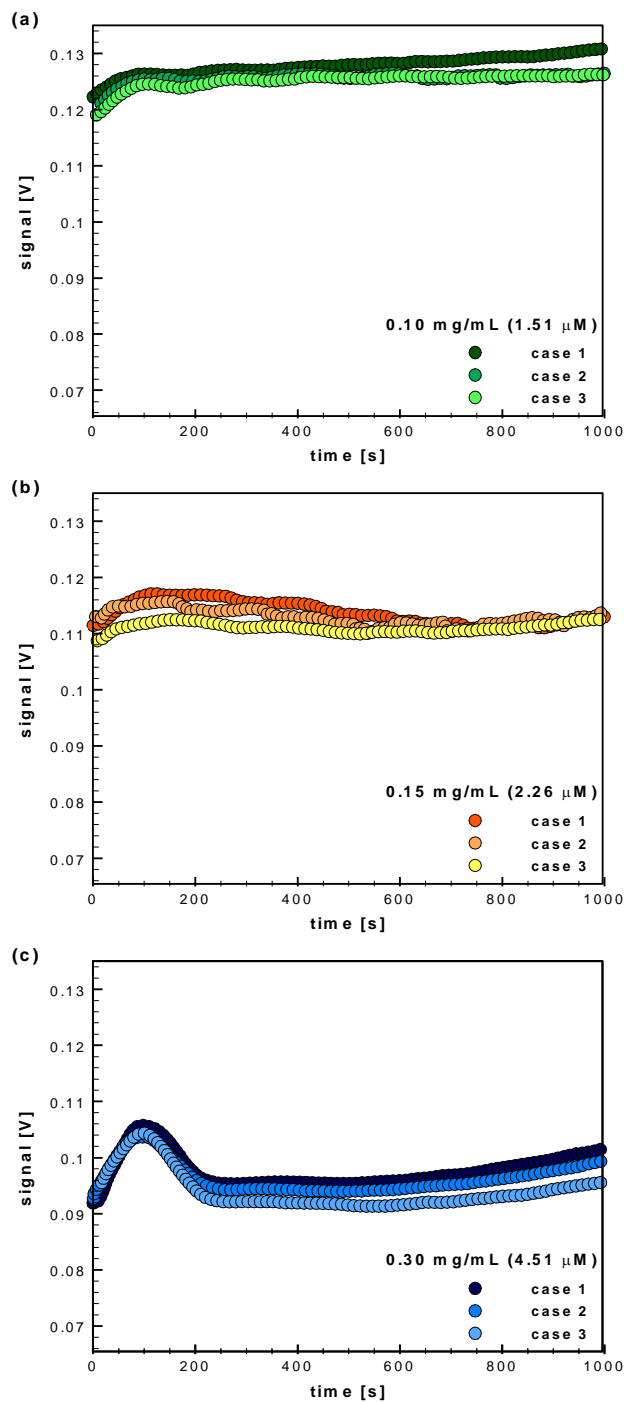


Figure E.2. Time-resolved raw voltage measurements of premixed sample droplets are shown for (a) 1.51  $\mu\text{M}$ , (b) 2.26  $\mu\text{M}$ , and (c) 4.51  $\mu\text{M}$ .

Figure E.3 shows the raw voltage measurements by the photodiode for the *in situ* mixed test cases for three concentrations: 0.10 mg/mL (1.51  $\mu\text{M}$ ), 0.15 mg/mL (2.26  $\mu\text{M}$ ), and 0.30 mg/mL

(4.51  $\mu\text{M}$ ). Overall, the signal decreases monotonically with concentration and the trends are most pronounced in the two valleys and the peak in the voltage signal.

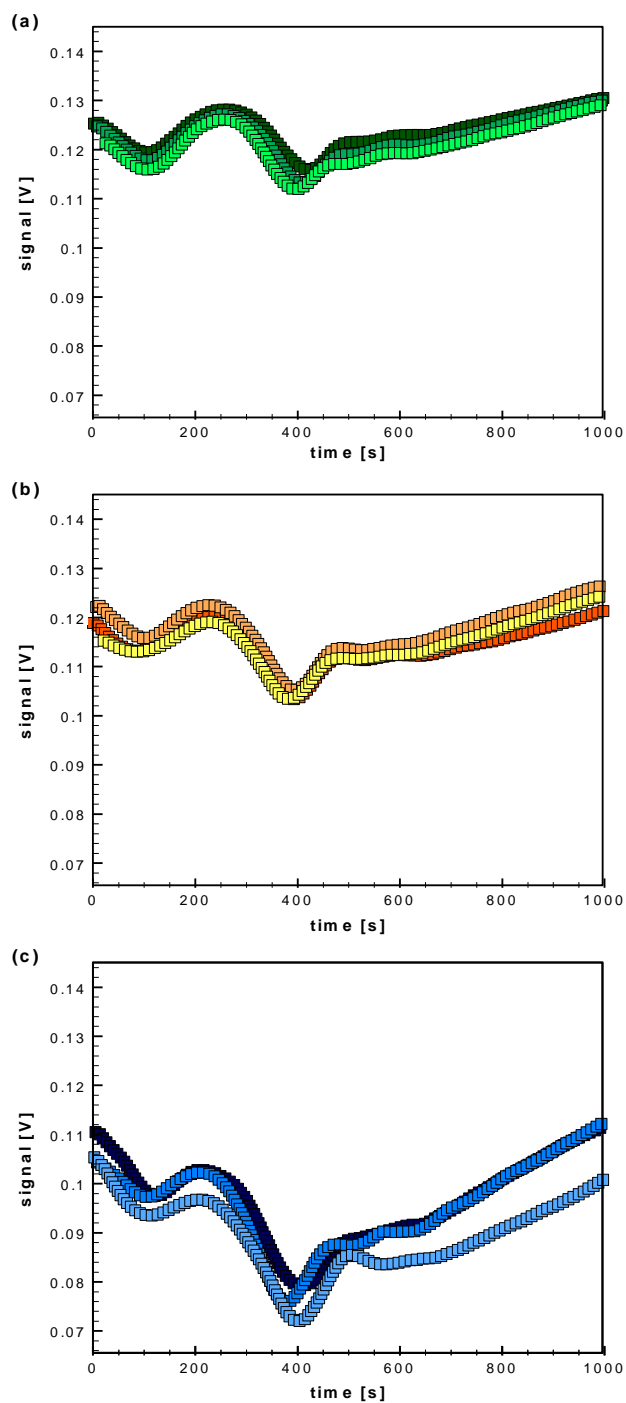


Figure E.3. Time-resolved raw voltage measurements of *in situ* sample droplets are shown for (a) 1.51  $\mu\text{M}$ , (b) 2.26  $\mu\text{M}$ , and (c) 4.51  $\mu\text{M}$ .

## APPENDIX F. LIST OF EXPERIMENTAL EQUIPMENT

Table F.1. Experimental Equipment and Materials.

<b>Part</b>	<b>Vendor</b>	<b>Part Number</b>	<b>Description</b>
Heater	Omega	KHLV-105/10-P	Flexible, thin film heater with serpentine resistor to heat samples
Temperature controller	Glas-Col	Temp-o-Trol TOT-1200	Feedback temperature controller to drive heaters
Infrared camera	FLIR	SC7650	1.5-5.1 um infrared camera for temperature measurements
Lens	Janos	Asio F/2.3 MWIR	Midwave infrared camera lens
Blackbody calibrator	SBIR	DB-04	Differential blackbody calibrator
Cooling stage	TE Technology	CP-031HT	Temperature controlled thermoelectric cooling stage
Lens	Janos	Nyctea	50 mm infrared camera lens
Pipette	AccuPet	AP-10	0.1-10 uL pipette for droplet measurements
Laser	Coherent	Verdi V5	532 nm 5W continuous Laser
High-speed camera	Photron	FASTCAM-1024PCI	Camera used for PIV measurements
Lens	Cosmicar	TV Lens	50 mm, 1:1.8 Lens for PIV measurements
LED	Thorlabs	LED591E	591 nm photodiode

Photodiode	Thorlabs	FD11A	1 mm <sup>2</sup> area visible light photodiode for light measurement
Multimeter	Keysight	34410A	Digital multimeter to measure photodiode signal
Glass slides	Gold Seal ®	3057	1 mm thick glass slides for substrates
Teflon	Dupont	Teflon® AF2400	Teflon granules to coat glass slides
Refrigerant solvent	3M	Fluorinert Electronic Liquid FC-72	Solvent used to dissolve Teflon
BSA	Sigma-Aldrich	98% lyophilized powder Bovine Serum Albumin	Protein used in the colorimetric quantitation experiments
Bradford reagent	Sigma-Aldrich	Bradford Reagent	Dye containing Coomassie Brilliant Blue G-250 in phosphoric acid and methanol for colorimetry of protein
Cooling stage	TE Technology	CP-200	Coling stage for condensation-melting on ice
Laser displacement sensor head	Keyence	LK-G37	Sensor to measure liquid film thickness on ice
Laser displacement sensor controller	Keyence	LK-G3000	Controller for laser displacement sensor

Methanol	N/A	N/A	Working liquid for droplet evaporation tests
Deionized water	N/A	N/A	Solvent for protein and as working liquid for droplet evaporation tests
1H,1H,2H,2H-perfluorodecyltrichlorosilane	N/A	N/A	Solution to silanize copper surfaces for nonwettability
Acetone	N/A	N/A	For surface cleaning

## VITA

Aditya Chandramohan is a Graduate Research Assistant in the Cooling Technologies Research Center, an I/UCRC at Purdue University and a recipient of the Cordier Fellowship. He joined Purdue University to pursue a Ph.D. in Mechanical Engineering under the advisement of Dr. Suresh Garimella and Dr. Justin Weibel. His research currently focuses on the microscale measurement techniques and their applications towards better characterization of microscale thermofluidic environments. Aditya received his B.S. in Mechanical Engineering from the University of California, Los Angeles in 2012.

## PUBLICATIONS

- [1] Dash, S., Chandramohan, A., and Garimella, S. V., 2014, “Flow Visualization During Droplet Evaporation on Hydrophobic and Superhydrophobic Surfaces,” *J. of Heat Transfer*, 136(8), p. 080917.
- [2] Dash, S., Chandramohan, A., Weibel, J. A., and Garimella, S. V., 2014, “Buoyancy-Induced on-the-Spot Mixing in Droplets Evaporating on Nonwetting Surfaces,” *Phys. Rev. E*, 90(6), p. 062407.
- [3] Chandramohan, A., Dash, S., Weibel, J. A., Chen, X., and Garimella, S. V., 2016, “Marangoni Convection in Evaporating Organic Liquid Droplets on a Nonwetting Substrate,” *Langmuir*, 32(19), pp. 4729–4735.
- [4] Chandramohan, A., Weibel, J. A., and Garimella, S. V., 2016, “The Role of Condensation from Humid Air on Melting of Ice,” 15th IEEE Intersociety Conference on Thermal and Thermomechanical Phenomena in Electronic Systems (ITherm), pp. 1340–1346.
- [5] Chandramohan, A., Weibel, J. A., and Garimella, S. V., 2017, “Spatiotemporal Infrared Measurement of Interface Temperatures during Water Droplet Evaporation on a Nonwetting Substrate,” *Appl. Phys. Lett.*, 110(4), p. 041605.
- [6] Chandramohan, A., Lyons, S. K., Weibel, J. A., and Garimella, S. V., 2018, “Error Reduction in Infrared Thermography by Multiframe Super-Resolution,” *J. Electron. Packag.*, 140(4), p. 041008.
- [7] Lyons, S. K., Chandramohan, A., Weibel, J. A., and Garimella, S. V., 2019, “Simultaneous Measurement of Temperature and Strain in Electronic Packages using Multiframe Super-Resolution Infrared Thermography and Digital Image Correlation,” in preparation.
- [8] Chandramohan, A., Weibel, J. A., and Garimella, S. V., 2019, “Absorbance Based Colorimetric Quantitation in Evaporating, Sessile Droplets on a Nonwetting Substrate,” in preparation.